



HAL
open science

Peptide-conjugated nanoparticles for targeted photodynamic therapy

Batoul Dhaini, Bibigul Kenzhebayeva, Amina Ben-Mihoub, Mickaël Gries, Samir Acherar, Francis Baros, Noémie Thomas, Joël Daouk, Hervé Schohn, Tayssir Hamieh, et al.

► **To cite this version:**

Batoul Dhaini, Bibigul Kenzhebayeva, Amina Ben-Mihoub, Mickaël Gries, Samir Acherar, et al.. Peptide-conjugated nanoparticles for targeted photodynamic therapy. *Nanophotonics*, 2021, *Nanophotonics and immunotherapy for cancer*, 10 (12), pp.3089-3134. 10.1515/nanoph-2021-0275 . hal-03350919

HAL Id: hal-03350919

<https://hal.science/hal-03350919>

Submitted on 21 Sep 2021

HAL is a multi-disciplinary open access archive for the deposit and dissemination of scientific research documents, whether they are published or not. The documents may come from teaching and research institutions in France or abroad, or from public or private research centers.

L'archive ouverte pluridisciplinaire **HAL**, est destinée au dépôt et à la diffusion de documents scientifiques de niveau recherche, publiés ou non, émanant des établissements d'enseignement et de recherche français ou étrangers, des laboratoires publics ou privés.



Review

Batoul Dhaini, Bibigul Kenzhebayeva, Amina Ben-Mihoub, Mickaël Gries, Samir Acherar, Francis Baros, Noémie Thomas, Joël Daouk, Hervé Schohn, Tayssir Hamieh and Céline Frochot*

Peptide-conjugated nanoparticles for targeted photodynamic therapy

<https://doi.org/10.1515/nanoph-2021-0275>

Received June 1, 2021; accepted July 16, 2021;

published online September 17, 2021

Abstract: Cancer is the second leading cause of death worldwide after cardiovascular disease. Depending on the type and the location of the tumor, several cancer treatments are implemented. Among these, the three most conventional therapies are surgery, radiotherapy and chemotherapy. However, there are other therapeutic approaches such as photodynamic therapy (PDT). PDT relies on the combined action of light, a photoactivable molecule called photosensitizer (PS) and molecular oxygen. Most of the PSs used for clinical applications are not cancer-cell specific. One of the

solutions to overcome this problem is the use of nanoparticles (NPs) to induce a passive targeting. It is also possible to graft a vector onto the NPs to specifically target membrane receptors overexpressed in the tumor cells or neovessels surrounding the tumor. In this review, we focus on the NPs loaded with PSs and coupled to peptides for targeted PDT. We described nanosystems that targeted Neuropilin-1 (NRP-1), $\alpha_v\beta_3$ integrins, nucleolin membrane receptor, epidermal growth factor (EGF) receptor, protein-glutamine-gamma-glutamyltransferase (TGM2), p32, transferrin, PD-1, and mitochondrial membrane. The use of a cell absorbing-peptide is also described.

Keywords: cancer; nanoparticle; peptide; photodynamic therapy; photosensitizer; targeting.

*Corresponding author: Céline Frochot, Reactions and Chemical Engineering Laboratory, Université de Lorraine, LRGP-CNRS, F-54000, Nancy, France, E-mail: celine.frochot@univ-lorraine.fr <https://orcid.org/0000-0002-7659-3864>

Batoul Dhaini, Reactions and Chemical Engineering Laboratory, Université de Lorraine, LRGP-CNRS, F-54000, Nancy, France; and Laboratory of Materials, Catalysis, Environment and Analytical Methods Laboratory (MCEMA), Faculty of Sciences, Lebanese University, Hadath, Lebanon

Bibigul Kenzhebayeva, Laboratory of Macromolecular Physical Chemistry, Université de Lorraine, LCPM-CNRS, F-54000, Nancy, France; and The Department of Chemical and Biochemical Engineering, University of Satbayev, Almaty, Kazakhstan. <https://orcid.org/0000-0002-0531-4805>

Amina Ben-Mihoub and Samir Acherar, Laboratory of Macromolecular Physical Chemistry, Université de Lorraine, LCPM-CNRS, F-54000, Nancy, France

Mickaël Gries, Noémie Thomas, Joël Daouk and Hervé Schohn, Department of Biology, Signals and Systems in Cancer and Neuroscience, Université de Lorraine, CRAN-CNRS, F-54000 Nancy, France

Francis Baros, Reactions and Chemical Engineering Laboratory, Université de Lorraine, LRGP-CNRS, F-54000, Nancy, France

Tayssir Hamieh, Laboratory of Materials, Catalysis, Environment and Analytical Methods Laboratory (MCEMA), Faculty of Sciences, Lebanese University, Hadath, Lebanon; and Faculty of Science and Engineering, Maastricht University, P.O. Box 616, 6200 MD Maastricht, The Netherlands

1 Introduction

Cancer is the second leading cause of death in the world after cardiovascular disease [1]. Cancer treatment is mainly based on surgery, radiotherapy, and/or chemotherapy, where the used therapeutic strategy depends on the cancer type and localization [2, 3]. The chemoradiotherapy treatment, which combines both radiotherapy and chemotherapy, exerts adverse effects on the normal cells surrounding the tumors. It is also well-known that the anticancer drugs could lead to the appearance of cell resistance mechanisms, resulting in the progression of tumors and rendering drug-treatment ineffective. An alternative strategy is the photodynamic therapy (PDT) [4]. PDT has been discovered more than 100 years ago by Raab and Tappeiner [5]. The principle of PDT consists of the transfer of light photons to a molecule, a photosensitizer (PS), which, in the presence of molecular oxygen, produces mainly singlet oxygen (1O_2) and other reactive oxygen species (ROS), through photoreaction of type II and I, respectively (Figure 1). The production of ROS/singlet oxygen at the loci of the mitochondrial, lysosomal, or endoplasmic reticulum (ER) can directly initiate cell death by apoptosis [6]. Apoptosis is an irreversible pathway to cell death. One of the

triggers for apoptosis is the release of cytochrome C into the cytoplasm, the photodamaged mitochondria trigger an apoptotic response and result in the destruction of anti-apoptotic proteins. When cells are unable to undergo apoptosis, the autophagy pathway will be proposed as the cell death pathway. Autophagy allows the recycling of cellular components under conditions of starvation. The third pathway to cell death is necrosis. Necrosis is often the consequence of an external cell injury. This injury is due to a supralethal dose of drug/light causing loss of membrane integrity. It can also occur after direct photodamage to the plasma membrane. When no apoptotic mechanism is involved, a fourth cell death pathway is proposed: Paraptosis [7]. The hallmark is a substantial degree of vacuolation which appears to involve the ER and possibly the mitochondria. PDT may also have implications for the treatment of distant metastases, as an increased immunologic effect may result [8]. In 1978 Dougherty performed the first clinical applications in digestive oncology, demonstrating the interest of PDT strategy in a clinical context [9, 10]. The treatment by PDT presents many advantages. It is of low cost, less invasive than surgery, localized, presents little or no side effects, can be combined with other treatments and can be repeated many times at the same site without causing unwanted effects [10, 11].

PDT is used in dermatology, urology, gastroenterology, gynecology, neurosurgery, and pneumology [10]. Although it is currently in clinic, there are several difficulties that hinder the application of PDT. These include

the poor penetration of light into the tissues; the hydrophobicity of the PSs, which in its turn increases the self aggregation and decreases the cell incorporation efficiency, as well as their low selectivity towards tumor cells [12].

To overcome this, a breakthrough strategy based on nanoparticles (NPs) doped with PSs had been developed [13]. NPs could be delivered into the tumor areas *via* the enhanced permeability and retention (EPR) effect, consisting of the modeling of the vascular system surrounding tumors with concomitant fenestration of the neoplastic vessels [14]. Moreover, the delivery of NPs into the tumor was improved by coupling peptides that target membrane receptors localized on the cancer cell surface or the surrounding neovessels. In addition, receptors involved in cell trafficking were also used for NP absorption. Noting that some peptide based nanoparticles are developed to be pH sensitive for photodynamic therapy (PDT) with prolonged tumor retention times [15].

The selectivity of PDT relies both upon the targeting of the light delivery and on the preferential uptake of the photosensitizer by malignant tissue. The majority of photosensitizers are taken up nonselectively by all cell types studied *in vitro*, and can also accumulate in normal cells. Different strategies can be addressed to improve the selectivity of PS. By using nanoparticles, the Enhanced Permeability retention (EPR) Effect allows the passive accumulation of the NP into the tumor. This is called the passive targeting. To target receptors over-expressed onto

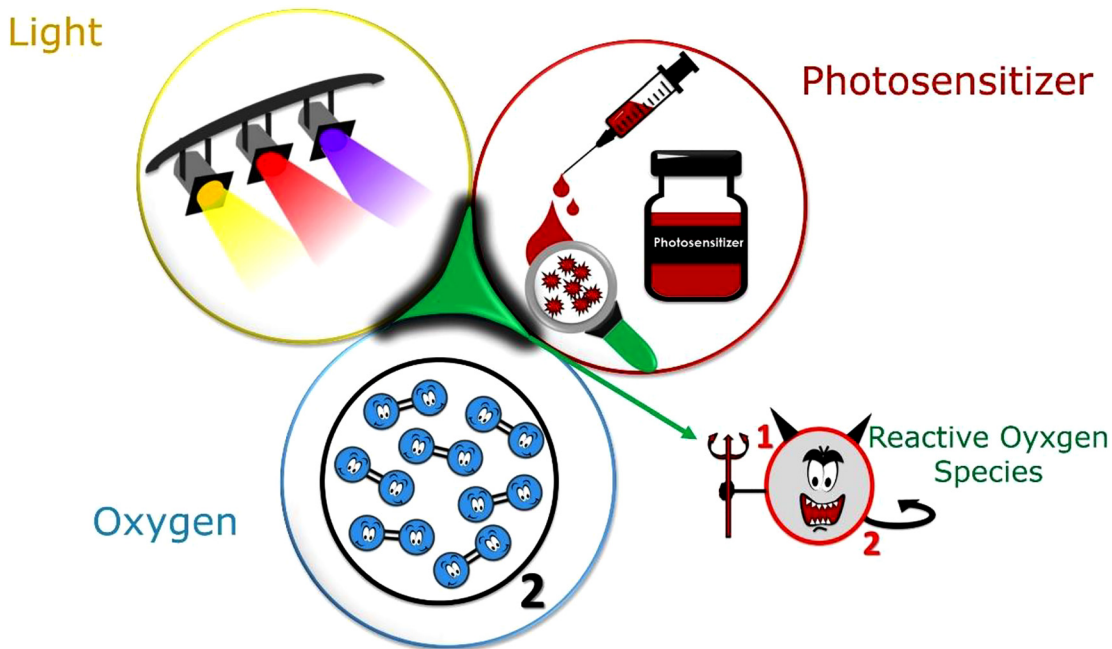


Figure 1: Schematic presentation of PDT functionalization.

membranes of tumor cells or neovessels, it is possible to attach a vector to the photosensitizer or the nanoparticle. It is active targeting. Different vectors are described in the literature such as folic acid that targets folic acid receptor over-expressed on many tumoral cell membranes [16], but can suffer from low stability [17]. Stability of folic acid under several parameters [18], antitumor monoclonal antibodies [19] that present drawbacks such as their large size and nonspecific uptake of the antibody molecules by the liver and the reticulo-endothelial system [18]. Moreover, anti-tumor monoclonal antibodies exhibit low tissue penetration and poor cellular uptake when used *in vivo* [20]. Protein [21] can also be coupled with success to PS as well as aptamer [22]. Small peptides represent excellent targeting agents for receptors over-expressed in human cancers. We already describe in a review [23] all the advantages of using peptides such as their small size, they present good tissue permeability, rapid access to the tumor site, they can cross a disturbed blood–brain barrier (BBB), and they present low antigenicity. They are easy to synthesize in liquid or solid phases, easy to modify (pseudo-peptides), easy to link to a spacer *via* amide bond for example, they can present high affinity for receptors and rapid clearance from the body. Two drawbacks can be cited: They are potentially degraded by endo- and/or exo-peptidases and they do not cross a normal BBB.

Different receptors overexpressed in tumor or endothelial cells that had been chosen for cell targeting are described in this review: Neuropilin-1 (NRP-1), $\alpha_v\beta_3$ integrins, nucleolin membrane receptor, epidermal growth factor (EGF), protein-glutamine-gamma-glutamyltransferase (TGM2), p32, as well as transferrin and mitochondrial membrane. The use of a specific cell absorbing-peptide is also described.

2 Nanoparticles loaded with photosensitizer and coupled to peptide

2.1 Peptides targeting neuropilin-1 receptor

2.1.1 NPs@PS@ATWLPPR

The neuropilin-1 (NRP-1) is a transmembrane glycoprotein and a coreceptor of the vascular endothelial growth factor receptor (VEGFR). It is involved in the axon guidance, angiogenesis, and immune responses [24]. NRP-1 is over-expressed in many types of cancers such as colon carcinoma, prostate, pancreatic carcinoma, lung carcinoma, melanoma, astrocytoma, and neuroblastoma [25].

NRP-1 has been described as a potential target against glioblastoma [26]. A high NRP-1 expression in a glioblastoma sample is correlated with increased malignancy. In contrast, NRP-1 under-expression is associated to lower cancer stem cell migration and proliferation *in vitro*, and to reduce tumor growth, *in vivo*. The enhanced NRP-1 expression has been observed in endothelial cells and is correlated to the development of tumor neovascularization [27, 28]. Vascular targeted photodynamic therapy (VTP) was applied using ATWLPPR heptapeptide as a part of specific NRP-1 recognizing sequence. Linked by a spacer arm (6-aminohexanoic acid, Ahx) to chlorin PS, the peptide accumulated in the tumor tissue and potentiated the photodynamic activity. However, the biodistribution studies conducted on mice demonstrated a rapid uptake of the peptide by the liver and the spleen. Consequently, 2 h after intravenous injection (IV), 85% of the total amount of the compound was degraded in the liver [29]. Since the peptide arm, conjugated to the PS, was responsible for its selectivity, the degradation of this peptide fragment was related to the decrease in the PS accumulation in the tumor tissue [30].

In order to reduce the hepato-splenic clearance and peptide degradation, functionalized silica-based NPs, grafted with ATWLPPR-peptide by hydrophilic polymer, were designed for vessel targeting. The NP was also designed as a magnetic resonance imaging (MRI) contrast agent, since it is composed of a silica shell coupled to polyethylene glycol (PEG), doped with gadolinium oxide (Gd_2O_3). The PS was a chlorin derivative, 5-(4-carboxyphenyl)-10, 15, 20 triphenylchlorin (TPC), substituted with a succinimidyl ester. In brief, aminopropyltriethoxysilane (APTES) reacted with PEG or propylenediaminetetra-acetic acid (PDTA) containing Gd_2O_3 and was cycle-hydrolysis to obtain the NPs (referred to as NP-TPC) [31–33] (Figure 2(A)). The size of the NPs was estimated between 3.3 and 3.8 nm [31, 33]. The coupling of the peptide (referred to as NP-TPC-ATWLPPR) raised the NPs' size to 4.6 ± 3.8 nm. NP-TPC-ATWLPPR was tested for their affinity to NRP-1 using biotinylated VEGF in competitive binding assays. The IC_{50} values were estimated to be 27 and $56.6 \mu M$ for NP-TPC-ATWLPPR and NP-TPC, respectively. The photocytotoxic effect was tested on human breast MDA-MB-231 cells that overexpress a high level of NRP-1. The calculated LD_{50} (Light dose) for P-TPC-ATWLPPR was estimated at $2.8\text{--}5.0 J cm^{-2}$ when cells were treated with $1 \mu M$ of NP-TPC-ATWLPPR (power 0.7 W, irradiance $4.54 J cm^{-2}$). The LD_{50} value was close to that obtained by a similar treatment with $1 \mu M$ NP-TPC [31, 32]. *In vivo*, the maximal MRI enhancement was found at 2–7 min, after the IV injection of NP-TPC-ATWLPPR in nude mice. The biodistribution, analyzed 75 min after the IV injection, suggested both renal

and hepatic clearance for NP-TPC and NP-TPC-ATWLPPR. However, the renal elimination was higher for NP-TPC. The exposure of the tumor U87 grafted cells to NP-TPC-ATWLPPR, revealed that the NPs targeted the peripheral vessels surrounding the tumors in accordance with the high expression of NRP-1 observed in endothelial cells [31, 32] (Figure 2(B)).

2.1.2 NPs@PS@KDKPPR

Based on the sequence homology of the natural ligand of NRP-1, VEGF-A165, a screening of several peptides was performed. Among the selected sequences, KDKPPR peptide showed a higher affinity to NRP-1 than ATWLPPR; the inhibitor dissociation constant (K_i) was estimated to be $9.0 \times 10^{-8} \text{ mol L}^{-1}$ for the former as compared to $1.4 \times 10^{-4} \text{ mol L}^{-1}$ for the latter [34]. The measurement of the affinity to NRP-1 for the K(P1)DKPPR conjugate (*i.e.* monocarboxylic tetraphenyl porphyrin, P1COOH, linked to the first ϵ -NH₂ lysine of KDKPPR) was 6 versus 171 μM for the P1-ATWLPPR complexes [35, 36].

The K(Pyro)DKPPR conjugate, using pypropheophorbide-a (Pyro) as PS, was coupled to PEGylated gold nanorods (AuNRs@PEG) through a thiol-maleimide (MI) click reaction to attain a combined hyperthermia and PDT effect (Figure 3) [37]. The AuNRs were functionalized with PEG to prevent any cytotoxicity. The AuNRs@PEG-MI-K(Pyro)DKPPR, illustrated in Figure 3, possessed a length of about 44 nm and a width of about 8 nm. The photophysical properties of the free Pyro were preserved in AuNRs@PEG-MI-K(Pyro)DKPPR, thus showing an unmodified visible absorption profile, a good fluorescence intensity ($\phi_F = 0.30$ in EtOH versus 0.38 for Pyro) and a preserved $^1\text{O}_2$ production ($\phi_0 = 0.40$ in EtOH versus 0.51 for Pyro).

The affinity of the AuNRs@PEG-MI-K(Pyro)DKPPR and the K(Pyro)DKPPR free peptide to recombinant NRP-1

was evaluated by competitive binding assay giving IC₅₀ values of 1.5 and 2.0 μM , respectively. The efficacy of AuNRs@PEG-MI-K(Pyro)DKPPR was tested *in vitro* on human glioblastoma U87 MG cells. No cytotoxicity was obtained with concentrations up to 30 μM (concentration relative to PS), in contrast to the cells treated with the PS alone. A good photodynamic efficiency was found when cells were treated with 30 μM of AuNRs@PEG-MI-K(Pyro)DKPPR for 24 h and then exposed to light irradiation at 652 nm (Fluence 10 J cm⁻², fluence rate 4.54 mW cm⁻²) with a 67% decrease in cell viability. This result supported the effect of both photodynamic and photothermal (PTT) therapies due to the presence of Gold.

The same methodology was also used to graft K(P1)DKPPR conjugate on multifunctional NP platform, namely AGuIX[®] [38–40]. The designed NPs were first proposed as nontoxic resonance magnetic agents for their imaging properties [41]. The so-called AGuIX@MI-K(P1)DKPPR NPs, illustrated in Figure 4, were tested for vascular-targeted interstitial photodynamic therapy (iPDT), using human umbilical vein endothelial cells (HUVEC) as an *in vitro* model and human U87 grafted tumors in rodents [38, 39].

AGuIX@MI-K(P1)DKPPR NPs had a hydrodynamic diameter of approximately 10 nm, making them particularly suitable for rapid renal elimination [42]. The fluorescence ($\phi_F = 0.7$ for P1COOH and $\phi_F = 0.1$ for AGuIX@MI-K(P1)DKPPR in D₂O) and singlet oxygen ($\phi_0 = 0.24$ for P1COOH and $\phi_0 = 0.28$ for AGuIX@MI-K(P1)DKPPR in D₂O) quantum yields of P1COOH PS were not altered after the peptide addition, demonstrating that the PS could be photoactivated to produce a photocytotoxic effect *in vitro* and *in vivo*.

HUVEC cell exposure to AGuIX@MI-K(P1)DKPPR NPs showed no dark cytotoxicity at PS concentrations up to 10 μM . However, the affinity to NRP-1 was altered as the peptide was coupled to the NPs (19 μM for

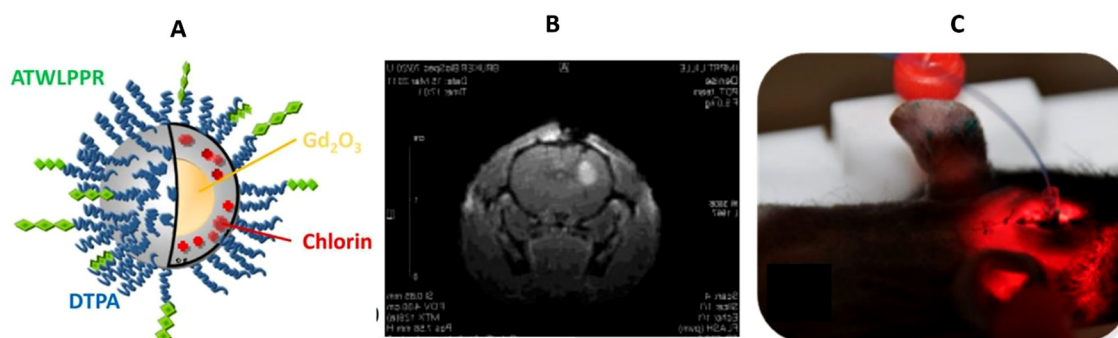


Figure 2: (A) Schematic presentation of NP-TPC-ATWLPPR, (B) maximal MRI signal intensity after injecting 84.2 μmol of Gd for a body weight of 250 g for cerebral biodistribution and brain tumor tissue selectivity of NP-TPC-ATWLPPR, and (C) overview clinical picture of the device applied on the mice [32] with permission from Elsevier and Copyright Clearance Center.

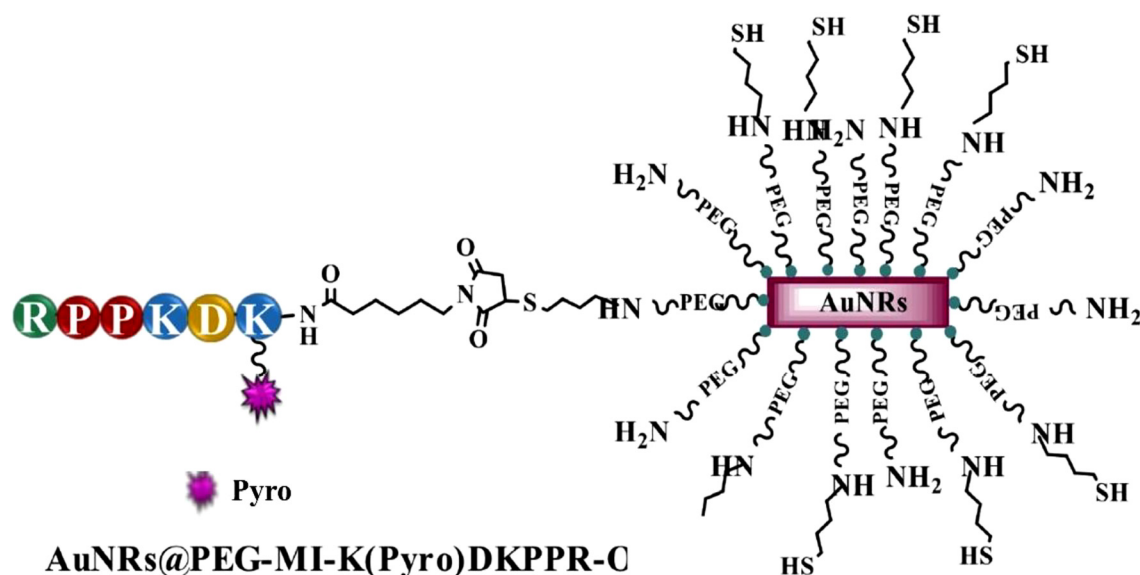


Figure 3: Schematization of AuNRs@PEG-MI-K(Pyro)DKPPR.

Adapted from Youssef et al. [24].

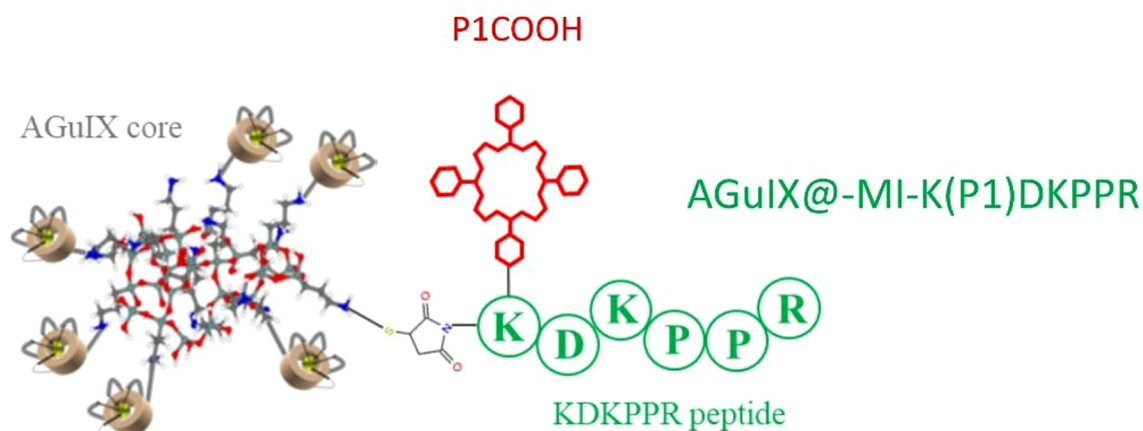


Figure 4: Schematic presentation of AGuIX@MI-K(P1)DKPPR NPs.

Adapted from Thomas et al. [39].

AGuIX@MIK(P1)DKPPR versus 2 μM for the peptide alone). Similar changes were observed when the affinity of AGuIX@MI-K(P1)DKPPR was assessed for human and rat NRP-1. Using the Biacore technology based on the surface plasmon resonance (SPR), the K_i values were estimated at 0.5 μM for KDKPPR and 4.7 μM for AGuIX@MI-K(P1)DKPPR for human NRP-1. For mice NRP-1 cells, the K_i values were estimated at 8.7 μM for KDKPPR and 25.2 μM for AGuIX@MI-K(P1)DKPPR. The use of a scramble peptide (KRPKPD) revealed no binding to recombinant NRP-1 protein, in contrast to the KDKPPR peptide. The specificity of the AGuIX@MI-K(P1)DKPPR NPs was validated using HUVEC overexpressing NRP-1.

The incorporation of AGuIX@MI-K(P1)DKPPR NPs into the cells was increased twice when compared to the NPs carrying the scramble peptide (*i.e.* AGuIX@MI-K(P1)RKPDP NPs).

In vivo, the distribution of AGuIX@MI-K(P1)DKPPR NPs was assessed in rodents, rats and mice, 96 h post-IV injection of 4 $\mu\text{mol kg}^{-1}$ (PS equivalent) corresponding to 55 $\mu\text{mol kg}^{-1}$ (Gd equivalent). Throughout the experimental delay, no signs of clinical toxicity were observed. Ninety six hours post-IV injection, the fluorescence signal was mainly found in the organs of excretion such as the liver, bladder and kidneys. However, the contrast enhancement of Gd quantification was only observed in the kidneys and

bladder. The selectivity of the AGuIX@MI-K(P1)DKPPR NPs to the tumor, compared to the healthy brain parenchyma, was validated in nude rats. This was applied on an orthotopic tumor developed from human glioblastoma U87 grafted cells, followed by MRI (T1 sequences). The selectivity of the AGuIX@MI-K(P1)DKPPR NPs towards the tumor vascular endothelium after IV injection was also assessed in nude mouse model either with dorsal chamber or cranial window. Nontargeting NPs (i.e. AGuIX@P1 without peptide and AGuIX@-MI-K(P1)RPKPD with scramble peptide) were visualized in the blood vessels 1 h after injection but disappeared after 4 h due to the fenestration of the tumor vascular system (Figure 5). In contrast, AGuIX@MI-K(P1)DKPPR NPs were more localized on the tumor vessel walls 1 h after injection and were still present after 24 h.

In addition, the efficacy of the treatment with the AGuIX@MI-K(P1)DKPPR NPs was studied by iPDT

performed on nude rats with a cranial anchor (Figure 6). This vascular targeting strategy decreased the tumor growth and extended the rats' survival rate from seven days, as in the case of AGuIX@P1 NPs, to 13 days ($P < 0.0001$). This result was associated with decreased tumor metabolism after treatment.

In the field of brain tumors, the susceptibility weighted imaging (SWI) has recently been examined for glioma imaging [43, 44]. These recent studies showed that SWI can help in the glioma classification thanks to its high sensitivity to the microhemorrhage and the microvascularization itself, which correlates with the tumor grade. After VTP using AGuIX@-MI-K(P1)DKPPR NPs, the onset of microhemorrhages was rapid, occurring within the first few minutes (Figure 7(A)). Specifically, hemorrhages were concentrated at the tumor periphery as early as 1 h after treatment and tended to resolve within 24–48 h post-treatment (Figure 7(B) and (C)). This observation was

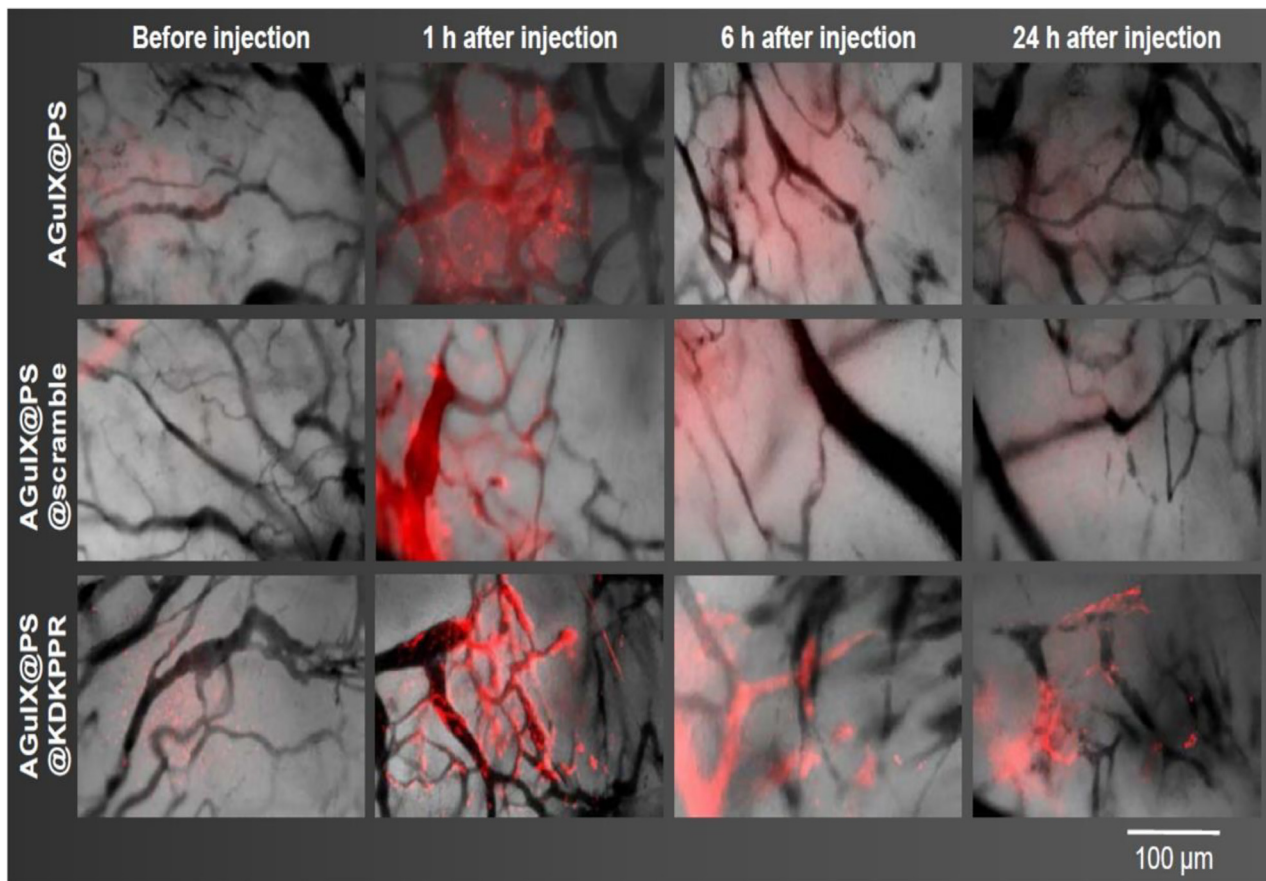


Figure 5: *In vivo* selectivity: selectivity of NPs using a dorsal skinfold chamber model, before and 1, 6, and 24 h after IV injection of AGuIX@P1, AGuIX@MI-K(P1)RPKPD and AGuIX@MI-K(P1)DKPPR ([P1] = 6 µmol/kg). Blood vessels are represented in black and P1 fluorescence in red. On the contrary to AGuIX@P1 or AGuIX@MI-K(P1)RPKPD NPs, thanks to the targeting peptide, AGuIX@MI-K(P1)DKPPR NPs were fixed to the vessel walls of the tumor tissue.

All pictures have been taken with the same magnification; scale bar represents 100 µm [38].

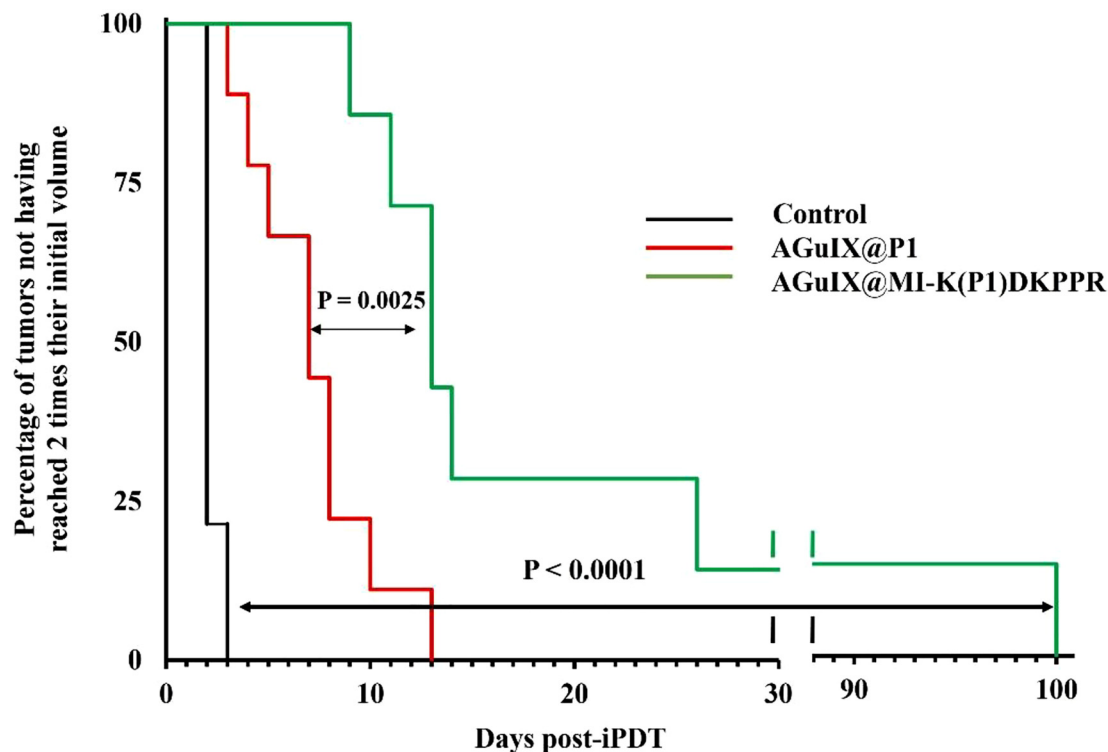


Figure 6: Kaplan–Meier curves of control rats or rats treated by iPDT using AGuIX@P1 NPs (in red) or AGuIX@MI-K(P1)DKPPR (in green), considering the percentage of tumors not having reached two times their initial volume at the end point. At least seven animals were used for each experimental group. Statistical analysis was performed using the Log rank test and highlighted a statistically significantly difference between AGuIX@MI-K(P1)DKPPR group and control group ($P < 0.0001$) and between AGuIX@P1 ($P = 0.0025$). Adapted from Gries et al. [39].

consistent with the localization of the NRP-1 protein which was mainly expressed in the vessels of the tumor periphery and sometimes at the stromal level [32, 45]. The vascular impact of the treatment was restricted to the tumor borders and it did not affect the vessels of the healthy brain tissues, validating the selectivity of the targeting using the DKPPR peptide.

Recently, the designing of NPs coupled to different NRP-1 targeting peptides was performed by two other teams. They used CRGDK and tLyp-1 peptides covalently coupled to the NPs.

2.1.3 NPs@PS@CRGDK

Zhao et al. designed a very interesting multifunctional nanosystem composed of PEG-PCL (polyethylene glycol-poly(α -caprolactone)) NPs encapsulating the IR780 PS and the oxygen depot perfluorooctyl bromide (PFOB), and covalently coupled to the tumor homing peptide CRGDK. IR780 was used for its near-infrared light absorption and high fluorescence imaging capability and PFOB was chosen for oxygen storage.

By measuring the $^1\text{O}_2$ formation in solution *via* singlet oxygen sensor green (SOSG), they observed that the presence of PFOB enriched the environmental O_2 and decreased the hypoxia. In MDA-MB-231 human breast cancer cell line, the fluorescence of dichloro-dihydro-fluorescein diacetate (DCFH-DA) was 1.8 times greater for CRGDK-targeted NPs than the untargeted ones. In MCF-7 resistant human breast adenocarcinoma cell line, no difference between the two types of NPs was observed. These results were in correlation with the NRP-1 expression level which is high in MDA-MB-231 cells and low in MCF-7 cells. By adding anti NRP-1-monoclonal antibodies, the cellular incorporation of CRGDK targeted NPs strongly decreased. Multicellular tumor spheroids of HT-29 cells overexpressing NRP-1 receptor were prepared and incubated with the CRGDK-targeted NPs. For the NPs holding PFOB, the DCFH-DA fluorescence was detected in the whole sphere at the depth of 65 nm, whereas it was only observed at the edge of the tumor spheroid for the NPs lacking PFOB. However, no fluorescence was observed when the CRGDK-targeted NPs were incubated in multicellular tumor spheroids of MCF-7 with low expression of NRP-1 receptor. *In vivo* experiments in BALB/c nude mice bearing

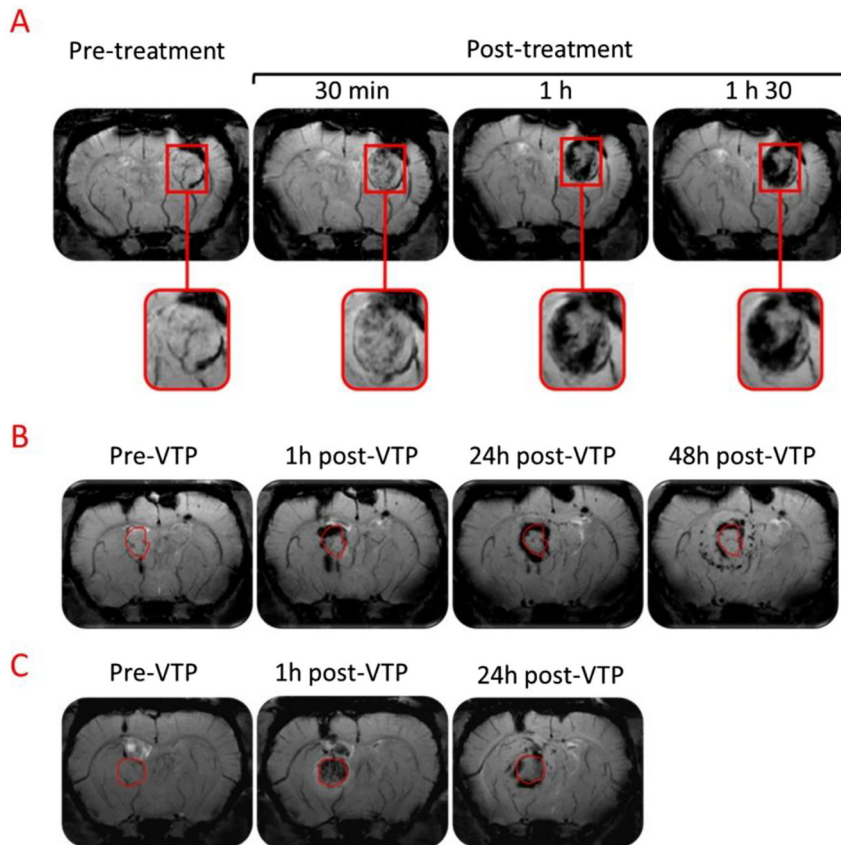


Figure 7: Formation of microhemorrhages after VTP.

The rat with human glioblastoma (U87) was treated with VTP (40 mW, 8 min 40 s, 20.8 J), 4 h after IV injection of AGuIX@MI-K(P1) DKPPR NPs ($1.75 \mu\text{mol kg}^{-1}$, PS equivalent). Short (A) and medium (B–C) term monitoring of microhemorrhages was performed by MRI using a magnetic susceptibility sequence (SWI), which is extremely sensitive to venous blood, hemorrhages and iron storage. The diameter of the tumor visible in T2 at pretreatment was reported on the SWI images (in red).

MDA-MB-231 tumor were conducted, where it was proved that the CRGDK-targeted NPs accumulated in tumor with a tumor-to-total organs ratio of 25%. After IV-injection, the fluorescence signal of IR780 was at the tumor periphery in the case of nontargeted NPs, however, with the CRGDK-targeted NPs, the signal occupied the whole tumor tissue. Indeed, CRGDK-targeted NPs could spread from the vascularized periphery to the avascular tumor area. Using a hypoxia marker (hypoxia-inducible factor (HIF)-1 α), it was proved that the tumor hypoxia decreased due to the presence of PFOB. To evaluate the phototoxicity, PDT treatment was performed at 808 nm (2 W cm^{-2} , 20 s) 24 h post-injection. As expected, the best efficiency was obtained with the CRGDK-targeted NPs (Figure 8) [45].

2.1.4 NPs@PS@tLyp1

In 2016, Jiang and coworkers designed a new targeted drug delivery system consisting of a PS (chlorin e6, Ce6, 3.8% loading capacity) chemically incorporated in the shell of D- α -tocopheryl polyethylene glycol 1000 succinate-poly(lactic acid) NPs (TPGS-PLA NPs). These

NPs were surface-decorated with CGNKRTR (tLyp-1), a tumor homing and penetrating peptide, to target NRP-1 receptor. The resulted spherical tLyp-1 NPs possessed an average size of around 140 nm. They encapsulated therein a chemo-drug (Doxorubicin, Dox, 9.56% loading capacity). The NPs were then used for chemo-photodynamic combination therapy of Dox-resistant breast cancer. In this combination therapy, the PS played multiple roles. On the one hand, it induced cell apoptosis by PDT. On the other hand, it disrupted the endolysosome membranes to release the encapsulated chemo-drug directly into cytoplasm for an enhanced treatment efficiency in drug-resistant cancers. The *in vitro* studies on HUVEC and Dox-resistant human breast adenocarcinoma cells (MCF-7/ADR) revealed a cellular uptake enhancement and a photocytotoxicity improvement of tLyp-1 NPs compared to untargeted NPs (660 nm laser irradiation). The *in vivo* studies on mice bearing MCF-7/ADR tumors demonstrated the targeting efficiency and the penetrative ability of tLyp-1 NPs. This resulted in a considerable accumulation of the PS and Dox into the drug resistant tumors, and thus a more efficient chemo-photodynamic combination

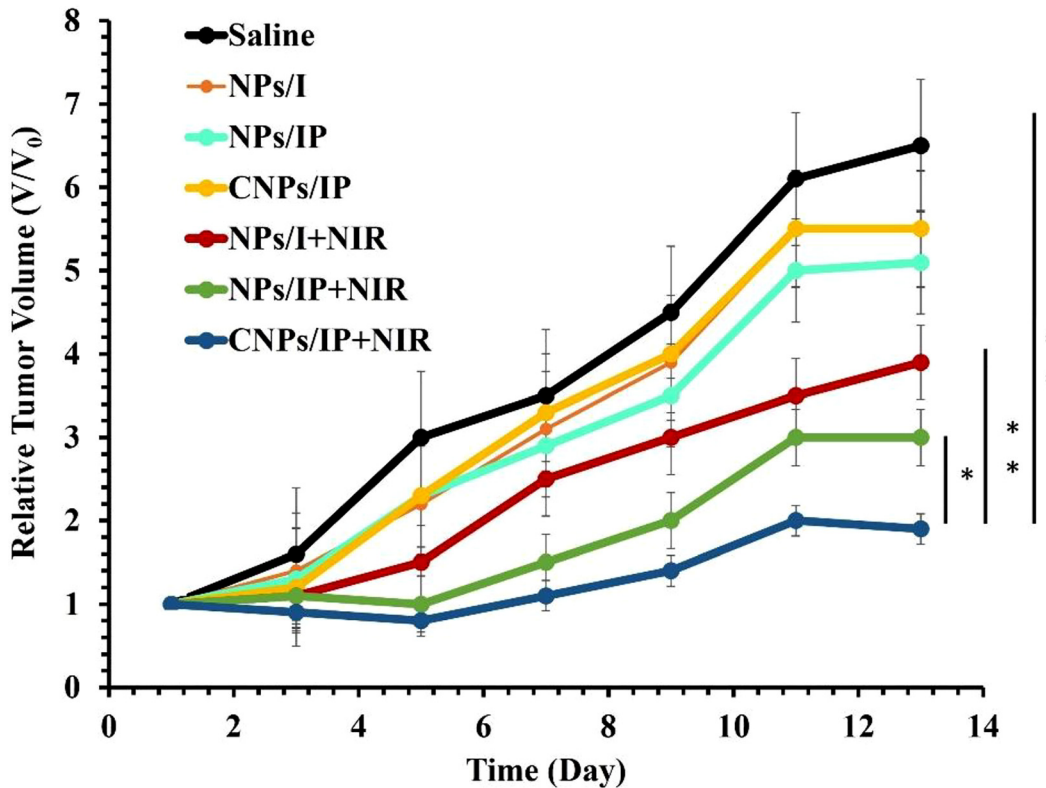


Figure 8: Tumor growth curves in mice treated *in vivo* on an MDA-MB-231 tumor model with saline solution, NPs/I with or without laser irradiation, NPs/IP with or without laser irradiation, and CNPs/IP with or without laser irradiation. The values are expressed as mean \pm SD, ($n = 5$, $*P < 0.01$, $**P < 0.005$, Student's *t*-test).

After 24 h, the tumors in laser treated groups were irradiated by an 808 nm laser with a power of 2 W cm^{-2} for 20 s. *I* = IR780, *P* = Perfluorooctyl bromide (PFOB), *NPs* = PEG-PCL (polyethylene glycol-poly (α -caprolactone)), *C* = CRGDK, V_0 = Initial tumoral volume before treatment [45].

treatment. An increase in the antitumor efficiency was detected with tLyp-1 NPs exposed to Laser (170 mW cm^{-2}) for 9.8 min at 660 nm (Figure 9) [46].

Table 1 describes the NPs@PS@peptide systems, targeting NRP-1 receptors, regarding the types of NPs, PSs, and the coupling between them, in addition to the NPs size, excitation wavelength ($\lambda_{\text{excitation}}$), fluorescence quantum yield (ϕ_F), singlet oxygen quantum yield ($\Delta_{0,S}$) and the results obtained *in vitro* and/or *in vivo*.

2.2 Peptides targeting $\alpha_v\beta_3$ integrins

$\alpha_v\beta_3$ integrins are involved in the tumor angiogenesis and are highly expressed on activated endothelial cells and some tumor cells. However, they are not present in resting endothelial cells and most of the normal organ systems, making them interesting targets for anti angiogenic PDT [48].

2.2.1 NPs@PS@RGD

Arginyl-glycyl-aspartic acid (RGD) is a well-known peptide targeting $\alpha_v\beta_3$ integrins.

In 2014, Wang et al. reported the synthesis of lipid coated upconverting NPs (UCNs). The coating was constituted of RGD peptide functionalized by PMAO (poly(maleic anhydride-alt-1-octadecene)) grafted DOPE (dioleoyl L - α -phosphatidylethanolamine) (UCN/RGD-PMAO-DOPE). Dextran merocyanine 540 (MC540) PS was adsorbed onto these NPs by hydrophobic interactions (MC540@UCN/RGD-PMAO-DOPE). These upconverting NPs were monodispersed and presented a size of 20 nm. The amphiphilic lipid polymer coating was used to improve the hydrophilic properties of the UCNs' surface, and protect the drug, by electrostatic repulsion, from aggregation and leakage during the transport. The *in vitro* experiments were performed on MCF-7 cells overexpressing $\alpha_v\beta_3$ integrins. ROS, mainly $^1\text{O}_2$, were more importantly produced by

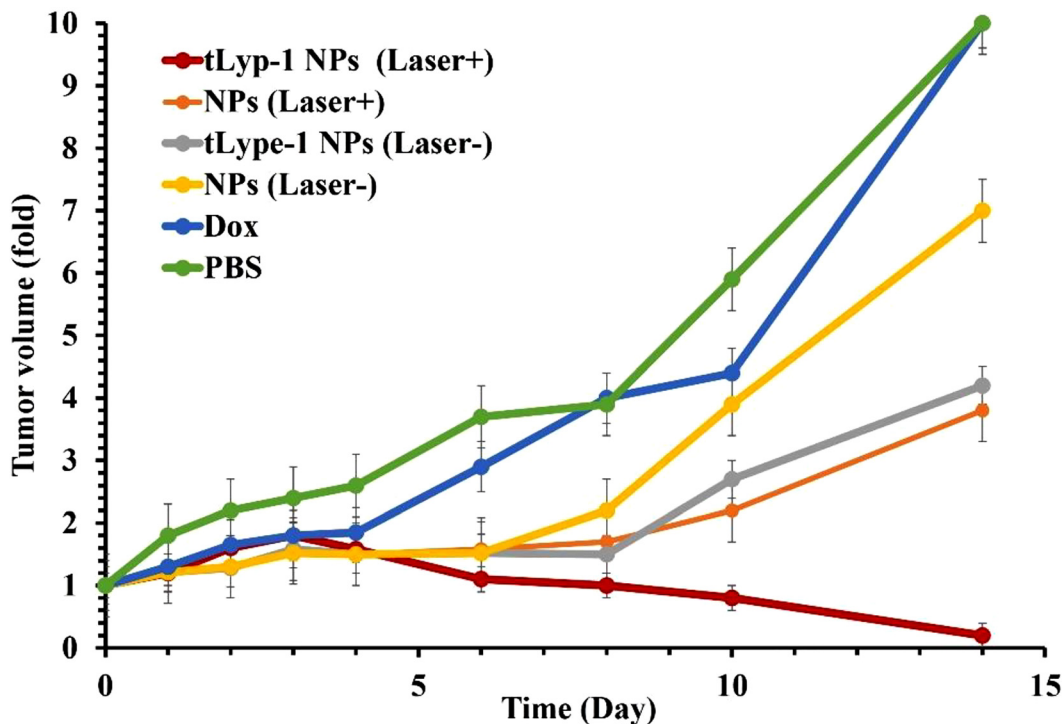


Figure 9: Tumor growth curves showing the antitumor efficiency of PBS, Free Dox, NPs with Ce6, and Dox without tLyp-1 in the surface (NPs), NPs with Ce6 and Dox with tLyp-1 in the surface (tLyp-1 NPs) with (Laser+) or without (Laser-) irradiation (170 mW cm^{-2} for 9.8 min, 660 nm). Adapted from Jiang et al. [46].

MC540@UCN/PMAO-DOPE decorated by RGD peptide (MC540@UCN/RGD-PMAO-DOPE) as compared to NPs lacking RGD (MC540@UCN/PMAO-DOPE). This was attributed to the role of RGD in enhancing the cellular uptake of the NPs through receptor-mediated endocytosis. The production of ROS proved the successful energy transfer from the UCNs to the MC540 PS. In addition, MC540@UCN/RGD-PMAO-DOPE were capable of decreasing the cell viability to 35% after exposure to 980 nm laser for 30 min, thus revealing a more efficient photodynamic effect as compared to MC540@UCN/PMAO-DOPE (65% cell viability) (Figure 10). These results verified that the efficiency of PDT was enhanced by the presence of the RGD peptide [49].

In 2018, Yuan et al. reported a new platform based on mesoporous silica NPs (MSN). Black hole quenchers (BHQs) were doped in the inner walls of the MSN mesopores (MSN-BHQ). The resulted NPs were coupled to photoporphyrin (PpIX) PS through a disulfide bond (SS) to afford MSN-BHQ-SS-PpIX. To prolong their blood circulation time, PEG was coupled to PpIX onto the NPs (MSN-BHQ-SS-PpIX-PEG). A specific targeting agent, RGD peptide, was then conjugated to this nanoplatform (MSN-BHQ-SS-PpIX-PEG-RGD). The MSN-BHQ-SS-PpIX-PEG-RGD NPs had a spherical morphology with an average size of 50 nm. An oxidation–reduction reaction

on this platform stimulated the glutathione (GSH)-mediated release of the therapeutic drug by breaking the SS link. GSH is present in large quantities in the tumor cells, which allowed accelerating the release of the drugs. *In vitro* experiments were performed on cervical cancer cells (HeLa). The fluorescence of MSN-BHQ-SS-PpIX-PEG-RGD was higher than that of free RGD. The cellular incorporation of MSN-BHQ-SS-PpIX-PEG-RGD was measured in HeLa cells with and without GSH. With extra GSH, many red fluorescent spots appeared in the cytoplasm mainly around the nucleus. When tested on two other cell lines (SCC-7 and COS7), MSN-BHQ-SS-PpIX-PEG-RGD showed low cytotoxicity in the dark and good phototoxicity in the presence of light (Figure 11). In conclusion, MSN-BHQ-SS-PpIX-PEG-RGD selectively targeted the tumor environment due to the presence of RGD. This selective toxicity was reinforced by GSH. The redox response of this nanoplatform in the tumor environment made it an important candidate in anticancer PDT and in tumor imaging therapy [50].

In the same year, Hou et al. synthesized nanodumbbell ZnPc-UCN@lipid@RGD. Hydrophobic UCNs were transferred into water to form UCN@lipid. The UCN@lipid and zinc phthalocyanine (ZnPc) were both encapsulated into polymersome (PS) shell to form UCN@lipid@PS

Table 1: The summary of NPs conjugated with PSs and peptides targeting neuropiline-1 receptor in terms of different parameters.

NPs@PS@Peptide targeting neuropilin -1 (NRP-1)									
Reference	NPs	PS	Coupling between NPs and PS	NPs size (nm)	$\lambda_{excitation}$ (nm)	ϕ_F	$\Delta_{0,s}$	<i>in vitro</i>	<i>in vivo</i>
Peptide KDKPPR									
[38]	AGuIX®	Monocarboxylic porphyrin (P1COOH)	Maleimide	4.9 ± 1.4 for AGuIX®	652	0.07 for AGuIX@P1	0.58 for AGuIX@P1	HUVEC [38]	Nude rat with orthotopic U87 [38]
[39]				11.2 ± 3.9 for AGuIX@P1		0.1 for AGuIX@MI-K(P1)DKPPR	0.28 for AGuIX@MI-K(P1)DKPPR	U87 [39]	Recombinant rat [39]
				11.6 ± 6.3 for AGuIX@MI-K(P1)DKPPR		0.09 for AGuIX@MI-K(P1)DKPPR	0.35 for AGuIX@MI-K(P1)DKPPR		
				10.6 ± 2.3 for AGuIX@MI-K(P1)DKPPR		RPKPD In H ₂ O	RPKPD In D ₂ O		
	AuNRs	Pyropheophorbide-a (Pyro)	Maleimide	AuNRs@PEG: 44.8	652	0.38 for Pyro	0.51 for Pyro	U87	nd
						0.30 for AuNRs@PEG-MI-K(Pyro)DKPPR	0.40 for AuNRs@PEG-MI-K(Pyro)DKPPR		
						In toluene	In EtOH		
Peptide ATWLPPR									
[31]	Silica shell	gadolinium 5-(4-carboxyphenyl)-	Amide bond	4.6 ± 3.8 for NP-TPC-ATWLPPR	652	0.19 ± 0.02 for NP-TPC-ATWLPPR	0.66 ± 0.05 for NP-TPC-ATWLPPR	MDA-MB-231	Male athymic nude rats with U87 tumor
[32]	oxide core	10,15,20-triphenyl-chlorin (TPC)				0.18 ± 0.05 for NP-TPC	and NP-TPC		
[47]						NP-TPC 0.21 ± 0.05 for TPC	0.69 ± 0.05 for TPC		
						for TPC in ethanol	in ethanol		
Peptide CRGDK									
[45]	PEG-PCL (polyethylene glycol-poly (α-caprolactone))	IR780	Encapsulation	201.5 ± 4.7 for CNPs/IP	808	nd	nd	MDA-MB-231, MCF-7, HT-29	BALB/c nude mice bearing MDA-MB-231 tumor
Peptide tlyp-1									
[46]	TPGS-PLA (D-α-tocopheryl polyethylene glycol 1000 succinate-poly(lactic acid))	Chlorin e6 (Ce6)	Ester bond	140.3 ± 13.45 for tlyp-1 NPs	660	nd	nd	HUVEC, MCF-7/ADR	Mice bearing MCF-7/ADR tumor

nd, not determined.

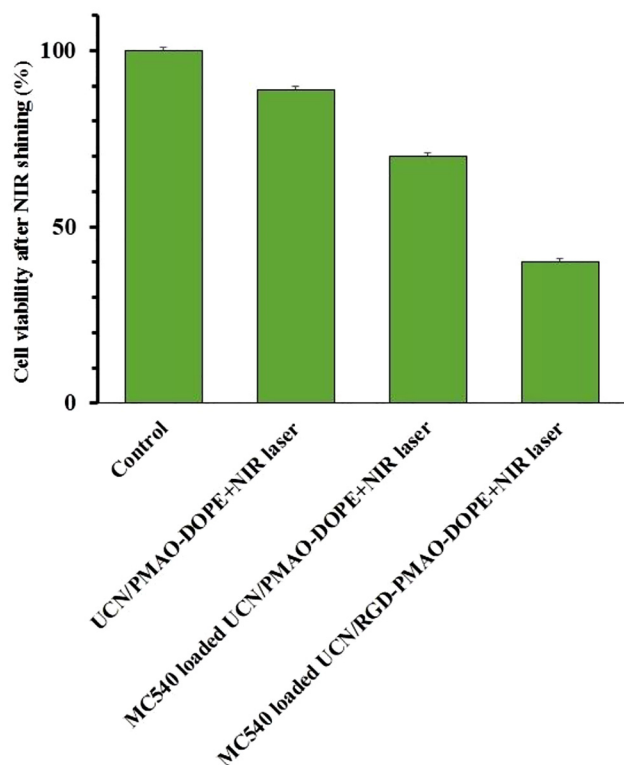


Figure 10: PDT treatment efficiency on MCF-7 cells. Untreated cells as control group and cells treated with UCN/PMAO-DOPE NPs, MC540 loaded UCN/PMAO-DOPE NPs or MC540 loaded UCN/RGD-PMAO-DOPE NPs after NIR laser irradiation (980 nm, 30 min). Adapted from Wang et al. [49].

nanodumbbell. The exterior of the polymersome possessed many carboxyl functional groups that were coupled to RGD peptide. The UCN's core converted the NIR rays into visible ones, thus overcoming the problem of the limited light penetration into tissues. The ZnPc-UCN@lipid@PS had a high drug loading efficiency of 18.03%. The transmission electron microscopy (TEM) showed that the ZnPc-UCN@lipid@PS were of spherical form with a size of 150 nm. Whereas, the dynamic light scattering (DLS) gave an average diameter of 195 nm. After coupling the UCNs to ZnPc, the fluorescence intensity of the UCNs decreased, indicating an energy transfer between the UCNs and ZnPc. Following the excitation at 980 nm, ZnPc-UCN@lipid@PS and ZnPc-UCN@lipid@PS-RGD showed the greatest production of 1O_2 . These tests were carried out using 9,10-anthracenediyl-bis(methylene)dimalonic acid (ABDA) probe. The study of the *in vitro* cytotoxicity in HeLa cells exposed to different concentrations of NPs, showed a greater biocompatibility in the case of UCN@lipid@PS-RGD (97% of cell viability for $500 \mu\text{g mL}^{-1}$

of NPs) as compared to UCN@lipid@PS (90%) and UCN@lipid (65%). This result was credited to the presence of RGD that induced the specific incorporation of the NPs in the cells, and hence decreased the unwanted cytotoxicity (Figure 12(A)). After incubation with HeLa cells and excitation with a NIR source (980 nm, 1.5 W cm^{-2}), ZnPc-UCN@lipid@PS-RGD showed the lowest tumor cell viability as compared to the untreated control cells and those exposed to the other ZnPc loaded-PS NPs (ZnPc-UCN@lipid@PS, UCN@lipid@PS nanodumbbells) (Figure 12(B) and (C)) [51]. In the same conditions, ZnPc loaded UCN@lipid@PS with and without RGD showed the best and higher production of singlet Oxygen in comparison with other couples detailed in Figure 12(C).

In 2015, Zhao et al. successfully synthesized a novel multi arm polymeric nanosystem for PDT (RGD-8PEG-IR700). The RGD and the IR700 units were coupled to a PEG arm (8 polyethylene glycol). The hydrodynamic diameter of the nanosystem was 6.6 nm. The *in vitro* results on spheroid tumor model A375 and SKOV3 cells that express $\alpha_v\beta_3$ integrins, showed a stronger fluorescence of the RGD-8PEG-IR700 NPs as compared to 8PEG-IR700. In contrast to IR700 and 8PEG-IR700, RGD-8PEG-IR700 induced a significant phototoxicity on A375 cells, under excitation at 504 nm with an IC_{50} value of 57.8 nM. No cytotoxic effect was observed in the dark even with a concentration of $1 \mu\text{M}$ (IR700 equivalent) (Figure 13) [52].

In 2015, Yuan et al. used the seventh generation poly (amidoamine) (PAMAM-G7, P) dendrimer of 8 nm. The PAMAM was coupled with Ce6 PS in addition to PEG or RGD, to obtain the PEG-P-Ce6 NPs and RGD-P-Ce6, respectively. The Φ_Δ was 2.5 times higher for RGD-P-Ce6 than free Ce6 in water. *In vitro* experiments were performed in A375 cells (nonpigmented melanoma cell line expressing $\alpha_v\beta_3$ integrins (+)) and NIH₃T₃ cells (mouse fibroblast that do not express $\alpha_v\beta_3$ integrins (-)). Cellular uptake in (+) A375 cells was 4.7-fold superior for targeted RGD-P-Ce6 than nontargeted PEG-P-Ce6 NPs, whereas the incorporation into (-) NIH₃T₃ cells was the same for both NPs. The photocytotoxicity was evaluated with various concentrations in both types of cells by illumination at 660 nm (3.5 mW cm^{-2} , 30 min). No cell killing was witnessed when A375 cells were treated with Ce6 due to its poor incorporation. RGD-P-Ce6 presented an enhanced phototoxicity in A375 cells compared to nontargeted NPs. As expected, in NIH₃T₃ cells, no difference in the phototoxicity between RGD-targeted NPs and PEG-P-Ce6 NPs was detected. The penetration of RGD-targeted NPs and free Ce6 was

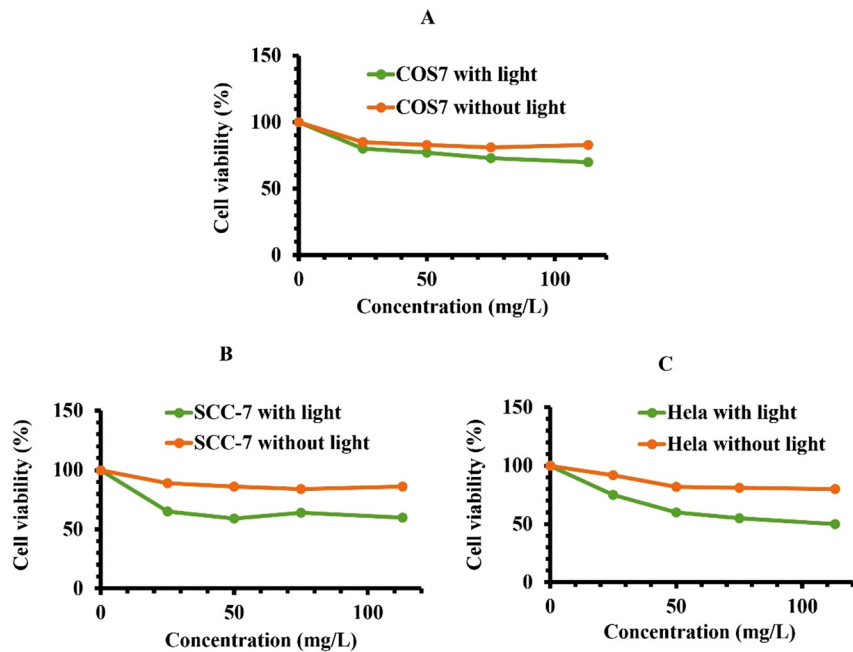


Figure 11: *In vitro* cell viability of (a) COS7, (b) SCC-7, and (c) HeLa cells incubated with different concentrations of MSN-BHQ-SS-PpIX-PEG-RGD without light and under 30 min. Data is shown as mean \pm SD ($n = 4$). Adapted from Yuan et al. [38].

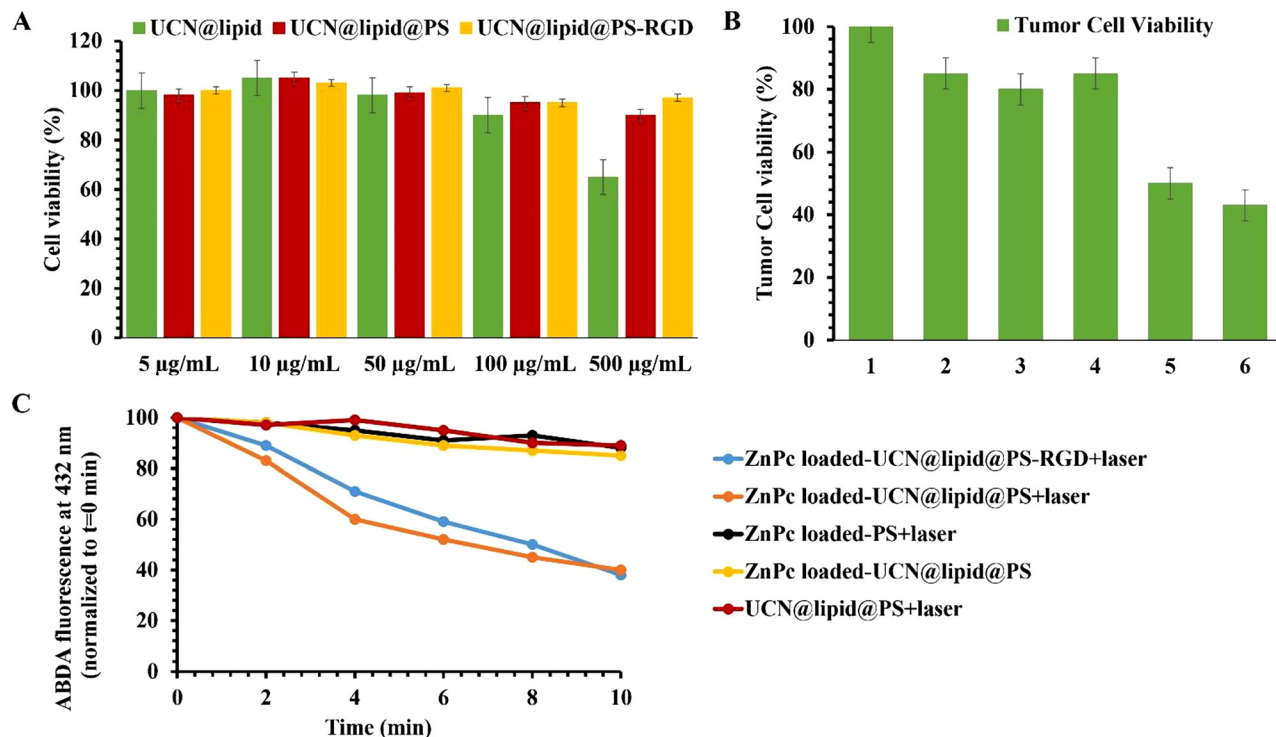


Figure 12: (A) Cytotoxicity on HeLa cells of UCN@lipid, UCN@lipid@PS, and UCN@lipid@PS-RGD. (B) Viability of HeLa cells treated with 1 PBS (Control group), 2 UCN@lipid@PS nanodumbbells plus NIR laser, 3 ZnPc loaded-PS NPs plus NIR laser, 4 (ZnPc + UCN@lipid)@PS NPs, 5 (ZnPc + UCN@lipid)@PS NPs plus NIR laser, 6 (ZnPc + UCN@lipid)@PS-RGD NPs plus NIR laser (980 nm, 1.5 W cm⁻²). The concentration is 500 µg mL⁻¹. (C) Comparison of ¹O₂ production between control groups and experiment groups. Adapted from Hou et al. [39].

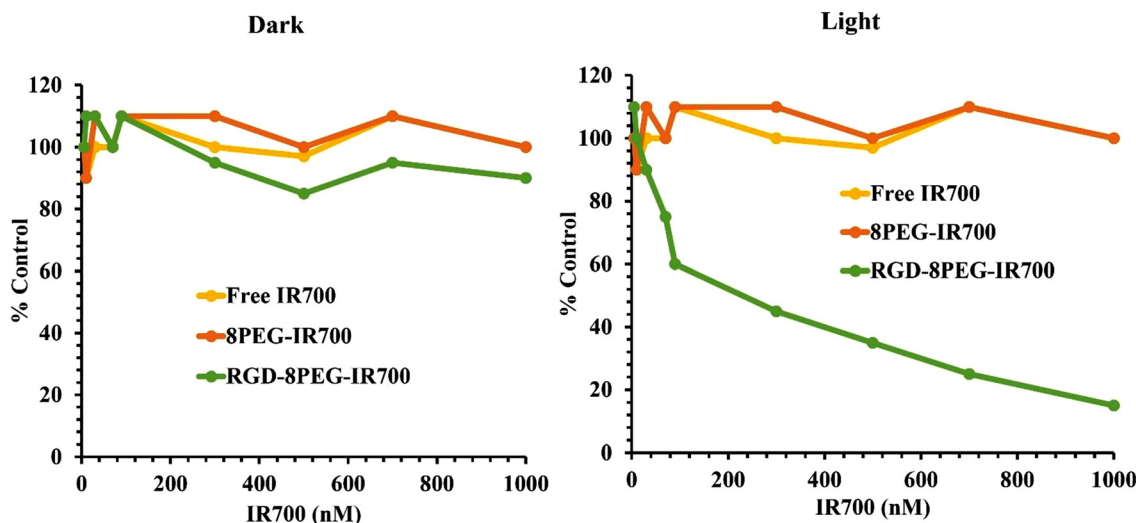


Figure 13: Determination of the dose-dependent (A) cytotoxicity and (B) phototoxicity of free IR700, 8PEG-IR700, and RGD-8PEG-IR700 in A375 cells. Light irradiation at 660 nm with 3.5 mW cm^{-2} for 30 min fluent rate. Adapted from Zhao et al. [40].

evaluated in A375 tumor spheroids. Using the same concentrations, *i.e.* 200, 400, and 800 nM, RGD-P-Ce6 showed a higher cellular uptake than free Ce6 with ratios of 40.8, 58.7, and 79.3, respectively (Figure 14) [53].

In 2017, Kim et al. [42] synthesized a nanoplatform consisting of C60 coupled to PEG and functionalized by Ce6 PS and cyclic RGD peptide (cyclic CKRGDf, denoted by cRGD). The nanosystem had a diameter of 3–4 nm. *In vitro* experiments were performed with SKOV-3 (high $\alpha_v\beta_3$ expression (+)) and KB (low $\alpha_v\beta_3$ expression (-)) cells [54]. After exposure to light (670 nm, 5.2 mW cm^{-2} , 10 min), the

highest cell death was observed in (+) SKOV-3 with the targeted NPs. As expected, free Ce6 and nontargeted NPs were less phototoxic in both SKOV-3 and KB cells. The phototoxicity of the targeted NPs was also reduced in (-) KB cells. The *in vivo* experiments using BALB/c nu/nu female mice with SKOV-3 and KB xenografted tumors proved that the targeted NPs had a lower uptake in KB than in SKOV-3 tumors. Due to the small size of the NPs and the EPR effect, both targeted and nontargeted NPs were incorporated into the tumors. However, the highest uptake was achieved by the targeted NPs in SKOV-3 tumor. After realizing PDT treatment on the cells incubated with targeted NPs (670 nm, 5.2 mW cm^{-2} , 40 min), the reached tumor volumes were 4.5 and 2.1 times smaller than those obtained in mice treated with Ce6 and nontargeted NPs, respectively.

In 2019, Shi et al. described the design of targeted RPTD/HP NPs made of chemo-drug Dox coupled to PEG, *via* a ROS-cleavable thioketal link, and a targeting cRGD peptide (cyclic RGDfC). This system also encapsulated hematoporphyrin (HP) PS (Figure 15) and was used for oral tongue squamous cell carcinoma treatment [55]. Due to the presence of both hydrophobic Dox and hydrophilic PEG, the molecules self-assembled to form RPTD/HP NPs with a size of about 180 nm.

In vivo studies were performed in HOEC (low $\alpha_v\beta_3$ integrin expression (-)) and CAL-27 (high $\alpha_v\beta_3$ integrin expression (+)) cells. The targeted RPTD/HP NPs were better incorporated in (+) CAL-27 than in (-) HOEC cells. After illumination (633 nm, 10 min, 100 mW cm^{-2}), the ROS

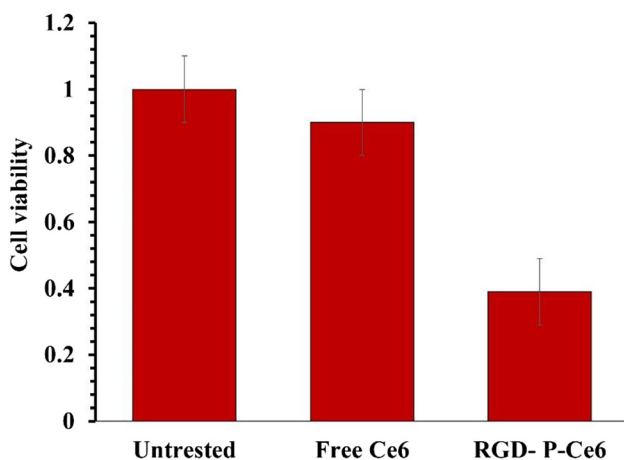


Figure 14: A375 Cell viability after PDT treatment (660 nm, 3.5 mW cm^{-2} , 30 min).

Adapted from Yuan et al. [41].

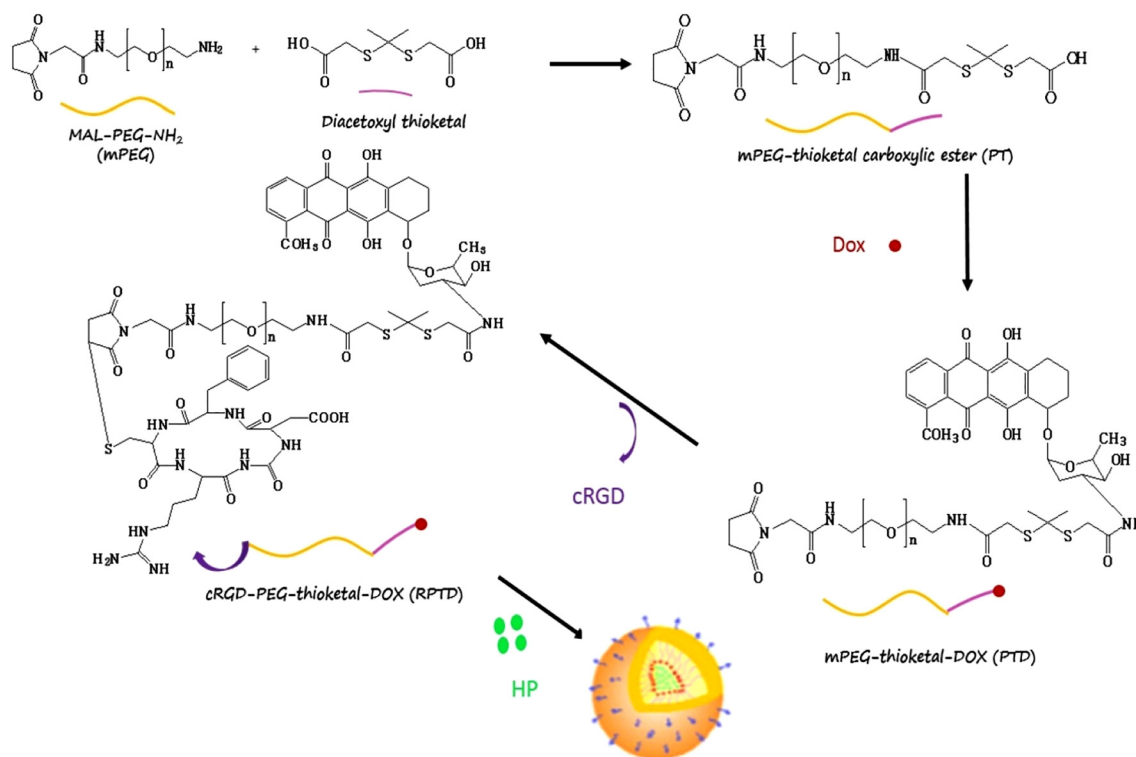


Figure 15: Synthesis of RPTD/HP NPs. Adapted from Shi et al. [55].

were formed, which triggered the cleavage of the thioketal bond. Consequently, the Dox was released and entered the nuclei of CAL-27 cells. Synergistic effects of PDT and chemotherapy was observed with both the targeted RPTD/HP and the nontargeted PTD/HP NPs with an IC_{50} value of 0.89 and 0.68 μM , respectively. Targeted RPTD/HP NPs displayed higher cytotoxicity and phototoxicity than nontargeted PTD/HP NPs, since they delivered more amounts of Dox and HP into the cells. The *in vivo* studies were implemented with free Dox, free HP, targeted RPTD/HP NPs, and nontargeted PTD/HP NPs in CAL-27 tumor bearing BALB/c nude mice. All the treatments inhibited the tumor growth to a certain extent when compared to the control. However, the best results were obtained with the targeted RPTD/HP NPs (Figure 16). In addition to that, these NPs displayed a strong effect on tumor angiogenesis [55].

2.2.2 NPs@PS@iRGD

Internalizing-RGD (iRGD, sequence: CRGDKGPDC) is a disulfide-based cyclic RGD peptide that targets integrin $\alpha_v\beta_3$ receptors. The process of tumor-targeting by the iRGD peptide takes place in several steps: First, iRGD is proteolytically cleaved by binding to the surface of cells

expressing α_v integrins ($\alpha_v\beta_3$ and $\alpha_v\beta_5$). This cleavage generates the CRGDK fragment, which then binds to NRP-1 and penetrates deeper into the tumor parenchyma. The affinity of iRGD for α_v integrins, compared to conventional RGD, is in the nanomolar range. Besides, the affinity of the CRGDK fragment is stronger for NRP-1 than for α_v integrins. This is due to the C-terminal exposure of a conditional C-end Rule (CendR) motif (R/KXXR/K). The receptor of this motif was proved to be NRP-1. On this basis, the CendR motif is able to bind to NRP-1, thus activating an endocytotic/exocytotic transport pathway that leads to a deeper penetration into the tumor [56].

In 2015, Yan et al. synthesized new NPs, named iRGD-ICG-LPs, by the thin-layer rehydration process [57]. These NPs were liposome-based (LP) in which the indocyanine green (ICG) PS was encapsulated (ICG-LPs) with an efficiency of $93.32 \pm 1.25\%$. ICG-LPs were then grafted with iRGD peptide. The mean dynamic diameter of iRGD-ICG-LPs was 115.91 nm. The *in vitro* assays were performed using three different cell lines, HUVECs (high expression of $\alpha_v\beta_3$), 4T1 (high expression of $\alpha_v\beta_3$ and NRP-1), and MCF-7 (low expression of $\alpha_v\beta_3$). After the incubation of these cells with ICG-LPs and iRGD-ICG-LPs, iRGD-ICG-LPs showed 1.86-fold and 1.69-fold higher fluorescence intensity in HUVEC and 4T1 cells, respectively, as compared to ICG-LPs

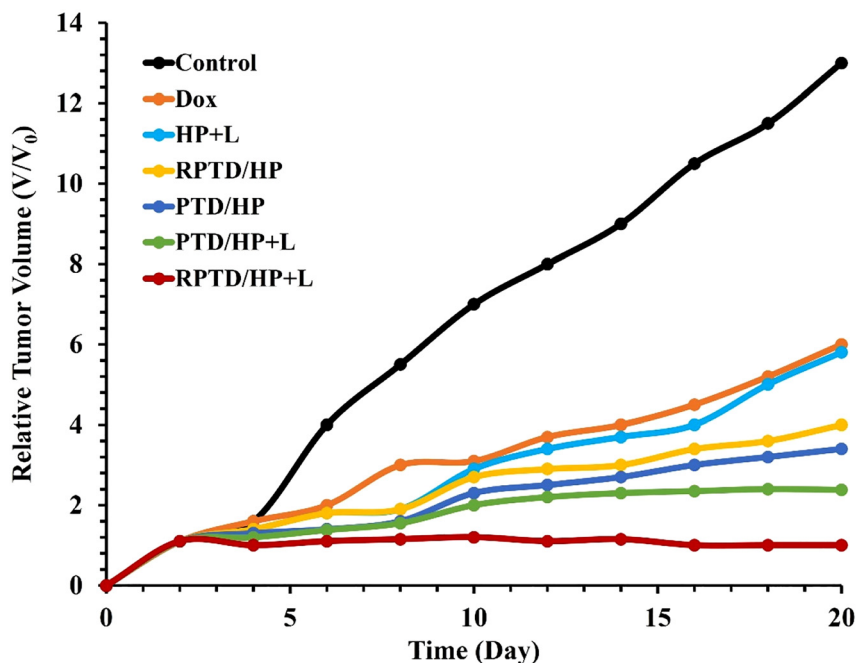


Figure 16: Antitumor effects of Dox, HP + light, nontargeted PTD/HP NPs, nontargeted PTD/HP NPs + light, targeted RPTD/HP NPs, targeted RPTD/HP NPs + light (633 nm, 10 min, 100 mW cm⁻²), with free HP (4.0 μg/mL), PTD/HP, and RPTD/HP nanoparticles (4.0 μg/mL HP and 1.0 μg/mL DOX) and L = Light. Adapted from Shi et al. [43].

(Figure 17(A)). Due to their lower expression of $\alpha_v\beta_3$, MCF-7 cells exhibited an inferior fluorescence as compared to HUVEC and 4T1 cells. The cytotoxicity studies showed that iRGD-ICG-LPs were biocompatible. Under laser illumination, iRGD-ICG-LPs and ICG-LPs exhibited a stronger cytotoxic effect than ICG alone ($P < 0.01$) at the same dose of ICG. The amount of 1O_2 produced without light, but in presence of iRGD-ICG-LPs alone, was 1.91 times smaller than with iRGD-ICG-LPs excited by laser at 480 nm. The coupling of iRGD with ICG-LPs induced a very important PDT-PTT effect, thus demonstrating the specific targeting of the tumors. Using the luminescence of ICG, the *in vivo* results showed a stronger accumulation of the NPs in the tumors than that in the liver, spleen and other organs (Figure 18(A)–(C)). After light illumination of the cells exposed to iRGD-ICG-LPs, the growth of the tumor was suppressed ($P < 0.01$) (Figure 17(B)). For these NPs, the amount of the generated ROS was 3.82 times greater than that produced in the tumors treated with PBS alone (control).

In 2019, Sheng et al. synthesized a novel nanoscale drug [58]. The basis of this NP was the high-density lipoproteins (HDL) in which ICG was encapsulated to give rHDL/ICG. The encapsulation of ICG in NPs presented several advantages such as the stability in the plasma and the lack of precipitation and aggregation. The iRGD peptide was coupled onto this system to afford iRGD-rHDL/ICG. These NPs possessed a hydrodynamic diameter of 90 nm. The *in vitro* assays in 4T1 cells overexpressing $\alpha_v\beta_3$

integrins, and the *in vivo* assays with the 4T1 murine breast cancer model, showed much higher fluorescence intensity for iRGD-rHDL/ICG than that of ICG and rHDL/ICG. This was ascribed to the efficient targeting displayed by iRGD. A strong tumor regression was observed after the treatment with iRGD-rHDL/ICG followed by light illumination at 808 nm (1.8 W cm⁻², 5 min), whereas the tumor continued to grow in the absence of any treatment (Figure 19). The iRGD-rHDL/ICG induced necrotic and apoptotic effects on the tumor tissues due to the ROS generation and, consequently, exhibited a greater photocytotoxicity compared to ICG and rHDL/ICG. In comparison with ICG, iRGD-rHDL/ICG accumulated specifically in tumors, exhibited a higher stability in blood, and showed a slower clearance from the body.

In 2020, Wang et al. developed biodegradable NPs (iMSN/siRNA + miRNA + ICG) [59]. The mesoporous silica NPs (MSN) had a size of 15 nm. ICG was encapsulated in the MSN, with an efficiency of 91%, to afford MSN-ICG. MSN-ICG-iRGD was obtained after the coating of a lipid layer coupled to iRGD peptide on MSN-ICG. Carboxyfluorescein (FAM)-siRNA were adsorbed onto the MSN-ICG-iRGD to improve the targeting and to induce the apoptosis of the cancer cells. After light excitation at 808 nm, ROS were produced, especially 1O_2 . The produced ROS had no significant influence on the genetic silencing activity of RNA, however, the exposure to the irradiation led to undesired heat generation. After irradiation at 808 nm (2.0 W cm⁻² for 5 min), the *in vitro* results in MDA-MB-

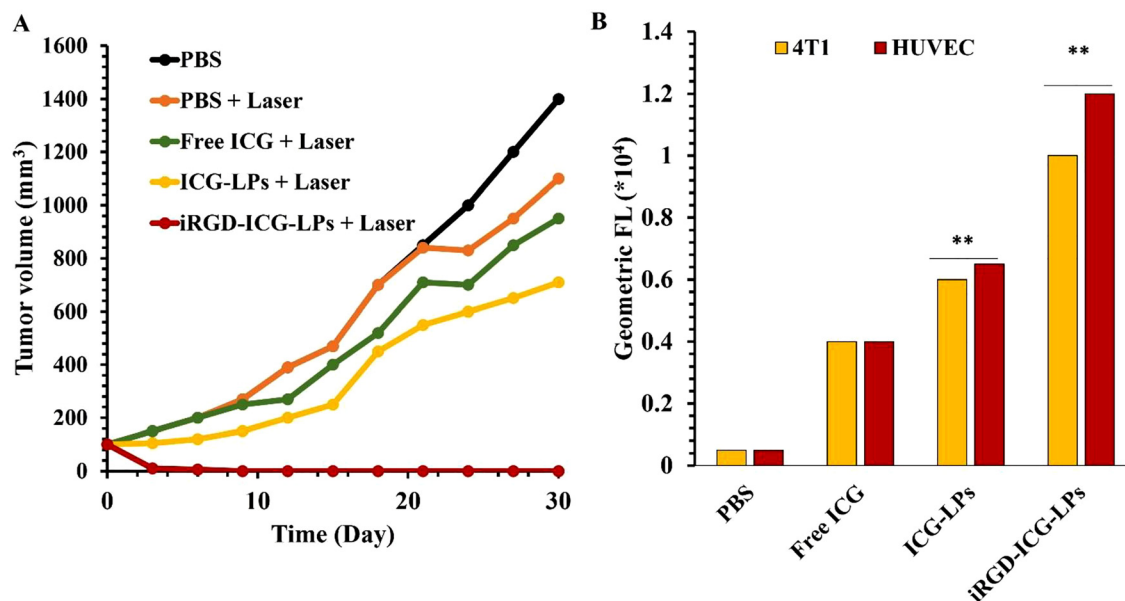


Figure 17: *In vivo* antitumor effect and safety evaluation.

(A) Geometric mean fluorescence intensity of HUVECs and 4T1 cells from flow cytometric analysis, ($n = 3$), (**) $P < 0.01$. (B) Tumor growth curves of nontreated mice or mice receiving iRGD-ICG-LPs, ICG-LPs, free ICG, PBS and laser irradiation within 30 days. (**) $P < 0.01$. An 808 nm laser at a power density of 1.0 W cm^{-2} was used to irradiate these samples for 8 min. Adapted from Yan et al. [45].

231 cells treated with iRGD + MSN/FAM-siRNA + ICG revealed the destruction of the membrane of the endosomal vesicles by the released ROS. iRGD + MSN/FAM-siRNA + ICG induced cancer cell death due to the successful targeting of iRGD and siRNA. *In vivo*, a tumor of MDA-MB-231 cells expressing galectin-8-YFP (Gal8) was grafted in mice. After light illumination at 808 nm, (2.0 W cm^{-2} , 5 min), a significant fluorescence of iRGD + MSN/FAM-siRNA + ICG was observed in the tumor and the liver but not in other organs. The results showed that iRGD + MSN/FAM-siRNA + ICG displayed a strong tumor regression (Figure 20).

2.2.3 NPs@PS@c-RGD

In 2012, Zhou et al. described the synthesis of UCNP (NaYF₄:Yb/Er) coupled to chitosan, cRGD targeting peptide (cyclic RGDyK, named c(RGDK)), and Pyro PS [60]. The diameter of the resulted UCNP-Pyro-cRGD was 53 nm. U87-MG ($\alpha_v\beta_3$ integrin positive (+)) and MCF-7 ($\alpha_v\beta_3$ integrin negative (-)) cells were used for the *in vitro* studies. The targeted UCNP-Pyro-cRGD displayed a high affinity for U87-MG cells. An excess of the free cRGD peptide decreased this affinity, demonstrating the receptor-mediated endocytosis. After light illumination (980 nm, 5 min, 500 mW cm^{-2}), MCF-7 cells treated with UCNP-Pyro-cRGD were intact, while on the contrary, the cell viability of the treated U87-MG cells was drastically decreased (Figure 21).

In 2015, the same team described *in vivo* studies applied in nude mice bearing U87-MG tumors. Two excitation types were chosen; *i.e.* 635 nm or continuous-wave at 980 nm, both at 500 mW cm^{-2} during 60 min with 1 min interval after each minute of irradiation. Two PDT treatments were performed three days apart. In order to mimic the environment of a deep tumor, they used slices of pork to absorb the light. As expected, the highest phototoxicity was achieved when the tumor was treated with UCNP-Pyro-cRGD and NIR-illumination at 980 nm. This result was comparable to that obtained with Pyro and visible-light illumination at 635 nm [61] (Figure 22).

In 2018, Tang et al. focused on the development of NaScF₄: 40% Yb, 2% Er@CaF₂ UCNP. Human serum albumin (HSA) was covalently coupled to the NPs. Ce6 chelating Mn²⁺, for PDT and MRI, was loaded onto the HSA. Finally, the thiolated targeting c(RGDyK) peptide was coupled to the NPs to afford rUCNP@HSA(Ce6-Mn)-cRGD. *In vitro* studies were performed with human glioma U87 and rat glioma C6 cells. To detect ROS, SOSG and dichlorodihydro-fluorescein diacetate (DCFH-DA) were used in solution and in cells, respectively. It was proved that upon excitation, a light resonance energy was transferred from rUCNPs to the Ce6-Mn complex leading to ¹O₂ generation. The highest uptake was observed for the targeted rUCNPs@HSA(Ce6-Mn)-cRGD due to the presence of HSA that could enhance the accumulation through the gp60 receptor and the cRGD peptide that targeted $\alpha_v\beta_3$ integrin.

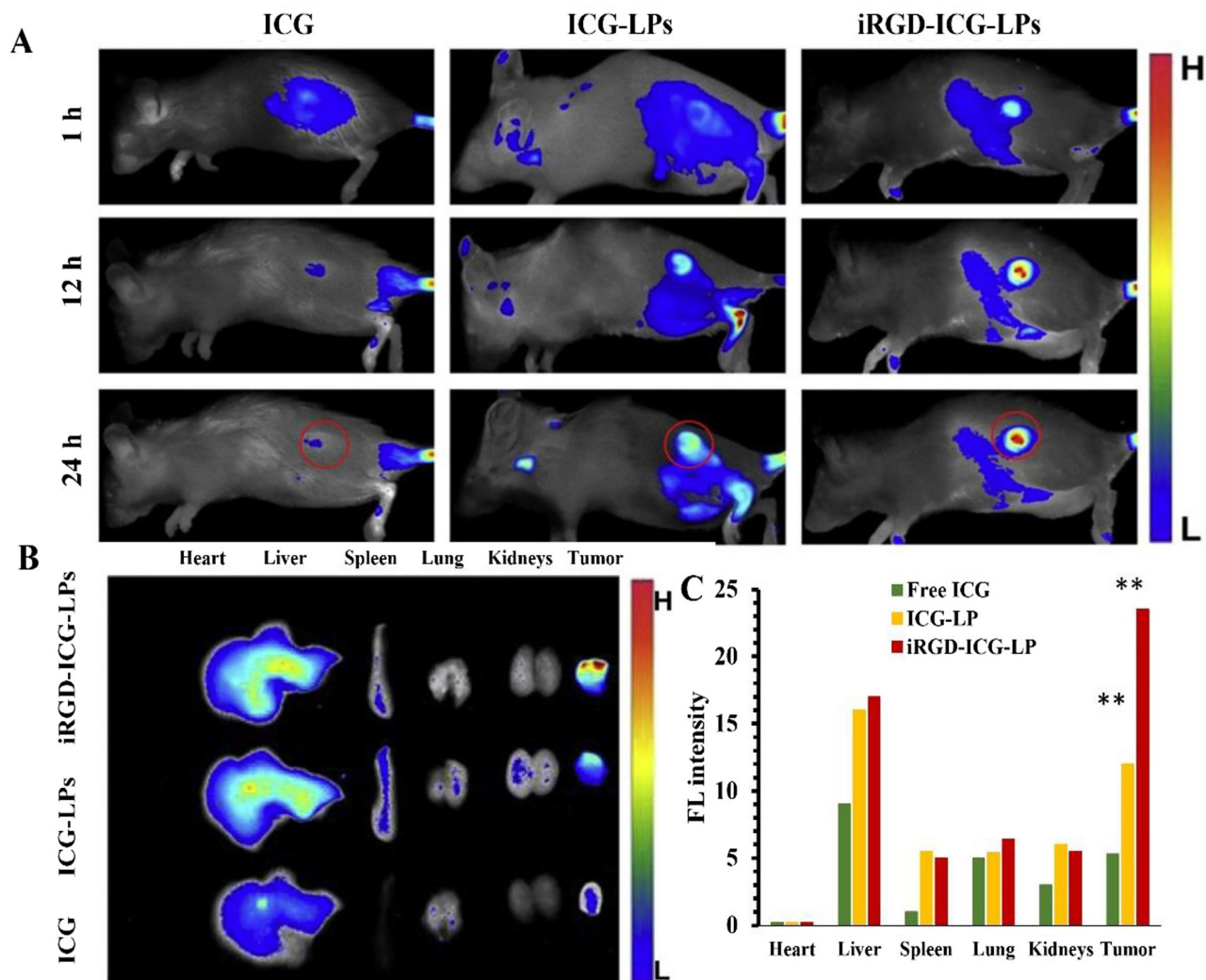


Figure 18: *In vivo* molecular imaging and biodistribution.

The free ICG, ICG-LPs, or iRGD-ICG-LPs were IV administered to the 4T1 tumor-bearing mice and the tumors and major organs were imaged with the *ex/in vivo* imaging system. (A) Fluorescence signal was obtained in tumor sites at 1, 12, and 24 h after IV administration of free ICG, ICG-LPs, or iRGD-ICG-LPs with 0.5 mg/kg equivalent ICG. (B) *Ex vivo* fluorescence images of major organs and tumors were obtained at 24 h post injection of free ICG, ICG-LPs, or iRGD-ICG-LPs with 0.5 mg/kg equivalent ICG. (C) Semiquantitative analysis of fluorescence intensity for the different organs and the tumor showed much higher signal intensity in the tumor of mice received with iRGD-ICG-LPs than those received with free ICG or ICG-LPs. (**) $P < 0.01$. Laser excitation: 808 nm, 1.0 W cm^{-2} for 10 min. Adapted from Yan et al. [45]. With permission from Elsevier and Copyright Clearance Center.

24 h post treatment, the free Ce6 and the non-targeted rUCNPs@HSA(Ce6-Mn) were eliminated from the tumor, whereas the rUCNPs@HSA(Ce6-Mn)-RGD was still there, showing a great targeting and hence a superior retention ability. The cells were illuminated with a 980 nm laser (1.5 W cm^{-2} for 30 min with a 5-min interval between each 5 min illumination) after 6 h of treatment with nontargeted rUCNPs@HSA(Ce6-Mn) or targeted rUCNPs@HSA(Ce6-Mn)-RGD. A strong phototoxic effect was observed with the targeted NPs. *In vivo* experiments were performed in U87 tumor-bearing mice. After 12 h of incubation with the

different compounds, the tumors were illuminated with a 980 nm laser every two days for 14 days (1.5 W cm^{-2} for 30 min with a 5-min interval between each 5 min illumination). The group treated with rUCNPs@HSA(Ce6-Mn)-RGD displayed the lowest tumor growth rate. The median survival times for the mice treated by PBS (control), light only, rUCNPs@HSA(Ce6-Mn) or rUCNPs@HSA(Ce6-Mn)-RGD were 45.0, 51.0, 54.5, and 59.2 days, respectively (Figure 23) [62, 63].

In 2019, Kohle et al. studied the modification of the diagnostic Cornell prime dots (C' dots) by encapsulating

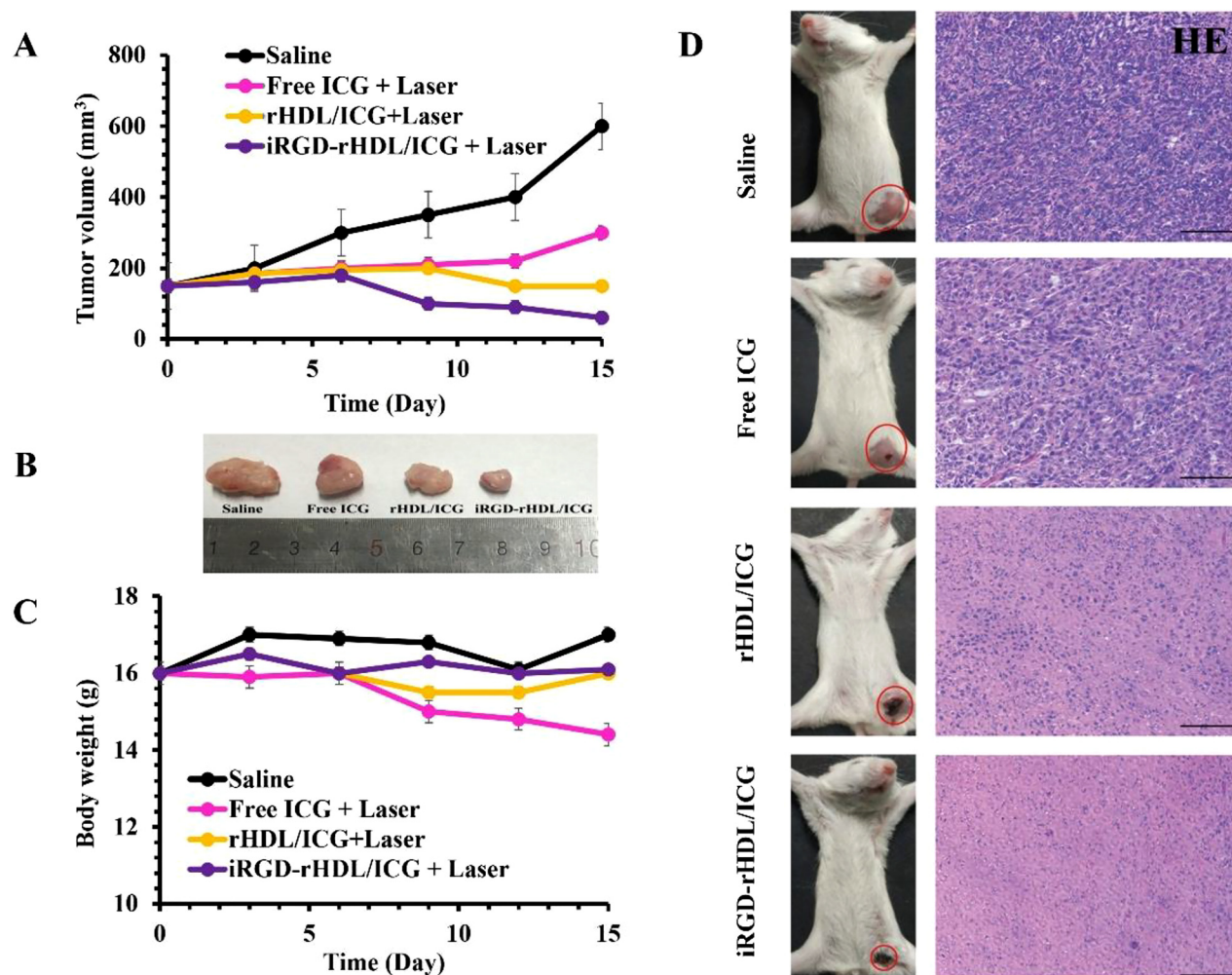


Figure 19: *In vivo* PDT efficacy in 4T1 tumor-bearing mice.

(A) Tumor growth curves after IV-injection of different formulations at an ICG concentration of 1.5 mg kg^{-1} ($n = 5$). (B) Representative image of tumors from the 4T1 tumor-bearing mice sacrificed after being treated with different formulations with 1.5 mg kg^{-1} of ICG1. (C) Changes in body weight over the PDT treatment period. (D) Hematoxylin and eosin (H&E) images of the tumor tissue section after PDT treatment with 1.5 mg kg^{-1} of ICG1. Scale bar is $100 \mu\text{m}$. Data are presented as mean \pm SD, $n = 3$; the light excitation is at 808 nm , 1.8 W cm^{-2} for 5 min. Adapted from Sheng et al. [46]. With permission from Royal Society of Chemistry.

(design 1) or coupling (design 2) a Methylene blue derivative (MB2) PS. In both designs, the functionalization with a c(RGDyC) targeting peptide was performed. The TEM images presented a diameter of about 4.0 nm for each design. They estimated, respectively, 17 and 14 c(RGDyC) units per MB2 molecule for design 1 and 2. The ϕ_0 were determined using the singlet oxygen sensor 1,3-diphenylisobenzofuran (DPBF) and were found to be $111 \pm 3\%$ for design 1 and $161 \pm 5\%$ for design 2. The PS photostability was better in design 1 than in design 2. Surprisingly, the coupling of c(RGDyC) led to a decrease of ϕ_0 by 25 and 12% for design 1 and design 2, respectively. No *in vitro* or *in vivo* studies were performed [64].

In 2005, Kopelman et al. presented a combination of a NP consisting of a polyacrylamide (PAA) core, a cloaking PEG coat, a Photofrin[®] PS, a cRGD targeting peptide (cyclic CDCRGDCFC) and an MRI contrast agent, as shown in Figure 24. The size of PAA NPs was about $30\text{--}60 \text{ nm}$. The $^1\text{O}_2$ production was determined using anthracene-9,10-dipropionic acid disodium salt (ADPA) probe. *In vitro* studies were performed in 9L rat gliosarcoma cells incubated with or without different concentration of NPs. A concentration of 1050 mg mL^{-1} was required to obtain a PDT effect. Rats bearing intracerebral 9L tumors were used for the *in vivo* studies. Diffusion-weighted MR images were obtained from untreated rats and those treated either with

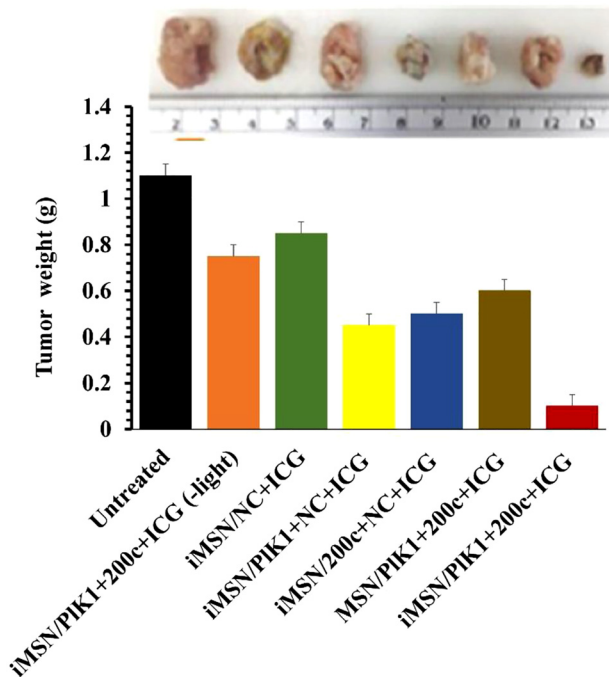


Figure 20: Representative images and weight of the isolated tumors from different groups.

** $P < 0.01$ versus all of the groups, (1) saline, (2) iMSN/NC + ICG, iMSN/Plk1 + 200c + ICG (-light), (3) iMSN/Plk1 + NC + ICG, (4) iMSN/200c + NC + ICG, (5) MSN/Plk1 + 200c + ICG, (6) iMSN/Plk1 + 200c + ICG (+light), and (7) iMSN/Plk1 + 200c + ICG (-light) with 1 mg/kg siPlk1, 1 mg/kg miR-200c and ICG 720 $\mu\text{g}/\text{kg}$. Light excitation: 808 nm, 2 W cm^{-2} , for 5 min. NC is a negative control, siRNA nonspecific to any human gene, Plk1 is a Polo-like kinase 1, 200c is a miR-200c mimic. Adapted from Wang et al. With permission from American Chemical Society.

laser alone or with laser and NPs. Only the latter showed necrosis of the tumor. The final step was the synthesis of targeted NPs using the cRGD peptide and testing them *in vitro* on (+) MDA-435 and (-) MCF-7 cells. The authors observed that targeted NPs bound only to (+) MDA-435 cells [65].

2.2.4 NPs@PS@Fibronectin targeted-peptide

In 2013, Halig et al. formulated iron oxide (IO) NPs encapsulating phthalocyanine 4 (Pc4) PS. These NPs were conjugated to a targeting fibronectin mimetic peptide (Fmp: WQPPRARI), which is well-known to bind to $\alpha_v\beta_3$ integrin overexpressed in head and neck squamous cell carcinoma (HNSCC). Only *in vivo* multispectral imaging was achieved on mice bearing M4E cell induced tumor. These indicated a high accumulation of the nontargeted IO-Pc4 and the targeted Fmp-IO-Pc4 NPs in tumors as

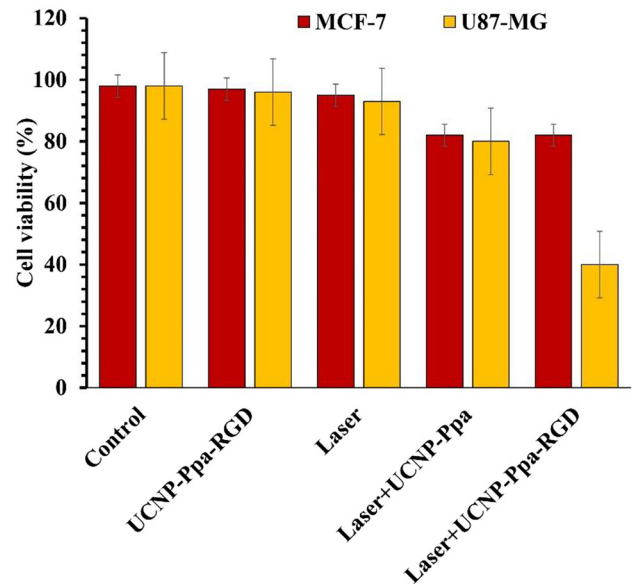


Figure 21: PDT effect on (-) MCF-7 and (+) U87-MG cells treated with different concentration of 0, 50, 100, 200 $\mu\text{g}/\text{mL}$ NPs (980 nm, 500 mW cm^{-2} for 5 min). Adapted from Zhou et al. [47].

compared to Pc4 alone. No clear effect of Fmp was observed [66].

In 2014, the same team estimated the size of the targeted Fmp-IO-Pc4 NPs of about 41 nm. *In vitro* experiments were carried out on 4 HNSCC cell lines (M4E-15, TU212, 686LN, M4E CNT). The most significant tumor regression was observed 48 h after laser treatment at 672 nm (100 mW cm^{-2} , 30 min) for the cells exposed to Fmp-IO-Pc4 NPs as compared to free Pc4, IO-Pc4 NPs, and IO NPs. *In vivo* experiments were then carried out on HNSCC xenografted mice. The initial tumor size in the mice was 5–7 mm^3 before the administration of the targeted and nontargeted NPs and the laser irradiation. 48 h post-administration, the results showed that both NPs prompted a reduced tumor growth compared to free Pc4, but still led to a final increase in tumor volume compared to the initial volume (Figure 25) [67].

In 2020, Y. Wang et al. described the synthesis and characterization of Pep-SQ@USPIO nanoprobe used for imaging-guided PDT of triple negative breast cancer (TNBC) [58]. This new cathepsin B (CTSB)-activatable nanoprobe was designed to achieve both fibronectin-targeting magnetic resonance (MR) imaging and near infrared fluorescence (NIRF) imaging. SQ (squaraine-based) PS, known for its high NIR emission and photodynamic effect, was firstly synthesized. The PS was further conjugated with fibronectin-targeting peptide (CREKA) by means of the CTSB-cleavable peptide (GFLG) to form the

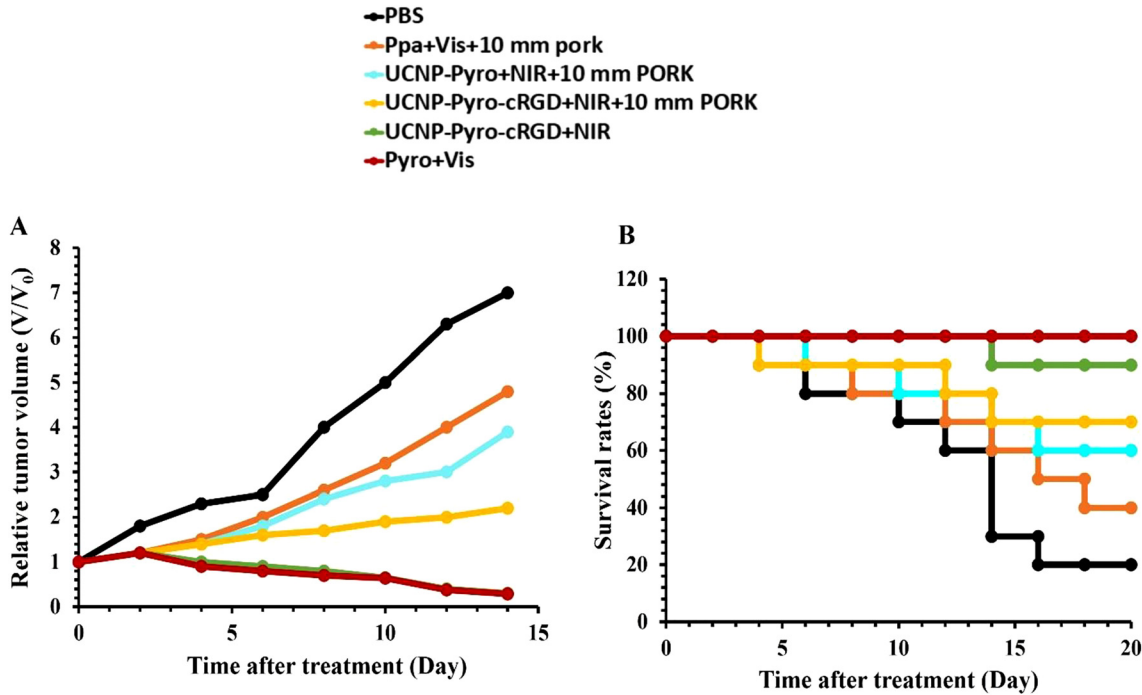


Figure 22: *In vivo* PDT treatment with same concentration of pyro (10 μ M). (A) time-dependent tumor growth rate, 14 days after the PDT treatment (B) mice survival rate after different kinds of PDT treatment with light excitation at 635 nm for Vis and 980 nm for NIR (500 $mW\ cm^{-2}$) for 1 min. Adapted from Zhou et al. [48].

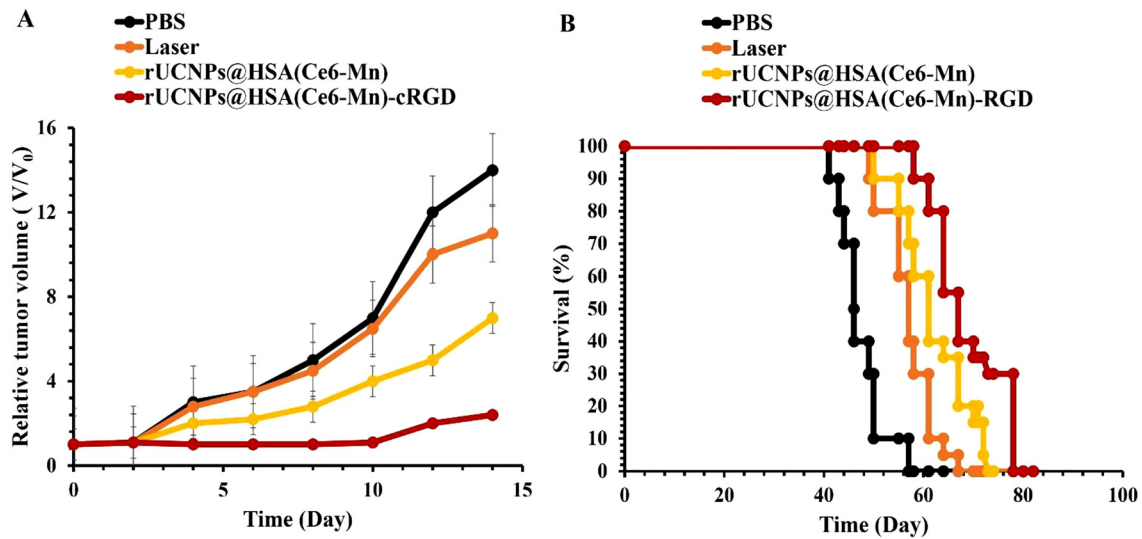


Figure 23: (A) The relative tumor volume after treatment with PBS (control), light only, rUCNPs@HSA(Ce6-Mn) or rUCNsP@HSA(Ce6-Mn)-RGD, with a concentration of 5.2 mg/kg (Ce6 equivalent) and (B) Kaplan–Meier survival time curve. Light excitation at 980 nm (1.5 $W\ cm^{-2}$) for 5 min. Adapted from Tang et al. [49, 50].

Pep-SQ conjugate. The Pep-SQ@USPIO nanoprobe was finally obtained by the covalent coupling of the Pep-SQ conjugate onto the maleimide-DSPE-PEG2000-coated ultrasmall superparamagnetic iron oxide (USPIO) NPs.

The hydrodynamic diameter of the NPs was 20 nm, as measured by DLS. *In vitro* PDT testing of the Pep-SQ@USPIO was done on MDA-MB-231 cells overexpressing fibronectin. After 24 h of cell incubation with Pep-

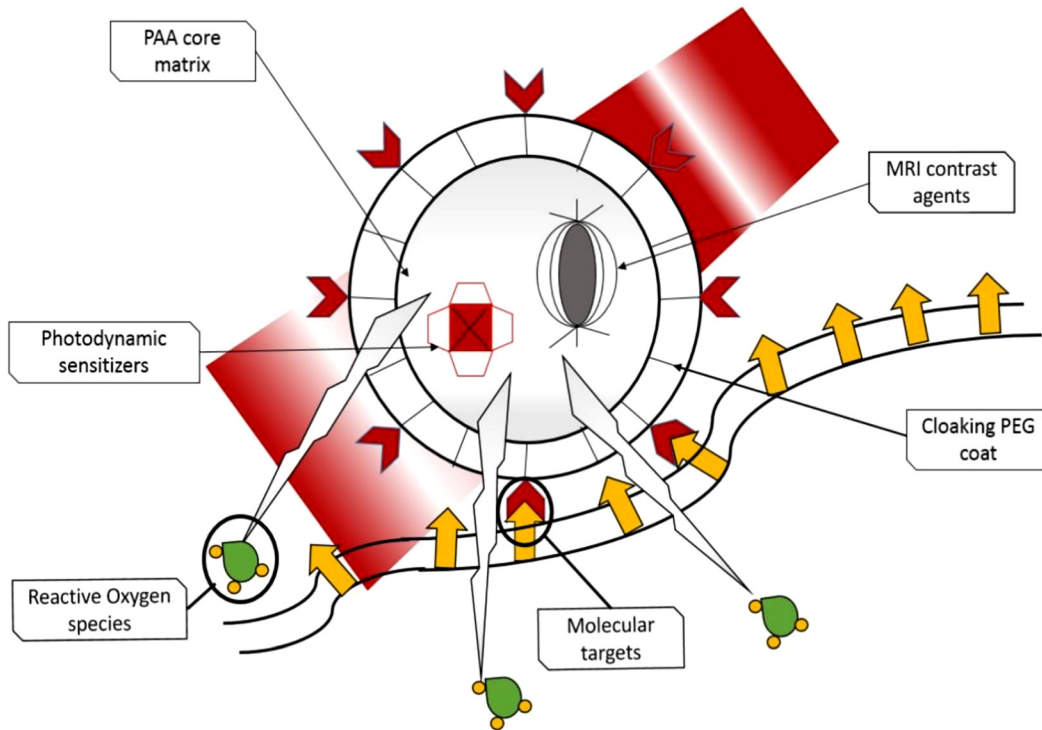


Figure 24: The schematic nanoplateform consisting of PAA core matrix with PEG cloaking coat, photodynamic dye (Photofrin[®]), MRI contrast enhancement agents and molecular targeting (cRGD peptide). Adapted from Kopelman et al. [52].

SQ@USPIO, the irradiation was applied (5 min, 660 nm, 1 W cm^{-2}). A significant decrease in the cell viabilities was induced by the increase of the laser power densities at 660 nm. In addition, cells treated with various concentrations of pep-SQ@USPIO, ranging between 100 and $800 \mu\text{g mL}^{-1}$, showed different degrees of apoptosis, consequently verifying the PDT efficiency of this system. The assessment of the accumulation of these NPs by Prussian blue staining revealed a low amount of iron in the heart, lungs, and kidneys, thus demonstrating the absence of pep-SQ@USPIO accumulation. However, the evident Prussian blue staining that occurred in both liver and spleen can arise from both nanoprobe accumulation and the endogenous iron. The obtained results of the NIRF imaging proved that the sufficiently high CTSB activity in the TNBC tumors enabled its detection by Pep-SQ@USPIO. The photodynamic efficiency of Pep-SQ@USPIO was also tested *in vivo* on MDA-MB-231 tumor-bearing mice. The tumor volume and mass decreased sharply when treated with Pep-SQ@USPIO in the presence of Laser irradiation (660 nm , 2 W cm^{-2}) as compared to those exposed to Pep-SQ@USPIO alone, control (PBS), and laser alone (PBS + L). Therefore, it was validated that the Pep-SQ@USPIO

activated nanoprobe exhibited a high photodynamic efficiency under laser irradiation, which allows for an enhanced PDT guided by NIRF/MR bimodal imaging for the treatment of TNBC.

In 2021, H. Cao et al. described the elaboration of BKC-NPs (6 nm) formed by the self-assembly of the multifunctional peptide BP-FFVLK-CREKA (BKC) in water. The NPs were constituted of three motifs; hydrophobic BP (bis(pyrene)) PS used for imaging and ROS production, FFVLK peptide for stabilizing the structure, and CREKA peptide for fibrin-targeting on the extracellular matrix of tumors and new-born blood vessels [59]. Using ABDA ((9,10-anthracenediyl-bis(methylene)dimalonic acid)) as ROS detection reagent, the authors observed the formation of singlet oxygen after the two-photon excitation of the BKC-NPs at 800 nm. The *in vitro* experiments were performed on MCF-7 and HUVECs that express fibrous protein onto their surfaces. No specificity was observed for MCF-7. Whereas, the robust interaction between BKC-NPs and the HUVECs was established by the strong fluorescence that was detected both inside and at the surface of these cells. This interaction was attributed to the abundant expression of fibrous protein onto the surface of HUVECs which

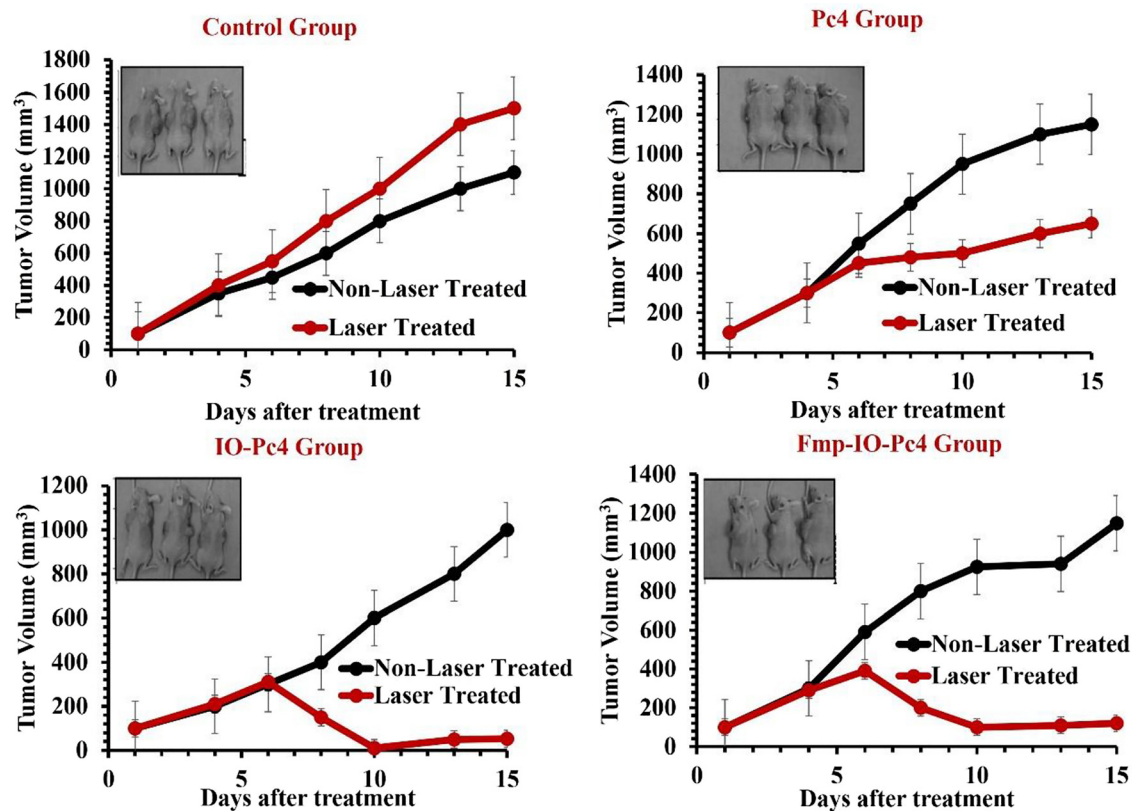


Figure 25: Inhibition of xenograft tumor formation by Pc4 PDT treatment delivered by IO NPs. (A–D) Tumor growth and representative images of tumors on both sides of the mice in (A) PBS control, (B) free Pc4, (C) IO-Pc4, and (D) Fmp-IO-Pc4 groups, respectively with 0.4 mg/kg Pc4. Laser treatment was performed at 48 h post administration (672 nm, 100 mW/cm² for 30 min). Three out of six mice from each group are shown as representatives.

Adapted from Halig et al. [54]. With permission from American Chemical Society.

allowed for a more specific recognition by the CREKA motif in the NPs. Cells incubated with the same concentration of BKC-NPs were tested under different conditions. After exposure to light illumination at 800 nm, the cell viability attained 20.8%, whereas it reached 16% for one photon (405 nm) and 73% for the control (two-photon laser of 800 nm (1 W) or a xenon lamp with a 405 nm cut-off filter for 20 min). *In vivo* experiments were then performed using BKC-NPs in BALB/c mice imaging. Confocal laser scanning microscopy revealed blood vessels in the ear and in the tumor. To explore the precision of the therapy *in vivo*, a selected region was illuminated by a two-photon laser for about 2 min. It was observed that the ROS generated by the accumulated BKC-NPs caused quick vessel breaking as compared to the control vessel that remained intact. It was proven that these new NPs could be used in precise surgery in the brain and eyes for example. Concerning PDT experiments, the mice were injected with these NPs and were illuminated with a two-photon laser at 800 nm at different time intervals. At day 16, it was observed that the tumor

volumes increased to attain 695.8, 780.2, and 610.3 mm³ for the control, laser, and BKC-NPs alone, respectively. However, an important tumor volume regression, reaching 67 mm³, was achieved by the BKC-NPs in the presence of irradiation.

2.2.5 NPs@PS@RGD-4R

In 2019, Dai et al. described the elaboration of polymeric NPs consisting of 1,2-distearoyl-sn-glycero-3-phosphoethanolamine-N-[maleimide(polyethylene glycol)-2000] (MPD) matrix encapsulating a fluorogen (TTB). TTB displays an important aggregation-induced emission with strong NIR fluorescence and can efficiently produce ROS especially ¹O₂. These MPD/TTB NPs were covalently coupled, *via* click reaction, to a targeting peptide, either RGD or RGD-4R (*i.e.* modular peptide RGDFGGRRRRRC), to produce targeted RGD-MPD/TTB and RGD-4R-MPD/TTB NPs. ROS production was demonstrated using dichlorofluorescein (DCFH), dihydrorhodamine 123 (DHR123), and

EPR spectroscopy to identify $O_2^{\bullet-}$ and ABPA to detect 1O_2 . The targeted NPs presented a high NIR luminescence at 730 nm and were efficient for real-time fluorescence monitoring. SKOV-3, HeLa, and PC3 cell lines having high $\alpha_v\beta_3$ integrin expression and MCF-7 cell line with low $\alpha_v\beta_3$ integrin expression were used to prove the specificity of RGD-targeted NPs to $\alpha_v\beta_3$ integrins. The incorporation of the targeted NPs in MCF-7 was negligible, while it was significant in the other cell lines. The targeted RGD-4R peptide presented a higher affinity than RGD. The PDT performed on cells incorporated with targeted RGD-4R-MPD/TTB NPs (730 nm, 200 mW cm⁻², 10 min) revealed an apoptotic rate of 87% for PC3, 89% for HeLa, and 91% for SKOV-3 cells. In comparison, it was only 17% for MCF-7 cells. The xenografted tumor model with HeLa, PC3 and SKOV-3 cells were used for the *in vivo* studies. A remarkable tumor growth delay was observed after the injection of targeted RGD-4R-MPD/TTB NPs and illumination at 730 nm (200 mW cm⁻², 10 min) (Figure 26). This was accompanied with an inhibition of the expression of BCL2 and *Ki-67* genes, and hence led to a reduction in the tumor proliferation and an advancement of apoptosis [68].

2.2.6 NPs@PS@RGDFK

In 2014, Haedicke et al. developed calcium phosphonate NPs, in which they incorporated 5,10,15,20-Tetrakis (3-hydroxyphenyl)chlorin (*m*THPC) PS. The authors covalently coupled both a targeted RGD peptide (RGDFK) and a fluorescent dye (DY682) for near-infrared fluorescence (NIRF) emission. *In vitro* experiments were performed using tongue-squamous epithelium carcinoma cells CAL-27. A perinuclear localization of the NPs was observed. *In vivo* experiments were conducted in CAL-27 xenografted female athymic nude mice. The best accumulation for the non-targeted and the RGD targeted NPs was found at 8 and 24 h post-treatment, respectively. A better internalization in the tumor was observed using RGD targeted NPs in comparison to the non-targeted NPs or Foslip[®] PS. However, a strong accumulation was also detected in the lungs, kidneys, spleen, and liver. After PDT (652 nm, 0.1 W cm⁻², 100 J cm⁻²), a decrease of both tumor volume and tumor vascularization was demonstrated in 3 out of 4 animals [69].

Table 2 describes the NPs@PS@peptide systems, targeting $\alpha_v\beta_3$ integrin, regarding the types of NPs, PSs and

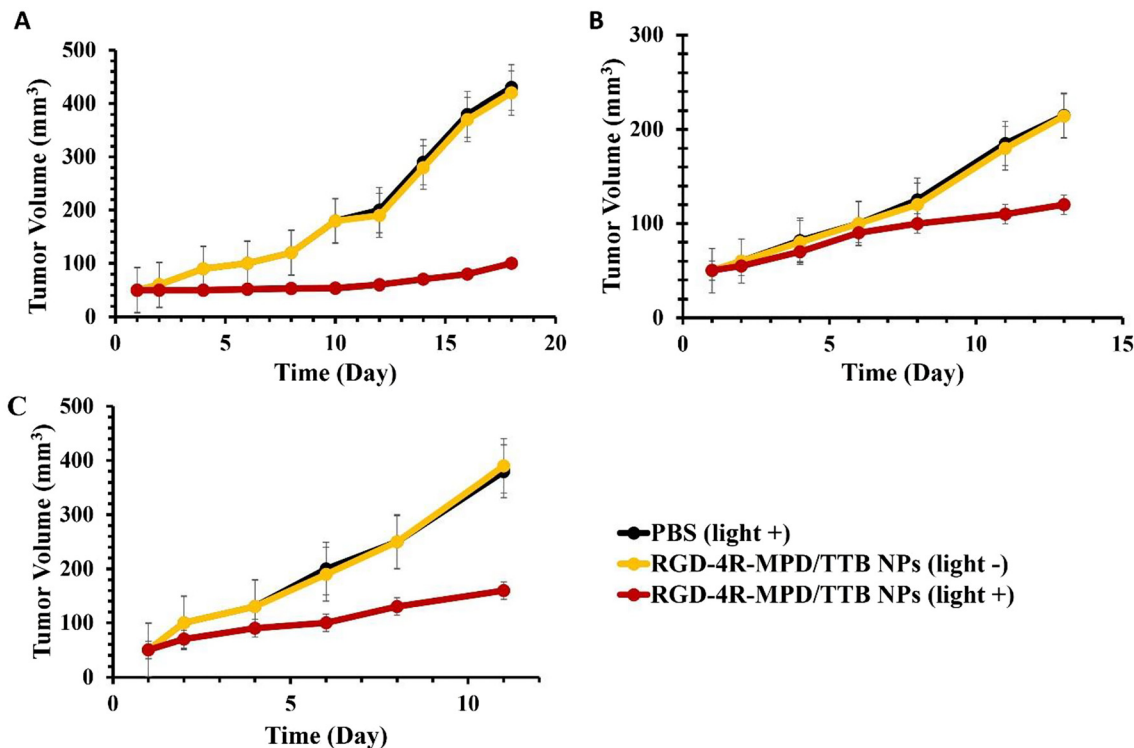


Figure 26: RGD-4R-MPD/TTB (10 μ g/mL) NPs mediated PDT for multiple xenograft tumors.

Tumor volume changes in (A) HeLa, (B) PC3, and (C) SKOV-3 cells. Light excitation at 730 nm, 200 mW cm⁻² for 10 min. Adapted from Dai et al. [55].

the coupling between them, in addition to the NPs size, excitation wavelength ($\lambda_{\text{excitation}}$), fluorescence quantum yield (ϕ_F), singlet oxygen quantum yield (Δ_{O_2}) and the results obtained *in vitro* and/or *in vivo*.

2.3 Peptide for nucleolin membrane receptors

Nucleolin is a nucleolar protein that has several roles in the intracellular pathways and is involved in tumorigenesis [72]. It is expressed in the nucleus of resting cells. In tumor cells, nucleolin cycles between the cell nucleus and the plasma membrane. Its overexpression was identified in different kind of cancers. Therefore, nucleolin is considered a target for anticancer therapies [73].

F3 peptide has a sequence of KDEPQRRSARLSAK-PAPPKPEPKPKKAPAKK. It is well-known to target tumor neovessels as well as some tumor cells [74, 75]. F3 peptide can bind to the nucleolin membrane receptors, which allows its internalization into the cells and its further localization into the nucleolin.

Kopelman's team reported the elaboration of an F3-targeted nanosystem, consisting of a polyacrylamide core in which a photodynamic agent, Photofrin[®] PS, and an MRI agent, iron oxide, were embedded. The F3 targeting peptide was also attached to the NPs in addition to the coupling to Alexa Fluor 594 for fluorescent imaging. Six molecules of Photofrin[®] were encapsulated into each NP and average of 30 F3 peptides were coupled. No cytotoxicity was observed in MDA-435 cells after 4 h of incubation with the F3-targeted NPs. However, a significant phototoxic effect was achieved after light illumination (630 nm, 1.5 mW, 5 min) as 90 % of the cells were destroyed. Using fluorescence microscopy, the authors detected a cellular uptake and a nuclear localization of F3-targeted NPs. *In vivo* studies in rats bearing 9L gliomas were performed in the presence of nontargeted and F3-targeted NPs for comparative reasons. The F3-targeted NPs had about three-fold prolonged tumor transit time. Their presence led also to an improved contrast-to-noise ratio of about two-fold at 1 h. A median survival time after treatment and illumination was found to be 7.0 days for the control untreated group, 8.5 days for the group treated only with laser and 13.0 days for the one treated with Photofrin[®] alone. Conversely, the median survival time was up to 33 days for the group treated with F3-targeted NPs (Figure 27) [76].

The same team [77] reported polyacrylamide NPs conjugated with MB PS and F3 targeting peptide. First, MB

was coupled to the 3-aminopropylmethacrylamide hydrochloride (APMA) monomer before the formation of NPs in a reverse microemulsion. The amino functions of APMA were then used to couple the F3 peptide. Four cell lines were cultivated, human melanoma MDA-MB-435, rat glioma F98, human breast adenocarcinoma MCF-7 and rat glioma 9L. The nucleolin expression was described previously by the same team [78]. The F3-targeted NPs presented the lowest affinity for MCF-7 cells. Yet, a better affinity by 2.5, 4, and 5.4 times was achieved for F98, MDA-MB-435 and 9L cells, respectively. No incorporation of the non-targeted MB-conjugated NPs was observed. Comparable results in terms of the photodynamic efficiency were obtained on all the four cell lines when the targeted NPs were tested at 1.5 mg mL⁻¹ and illuminated at 647 nm (20 J cm⁻², 1 min). Further experiments performed on F98 cell lines proved that the cell death increased with illumination time and NPs concentration.

Feng et al. described the synthesis of targeted F3-PTX-(Pyro-PLA)₂PEG NPs (denoted by F3-targeted NPs). These consist of pyro-conjugated amphiphilic (Pyro-PLA)₂PEG NPs covalently attached to the F3 targeting peptide. Paclitaxel (PTX, Taxol) was then encapsulated to demonstrate a combination of PDT and chemotherapy [79]. (Pyro-PLA)₂PEG NPs presented a good stability *in vitro*. In HUVEC and human colorectal cancer cells (HCT-15), a better accumulation of the F3-targeted NPs was observed with a factor of 1.21 and 1.18, respectively, when compared with that of (Pyro-PLA)₂PEG. These NPs were localized mostly in the endolysosomal compartment. The production of ROS was demonstrated using 2',7'-dichlorofluorescein (DCF) fluorescence. The IC₅₀ values in HUVEC were 122.1 ng mL⁻¹ for Taxol, 84.09 ng mL⁻¹ for non-targeted NPs (*i.e.* PTX-(Pyro-PLA)₂PEG NPs) in the absence of laser, 41.21 ng mL⁻¹ for non-targeted NPs in the presence of laser and 17.0 ng mL⁻¹ for F3-targeted NPs accompanied by laser irradiation. The IC₅₀ values in HCT-15 cells were 426.7 ng mL⁻¹ for nontargeted NPs in the absence of laser, 86.32 ng mL⁻¹ for non-targeted NPs in the presence of laser and 32.86 ng mL⁻¹ for F3-targeted NPs accompanied by laser irradiation. These outcomes validated the importance of adding a targeting peptide to boost the PDT efficiency. The *in vivo* experiments performed in male BALB/c nude mice bearing colorectal tumor (HCT-15 injected subcutaneously) confirmed the *in vitro* results. After injection, the nontargeted NPs were slightly accumulated in the tumor and around the blood vessels, whereas the F3-targeted NPs were effectively accumulated into the tumor due to the efficient targeting of both the tumor cells and the

Table 2: The summary of NPs conjugated with PSs and peptides targeting $\alpha_v\beta_3$ integrin in terms of different parameters.

Reference	NPs	PS	NPs@PS@Peptide targeting $\alpha_v\beta_3$					$\Delta_{0.5}$	<i>in vitro</i>	<i>in vivo</i>
			Coupling between NPs and PS	NPs size (nm)	$\lambda_{excitation}$ (nm)	ϕ_F				
Peptide RGD										
[52]	Polymeric (PEG)	IR700	Maleimide	6.6 for RGD-8PEG-IR700	540	nd	nd	A375	Mouse fibroblast NIH/3T3	
[50]	Mesoporous silica (MSN)	Photoporphyrin IX (PpIX)	Amide bond	50 for MSN-BHQ-SS-PpIX-PEG-RGD	nd	nd	nd	COS7 SCC-7 HeLa Hela	nd	
[51]	Upconversion (UCN)	Zinc (II) phthalocyanine (ZnPc)	Encapsulation	150 for ZnPc-UCN@lipid@PS	980	nd	nd	HeLa Hela	nd	
[49]	Upconversion (UCN)	Merocyanine 540 (MC540)	Adsorption	225 for MC540 loaded UCN/RGD-PMAO-DOPE	540	nd	nd	MCF-7	nd	
Peptide iRGD										
[58]	High-density lipo-proteins (HDL)	Indocyanine green (ICG)	Encapsulation	86.7 for iRGD-rHDL/ICG	808	nd	nd	4T1	Female BALB/c mice	
[59]	Mesoporous silica (MSN)	Indocyanine green (ICG)	Encapsulation	100-200 for Amine-functionalized MSNs	808	nd	nd	MDA-MB-231.Luc B16F10.Luc. 4T1	Immuno compromised female NCG mice 4T1 Tumor-bearing mice	
[57]	Liposome (LP)	Indocyanine green (ICG)	Encapsulation	115.91 for iRGD-ICG-LPs	808	nd	nd			
Peptide cRGD										
[54]	Globular PEG	Chlorin e6 (Ce6)	Maleimide	3-4 for cRGD-gPEG-Ce6	360	nd	nd	SKOV-3 KB	Seven-week-old Female nude mice (BALB/c nu/nu mice, Institute of Medical Science, Tokyo)	
[53]	Poly (amido amine) dendrimer (PAMAM)	Chlorin e6 (Ce6)	Amide bond	28 for PEG-P-Ce6 and 273 RGD-P-Ce6	488	nd	2.5-fold higher than that of free Ce6	A375 NIH3T3	nd	
[55]	Self assembly	Hematoporphyrin (HP)		180 for RPTD/HP	395	nd	nd	nd	nd	

Table 2: (continued)

NPs@PS@Peptide targeting $\alpha_5\beta_3$									
Reference	NPs	PS	Coupling between NPs and PS	NPs size (nm)	$\lambda_{excitation}$ (nm)	ϕ_F	$\Delta_{0.5}$	<i>in vitro</i>	<i>in vivo</i>
Thioketal linkage									
Peptide c(RGDyK)									
[60]	Upconversion (UCN)	Pyropheophorbide-a (Pyro)	Amide bond	53 for OCMC-UCNP	414	nd	nd	U87-MG MCF-7	nd
[64]	Silica	Methylene blue (MB)	Encapsulation (Design 1), Mal-eimide (Design 2)	Below 10 for designed NPs 1 and 2	543	nd	$111 \pm 3\%$ for Design 1 $161 \pm 5\%$ for Design 2	nd	nd
[61]	Upconversion (UCN)	Pyropheophorbide-a (Pyro)	Amide bond	55 for UCNP-Pyro-RGD	633	nd	nd	U87-MG	Nude mice bearing U87-MG tumor
[63]	Upconversion (UCN)	Chlorin e6 Mn ²⁺ (Ce6-Mn)	Encapsulation	101.6 for UCNPs@HSA	980	nd	nd	U87	U87-Bearing mice
Peptide cRGD									
[65]	Polyacrylamide (PAA)	Photofrin [®]	Encapsulation	30–60 for PAA	630	nd	nd	9L rat	Rats bearing intracerebral 9L tumors
Peptide Fmp fibronectin									
[66]	Iron oxide	Phthalocyanine 4 (Pc4)	Encapsulation	nd	586–820	nd	nd	nd	Mice bearing M4E tumor induced
[67]	Iron oxide	Phthalocyanine 4 (Pc4)	Encapsulation	41 for Fmp-10-Pc4	672	nd	nd	M4E, M4E-15, 686 LN, TU212	Mice bearing M4E tumor induced
Peptide RGD or RGD-4R									
[68]	Polymeric matrix	TTB ^a	Encapsulation	79.1 for RGD-4R-MPD/TTB	400–700	0.10 in solid state	nd	MCF7, PC3, HeLa, SKOV-3	BALB/c Nude mice (male for PC3 xenograft tumor and female for both HeLa and SKOV-3 xenografted tumor models)

Table 2: (continued)

Reference	NPs	PS	NPs@PS@Peptide targeting $\alpha_v\beta_3$				$\Delta_{0.5}$	ϕ_F	<i>in vitro</i>	<i>in vivo</i>
			Coupling between NPs and PS	NPs size (nm)	$\lambda_{excitation}$ (nm)					
			Peptide RGDfK							
[69]	Calcium phosphate	5,10,15,20-Tetrakis(3-hydroxyphenyl)chlorin (mTHPC)	Encapsulation	205 for NP-DY682-mTHPC-RGD	652	nd	nd	CAL-27	Female athymic nude mice	
			Peptide CREKA							
[70]	Self assemble of bis(pyrene)-FFVLK	bis(pyrene)	Amide bond	6	405 nm (one photon) and 800 nm (two-photon, day 1 and 4; 7 min (3.5 W cm ⁻²), day 8; 8 min with 4 W cm ⁻² laser)	nd	60.1%	MCF-7 and HUVEC	BALB/C mice	
[71]	Ultrasmall Superparamagnetic iron oxide	SQ (Squaraine)	amide bond	20	660	nd	nd	MDA-MB-231	MDA-MB-231 tumor-bearing mice	

^a TTb: Contains an electron-accepting benzo[1,2-b:4,5-b']dithiophene 1,1,5,5-tetraoxide core and electron-donating 4,4'-(2,2-diphenylethene-1,1-diyl)bis(N,N-diphenylaniline) groups for image-guided targeted PDT, *nd, not determined.

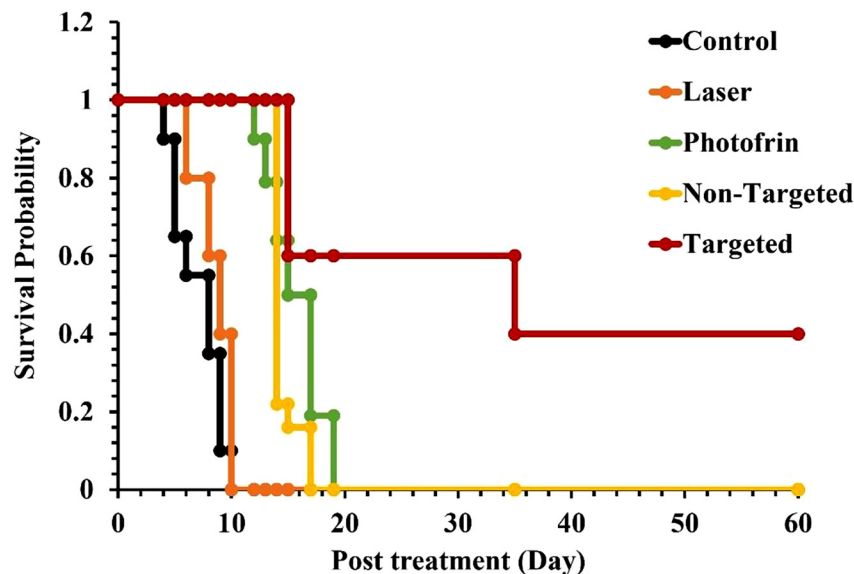


Figure 27: Survival curves for animals bearing a brain tumor: untreated (control), laser only, Photofrin[®] + laser, nontargeted NPs + laser and F3-targeted NPs + laser with a concentration of 7 mg Kg⁻¹ (Photofrin equivalent). Irradiation at 630 nm, 1.5 mW for 5 min. Adapted from Kopelman et al. [61].

neovessels. After light irradiation (660 nm, 100 J cm⁻² for 9.8 min), the inhibition rate of the tumor was 79.92% for the F3-targeted NPs. F3-PTX-(Pyro-PLA)₂PEG NPs showed better results of tumor regression (Figure 28(A) and (C)) and had a better survival rate in mice as compared to these NPs without laser or nonvectorized NPs (Figure 28(B)). However, the tumor inhibition rate was only 5.71% for Taxol, 18.97% for nontargeted NPs without irradiation, 38.08% for PTX-free nontargeted NPs (*i.e.* (Pyro-PLA)₂PEG NPs) in the presence of laser irradiation and 54.68% for nontargeted NPs without laser (Figure 28(D)). The combination of PDT and chemotherapy was more efficient than any of these treatments alone. The addition of the F3 peptide allowed the NPs to accumulate specifically into the tumor parenchyma as well as around tumor angiogenesis [79].

Table 3 describes the NPs@PS@peptide systems, targeting $\alpha_v\beta_3$ integrin, regarding the types of NPs, PSs, and the coupling between them, in addition to the NPs size, excitation wavelength ($\lambda_{excitation}$), fluorescence quantum yield (ϕ_F), singlet oxygen quantum yield ($\Delta_{O,S}$) and the results obtained *in vitro* and/or *in vivo*.

2.4 Peptides for cell penetration

The plasma membranes form barriers, with a selective permeability that hinder the intracellular transfer of the anticancer drugs. To overcome this obstacle, cell penetrating peptides of 5–30 amino acids can be used [80]. TAT (GRKKRRQRRRPQ) is a 12-amino acid peptide that allows the penetration into the cells [81]. Direct penetration has

been proposed as the mechanism used for the internalization of the TAT protein. The first step in this model is the interaction between the membrane and the unfolded TAT fusion protein that causes the disruption of the membrane enough to allow its passage. Once internalized, the TAT fusion protein will then fold back using of a chaperone system. There is no consensus on this mechanism, and other ones that have been proposed involve clathrin-mediated endocytosis.

In 2013, Fales et al. synthesized Raman-labeled gold nanostars (AuNS-DTDC), where DTDC, 3,3'-diethylthiadicarbocyanine iodide, represents the Raman probe. The NPs were coated with a silica shell and loaded with PpIX PS and TAT peptide, where the latter was conjugated by passive adsorption, to afford AuNS-DTDC@SiO₂-PpIX-TAT. The size of NPs was 123 nm. The *in vitro* Raman imaging of BT-549 breast cancer cells incubated for 24 h with AuNP-DTDC@SiO₂-PpIX without TAT displayed little to no signal, in contrast to that obtained in the presence of TAT. Such results indicated the convenience of this method in the delivery of the NPs into the cells. An *in vitro* phototoxic effect was observed after the excitation with a mercury arc lamp (filtered at 633 nm, 4.4 W cm⁻², 30 s), in BT-549 breast cancer cells exposed to the NPs (Figure 29). The PDT effect induced by the developed NPs was clearly validated in the fluorescent microscopic images of the BT-549 breast cancer cells, incubated with the NPs with and without PpIX (Figure 29) [82].

In 2014, Thandu et al. developed superparamagnetic iron oxide (SPION) NPs coupled to 5-(4-carboxyphenyl)-10,15,20 triphenyl-porphyrin (TPP) PS. The size of the SPION NPs alone was 20 nm. The coupling of TPP to SPION

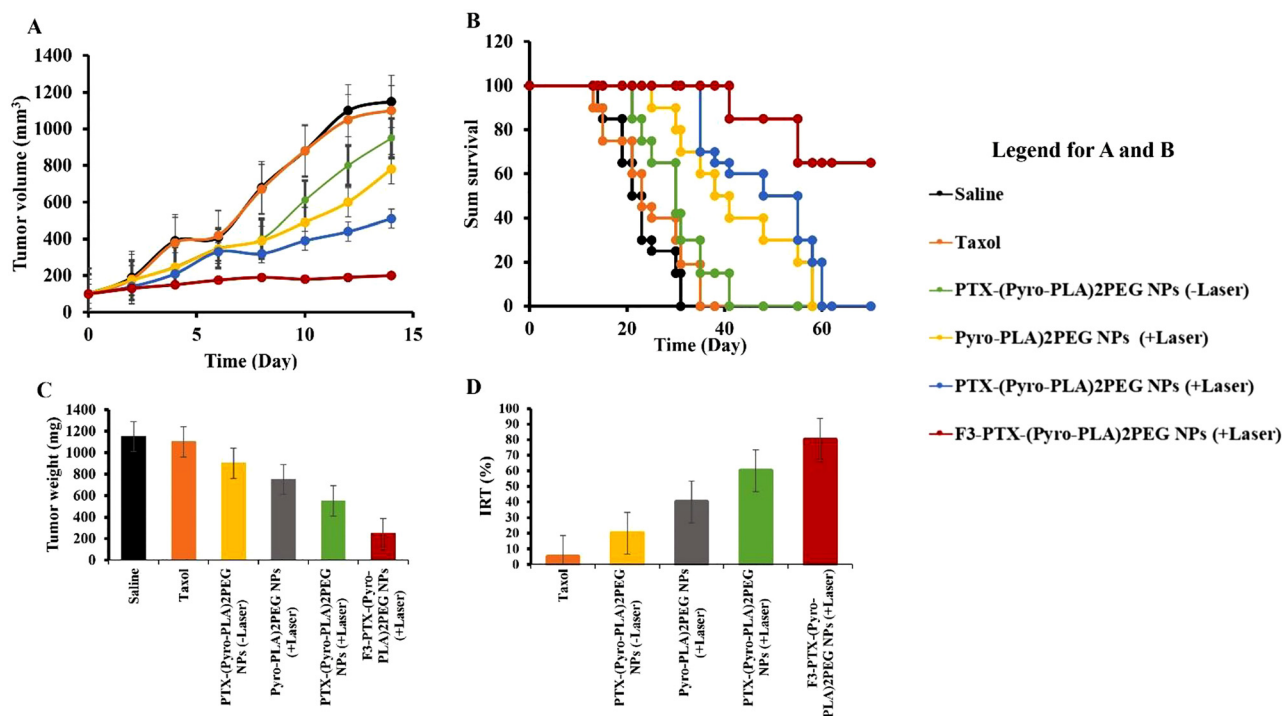


Figure 28: Antitumor effect with 2.5 mg/kg of Pyro, (Pyro-PLA)₂PEG NPs, PTX-(Pyro-PLA)₂PEG NPs and F3-PTX-(Pyro-PLA)₂PEG NPs, respectively, with or without irradiation for 9.8 min with a 660 nm laser, 170 mW cm⁻².

The mice given with saline were applied as the negative control. (A) Changes in tumor volume of mice during the 14 days experimental period. (B) Kaplan–Meir survival curve of mice. (C) Weight of dissected tumors. (D) Tumor-growth inhibition (IRT) rate of the various treatment strategies.

Adapted from Feng et al. [64].

did not affect their ¹O₂ production. Due to the poor cell affinity of these SPION-TPP NPs in B78-H1 murine amelanotic melanoma cells, the authors conjugated a TAT peptide functionalized with rhodamine (Rhod-TAT) to the SPION-TPP NPs. The *in vitro* photodynamic effect of Rhod-TAT-SPION-TPP NPs was evaluated in B78-H1 cells after laser illumination at 543 nm (14 J cm⁻², 30 min). An IC₅₀ value of 500 nM was estimated. The rhodamine fluorescence was used to verify the incorporation of the targeted Rhod-TAT-SPION-TPP NPs into the cells (Figure 30) [83].

In 2017, Gao et al. synthesized a new polymeric NP decorated with tumor acidity (pHe)-activatable TAT peptide and loaded with Ce6 PS and Gd³⁺ contrast agent (D^ATAT-NP). These NPs were developed for the treatment of pancreatic cancer through fluorescence/MRI-guided PDT. D^ATAT-NP comprised two diblock copolymers, PCL₄₅-*b*-PAEP₃₅-Cya/DTPA and D^ATAT-PEG₇₇-*b*-PCL₂₅. The targeting effect of the TAT peptide was inactivated by masking the amines of the TAT lysine residues with 2,3-dimethylmaleic anhydride (DA). *In vitro* studies were performed on pancreatic BxPC-3 cancer cells incubated with different concentrations (Ce6 equivalent) of free Ce6, TAT-NP, D^ATAT-NP and succinic anhydride TAT-NP (*i.e.* S^ATAT-NP)

in a medium with pH adjusted at 6.5 or 7.4, the extracellular pH of tumor and normal tissues, respectively. 4 h post-incubation, a NIR laser irradiation (660 nm, 0.5 W cm⁻²) was applied for 20 min. Figure 31 showed that the cell viability decreased linearly with the increase in the Ce6 concentration. Moreover, it was revealed that no significant difference was observed due to pH in TAT-NP and S^ATAT-NP. Conversely, D^ATAT-NP had a significant increasing effect on cell death when pH decreased. The intracellular ROS generation in BxPC-3 cancer cells was investigated under both pH conditions with all the tested compounds at a concentration of 20 mg mL⁻¹ (Ce6 equivalent). ROS were detected using the DCFH-DA reagent. A similar ROS production was detected for all the three NPs in water [84].

The *in vivo* studies were then realized on BxPC-3 xenograft-bearing mice, with a tumor volume around 100 mm³ (Figure 32). Cancer tissues were imaged by fluorescence 48 h after IV-injection of free Ce6, TAT-NP, D^ATAT-NP, and S^ATAT-NP. D^ATAT-NP treated mice exhibited the highest Ce6 fluorescence in the tumor when compared to other NPs and free Ce6. In healthy tissues, no difference was observed. This was in favor of a process in which

Table 3: The summary of NPs conjugated with PSs and F3 targeting peptides in terms of different parameters.

Reference	NPs	PS	Coupling between NPs and PS	NPs size (nm)	$\lambda_{\text{excitation}}$ (nm)	ϕ_F	$\Delta_{0,S}$	NPs@PS@F3-Peptide	
								<i>in vitro</i>	<i>in vivo</i>
F3-peptide targeting									
[77]	Polyacrylamide (PAA)	Methylene blue (MB)	Amide bond	55.8 ± 5.0 for MB-conjugated PAA NPs	647	nd	nd	MDA-MB-435, F98, MCF-7 9L	nd
[79]	Hydroxyl-poly(lactic acid) ₁₉₀₀ 0-poly(ethylene glycol) ₃₀₀₀ poly(lactic acid) ₁₉₀₀ 0-hydroxyl (HO-PLA-PEG-PLA-OH)	Pyropheophorbide-a (Pyro)	Ester bond	109.81 ± 3.55 for PTX-(Pyro-PLA) ₂ PEG NPs	660	nd	nd	HUVEC HCT-15	Male BALB/c nude mice
[76]	3-aminopropylmethacrylamide0 encapsulating Iron oxide	Photofrin®	Encapsulation	40 for F3-targeted NPs	630	nd	nd	MDA-MB-435	Rat 9L glioma in male Fischer 344

nd, not determined.

^{DA}TAT-NP had a prolonged blood circulation lifetime. In addition, the acidic environment in the tumor reactivated the masked TAT peptide, leading to an important reduction in the tumor volume by more than 65% after 16 days of therapy [84].

In 2019, Wan et al. combined PDT, PTT, and chemotherapy in order to treat breast cancer cells. The fluorescent infrared dye, IR780, was first conjugated with the nuclear targeting TAT peptide. Then, TAT-IR780 and chemotherapeutic Dox self assembled using hydrophobic interactions to afford TID NPs (TAT-IR780-Dox). These NPs possessed a size of around 100 nm. For comparative reasons, the authors also tested TAT-IR780 in the absence of Dox (TIR). *In vitro* studies were performed on 4T1 cancer cells. 2- and 6-h post incubation, it was revealed that the fluorescence significantly increased when the NPs (TID or TIR) were administrated instead of IR780 alone. This proved the greater internalization of both NPs in the nuclear region (Figure 33) [85]. 24 h after irradiation (785 nm, of 1.0 W cm⁻², 5 min), the viability of the cells treated with Dox, IR780, TIR, and TID reached 60, 35, 20% and >10%, respectively. This synergetic effect was also validated *in vivo* when 4T1 tumor-bearing mice were treated then sacrificed 6 h later. The 100 mm³ tumor was nearly ablated 6 days posttreatment with TID NP and IR irradiation, however, it was increased again, very slight, after 18 days (Figure 34) [85].

Table 4 describes the NPs@PS@peptide systems, targeting $\alpha_v\beta_3$ integrin, regarding the types of NPs, PSs, and the coupling between them, in addition to the NPs size, excitation wavelength ($\lambda_{\text{excitation}}$), fluorescence quantum yield (ϕ_F), singlet oxygen quantum yield ($\Delta_{0,S}$), and the results obtained *in vitro* and/or *in vivo*.

2.5 Peptide targeting EGFR

Epidermal growth factor receptor (EGFR) has a role in the tumor progression in several cancers. EGFR also promotes tumor proliferation, angiogenesis and metastasis. The overexpression of EGFR in many types of cancer cells makes it a good candidate for targeted PDT [86]. The HER2 gene, one of the members of the EGFR family is expressed in two copies in healthy cells [87]. The modification of this gene and its amplification causes tumor proliferation.

2.5.1 NPs@PS@HER2 3-340

Narsireddy et al. synthesized 35–40 nm sized multimodal NPs constituting of an Fe₃O₄ core and a chitosan shell. The chitosan-covered Fe₃O₄ NPs were then deposited with

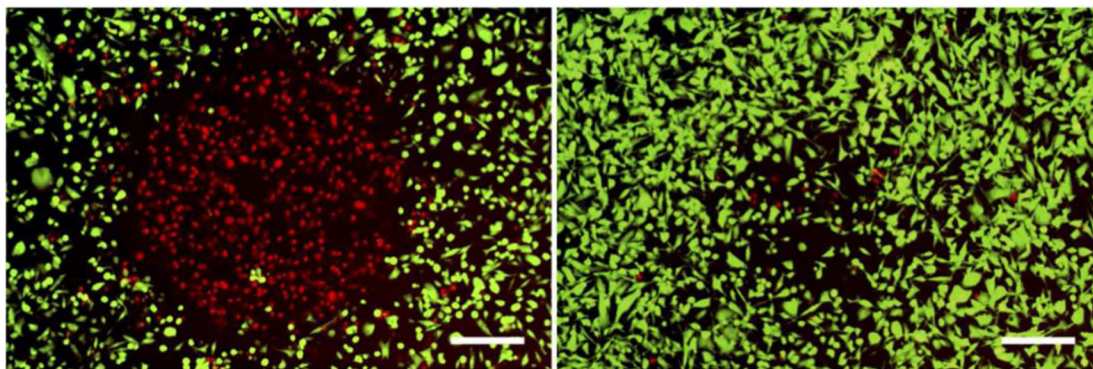


Figure 29: Viability staining of BT-549 breast cancer cells incubated with AuNS-DTDC@SiO₂-PpIX-TAT NPs (left) and AuNS-DTDC@SiO₂-TAT NPs particle concentration of 0.1 nM (right) after 30 s of light irradiation 4.4 W cm⁻² for 30 s (mercury arc lamp, filtered at 633 nm). Live cells are stained green and dead cells are stained red. Scale bars are 250 μm [67]. With permission from American Chemical Society.

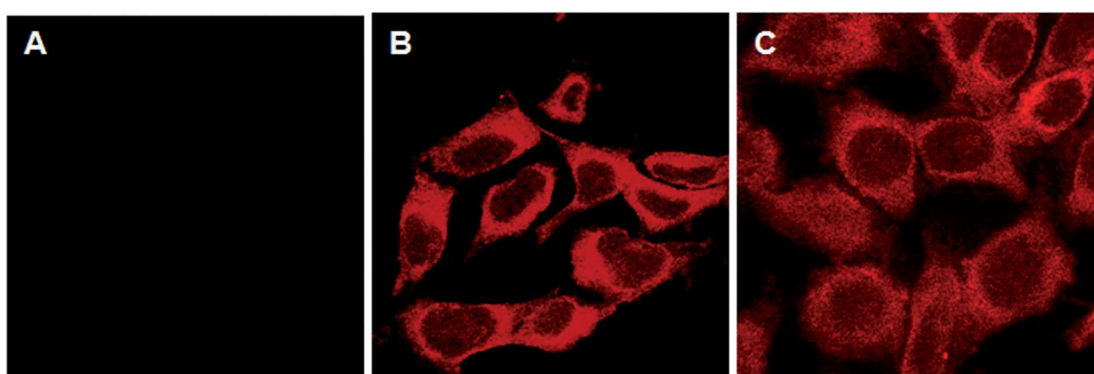


Figure 30: Cellular uptake by confocal laser microscopy. Images of B78-H1 cells (A) untreated and treated with 400 nm Rhod-TAT-SPION-TPP after incubation for (B) 3 h and (C) 24 h [68]. With permission from John Wiley and Sons.

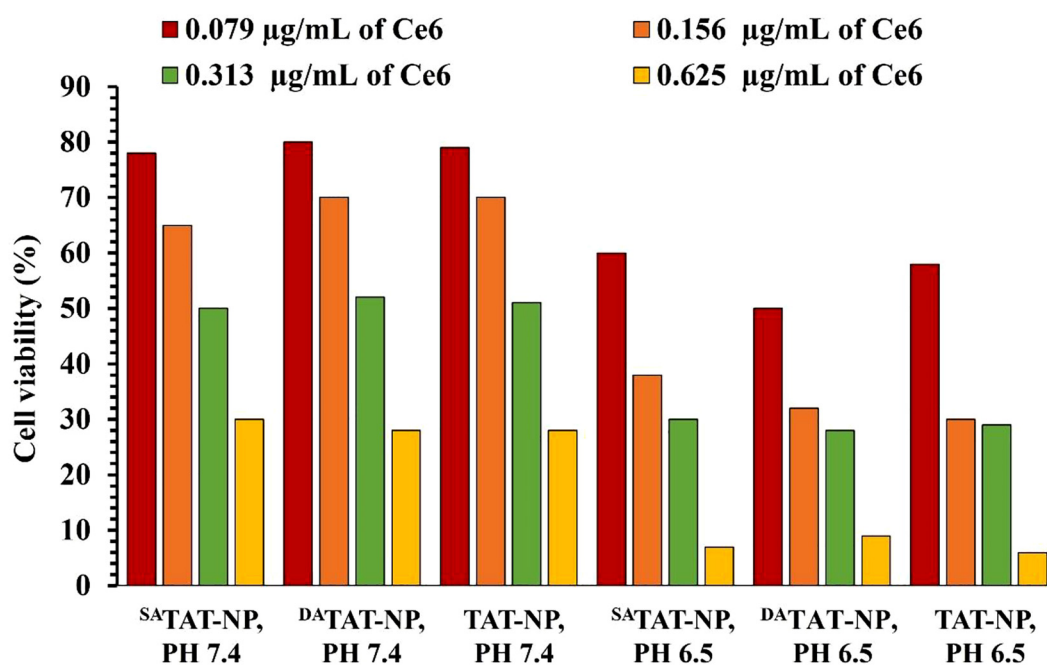


Figure 31: The cytotoxicity performance of ^{DA}TAT-NP, ^{SA}TAT-NP, and TAT-NP performance in BxPC-3 cells with NIR laser irradiation (660 nm, 0.5 mW cm⁻²) for 20 min. Adapted from Gao et al. [69].

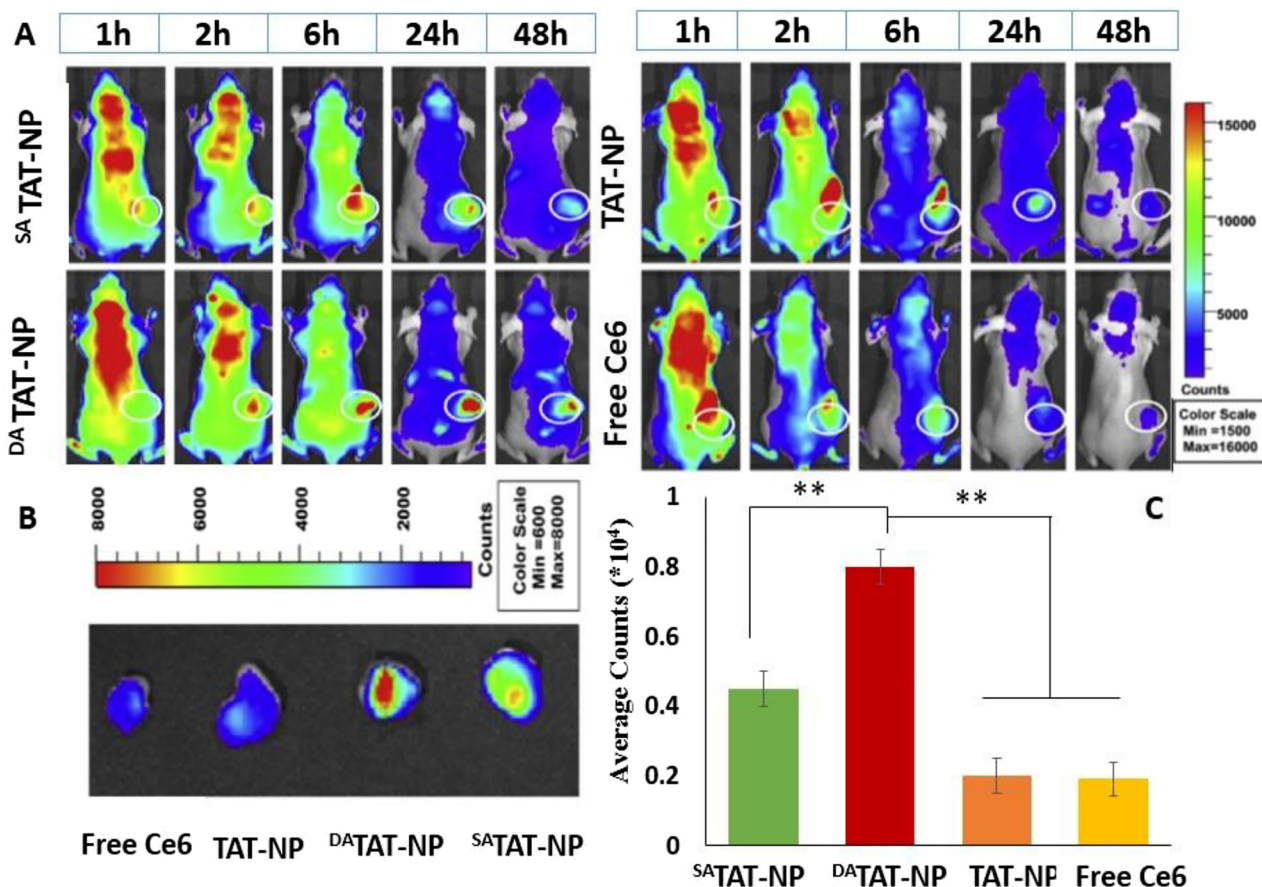


Figure 32: (A) Fluorescence images of BxPC-3 xenograft-bearing mice after IV-injection of DATAT-NP, SATAT-NP, and TAT-NP at different times. The tumor sites are denoted by white circles. (B) Ex vivo images of tumors excised at 48 h post injection. (C) Quantification of Ce6 fluorescence in the tumors, as performed in (B) by the average counts.

All of these experiments are on 2.5 mg Kg^{-1} Ce6, 660-nm laser, 0.5 mW cm^{-2} , 20 min. Adapted from Gao et al. [69]. With permission from Elsevier.

gold NPs. 5,10,15,20-tetrakis(4-hydroxyphenyl)-21H,23H-porphine (tHPP) PS was attached *via* a lipionic acid linker to the gold NPs. A human EGFR2 (or HER2) targeting peptide, known as HER2 3–340 (MGSSHHHHHH SGLVPRGSH MGVDNKFNKE MRNAYWEIAL LPNLNNQQR AFIRSLYDDP SQSANLLAEA KKLNDQAQPK), was finally attached to the chitosan shell *via* a nickel-nitrilotriacetic acid linker. The uptake assays were performed in ovarian SKOV-3 cells. The obtained IC_{50} values for the PS alone, the nontargeted NPs and the targeted Peptide-NPs were 0.75, 2.1, and 1.7 μM , respectively. The addition of the peptide did not significantly improve the selectivity for HER2. The positive effect of the NPs was demonstrated by the decrease of the dark cytotoxicity compared to the PS alone. The *in vivo* distribution was studied in FoxN1 nude mice. 24 h after the injection of the nontargeted and the targeted peptide-NPs in the tumors, the estimated gold amount (ng of Au/gm of wet tissue) was found to be 477.5 ± 128 and 1794.2 ± 505 , respectively,

while a value of 361.4 ± 78 was recorded in the normal tissue. These outcomes validated the advantage of adding a peptide targeting HER2. Twenty four hours after the injection, PDT was performed (PDT-1200 set up, 640–720 nm, 120 J cm^{-2} , 200 mW cm^{-2} , 10 min). A notable retarding effect on tumor growth was observed with the targeted NP (Figure 35) [88].

One year later, the same team synthesized a fourth generation poly(amidoamine) (PAMAM) dendrimer (*i.e.* DPN and ADPN) coupled to the same PS and the same peptide to target HER2. Using confocal microscopy, the authors observed a greater fluorescence with the targeted ADPN dendrimer than with the nontargeted DPN dendrimer in SKOV-3 cells. PDT was performed on SKOV-3 (+) and human breast cancer MCF-7 cells (–) (PDT-1200 set up, 20 J cm^{-2} , 50 mW/cm^2 , 6.5 min). The IC_{50} values were 0.175, 0.100 and 0.075 μM for the PS, the nontargeted DPN dendrimer and the targeted ADPN dendrimer, respectively. In

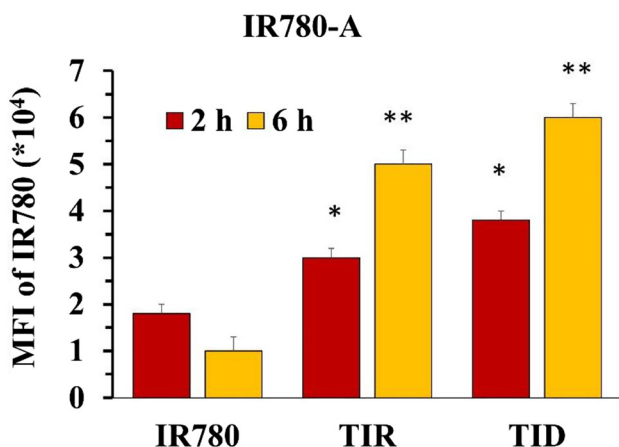


Figure 33: Quantitative analysis by flow cytometry of mean fluorescence intensity (MFI) of intracellular IR780 in 4T1 cells after 2- and 6-h incubation with free IR780, TIR, and TID NPs * $P < 0.05$ and ** $P < 0.01$ as compared to the control (785 nm, of 1.0 W cm^{-2} , 5 min). Adapted from Wan et al. [70].

MCF-7 cells, no difference in the IC_{50} values was detected between the PS and both dendrimers. The *in vivo* phototoxicity experiments (PDT-1200 set up, 120 J cm^{-2} , 200 mW/cm^2 , 10 min) revealed a delay in the tumor growth when exposed to the nontargeted DPN dendrimer or to the targeted ADPN dendrimer. However, no photodynamic effect was observed in tumors exposed to PBS (untreated) or PS alone. It seemed that grafting the targeted peptide did not enhance the efficacy of PDT [89].

2.5.2 NPs@PS@GE11

GE11 is a dodecapeptide with 12 amino acids (YHWY-GYTPQNVI). Its affinity towards EGFR was identified by Li et al. GE11 has a lower affinity for EGFR ($k_d = 22 \text{ nM}$) than EGF ($k_d = 2 \text{ nM}$). It increases the endocytosis of the NPs due to an alternative EGFR-dependent actin-driven pathway. It has been shown that the EGFR level stays constant after the incorporation of GE11, indicating an EGFR recycling process with a prolonged cell receptivity for the circulating GE11 [90]. In 2012, Master et al. developed PEG-co-poly-caprolactone (PEG-PCL) NPs encapsulating phthalocyanine 4 (Pc4) PS and covalently coupled to GE11 peptide ligand to target EGFR overexpressed on many cancer cell lines. For their *in vitro* studies, the authors selected A431 human epidermoid carcinoma cells and MCF-7 human breast cancer cells overexpressing EGFR. After 1 and 5 h of incubation, a better accumulation into A431 (+) cells was observed for the targeted NPs as compared to the untargeted ones. However, no accumulation was witnessed into

the MCF-7 (–) cells. This was in favor of the receptor-mediated internalization of the targeted NPs. Twenty four hours post incubation, no difference was detected between both NPs. This was due to the processes of passive uptake relying on the EPR effect and the active uptake *via* the EGF receptors. After 200 s of light illumination (diode array, 675 nm , 200 mJ cm^{-2}), it was revealed that the cell viability evolves linearly with the amount of the accumulated NPs. The higher the accumulation, the greater the cell death. In the same year [91], the authors optimized various parameters, *i.e.* the density of the GE11 peptide ligand on the micelle surface, the Pc4 loading and the light dose, in order to enhance the PDT efficiency. They discovered that the micelle formulation should be of 10% mole GE11-modified polymer and $50 \mu\text{g Pc4}$ per mg of polymer. In addition, the illumination using the light-emitting diode array (675 nm , 200 mJ cm^{-2}) was prolonged to 400 s [92].

Table 5 describes the NPs@PS@peptide systems, targeting $\alpha_v\beta_3$ integrin, regarding the types of NPs, PSs, and the coupling between them, in addition to the NPs size, excitation wavelength ($\lambda_{\text{excitation}}$), fluorescence quantum yield (ϕ_F), singlet oxygen quantum yield ($\Delta_{O,S}$), and the results obtained *in vitro* and/or *in vivo*.

2.6 Peptides targeting vascular endothelial tumor

Tissue transglutaminase (TGM2) is a multifunctional protein that has been found to be a molecular marker of colorectal cancer [94]. It is mainly located in the cytoplasm and is involved in the cell growth and differentiation, remodeling and stabilization of extracellular matrix. TGM2 is overexpressed in different cancers such as ovarian, breast and colon cancers. The GX1 peptide (CGNSNPKSC) is an important new vector for targeting TGM2 and tumor vessels such as colorectal orthotopic vessels [95, 96].

2.6.1 NPs@PS@GX1

In 2017, Guo et al. developed new angiogenic vessel-targeting (AVT) NPs as delivery vehicles for a hypoxia-activated bioreductive prodrug (Tirapazamine, TPZ). The AVT NPs were formed by the self assembly of a TPC-GX1 conjugate. This conjugate was composed of the TPC PS (5-(4-carboxyphenyl)-10, 15,20-tris(3-hydroxyphenyl)chlorin) covalently linked to an angiogenic vessel-targeting cyclopeptide GX1. The elaborated NPs had an average hydrodynamic size of about 109 nm. TPZ was then loaded on the AVT-NPs, at a capacity of 11.08%. The synthesized

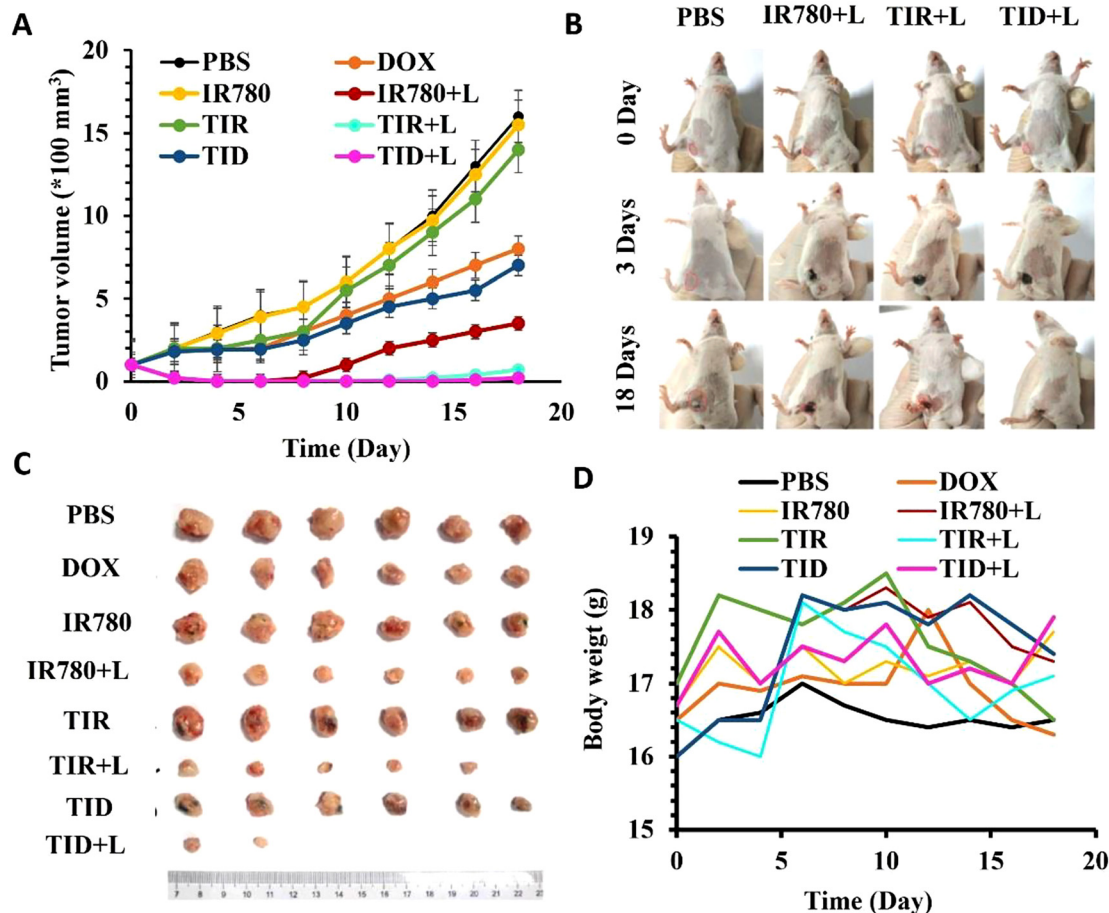


Figure 34: Synergistic antitumor effects of TID NPs-mediated trimodal treatment of nucleus-targeted PTT/PDT and chemotherapy in 4T1 tumor-bearing mice. (A) Tumor growth curves of the mice treated with free Dox, free IR780, TIR, and TID NPs combined with (+L) and without laser irradiation. (B) Photos of the mice at 0-, 3-, and 18-days post-treatment with free IR780, TIR, and TID NPs combined with laser irradiation (+L). Red cycles indicate the recurrent tumors. (C) Photo of the tumors derived from the mice at the end of various treatments (D) Body weight changes of the mice with various treatments.

** $P < 0.01$ for comparison between two treatment groups. IR780 and Dox doses were 1.0 and 0.5 mg kg^{-1} , respectively. Laser irradiation was carried locally at the tumor at 785 nm at a power density of 1.0 W cm^{-2} for 5 min . Adapted from Wan et al. [70]. With permission from Elsevier.

AVT-NP/TPZ system was designed for application in the chemo-photo synergistic cancer therapy. TPC-PEG micelles and chemotherapeutic cisplatin were used to track the distribution of the AVT-NPs and to demonstrate their targeting capability. The *in vitro* studies were performed on MCF-7, 3T3 and HUVEC cells. As for the *in vivo* assays, they were conducted on MCF-7 and MDA-MB-231 xenograft mouse models. After exposure to the He-Ne laser irradiation (650 nm , 1.2 W cm^{-2} , 10 min), TPC, in the AVT-NP/TPZ system, interacted with the molecular oxygen to produce $^1\text{O}_2$ that initiated firstly the cancer cell killing by PDT. The PDT-induced hypoxia triggered a promoted angiogenesis, thus resulting in an enhanced targeted delivery of the NPs specifically to the tumor site, in addition to the activation of the bioreductive prodrug TPZ, that in its turn generate highly cytotoxic free radicals for a combinational

chemophototherapy (Figure 36). This work showed the great potential of using hypoxia-induced enhancement of angiogenesis to mediate a specific accumulation of the NPs at the tumor site and initiate a chemo-photo combinational treatment [97].

Table 6 describes the NPs@PS@peptide systems, targeting $\alpha_v\beta_3$ integrin, regarding the types of NPs, PSs, and the coupling between them, in addition to the NPs size, excitation wavelength ($\lambda_{\text{excitation}}$), fluorescence quantum yield (ϕ_f), singlet oxygen quantum yield (Δ_{O_2}), and the results obtained *in vitro* and/or *in vivo*.

2.6.2 Peptide targeting p32

The p32 protein is a trimer with three homologous subunits [98]. It is a mitochondrial matrix protein in normal tissues,

Table 4: The summary of NPs conjugated with PSs and cell penetrating peptides in terms of different parameters.

Reference	NPs@PS@Cell Penetrating Peptide.				
	PS	Coupling between NPs and PS	NPs size (nm)	$\lambda_{excitation}$ (nm)	ϕ_F $\Delta_{0.5}$ <i>In vitro</i> <i>In vivo</i>
	TAT Peptide				
[83]	Superparamagnetic iron oxide (SPION)	5-(4-Carboxyphenyl)-10,15,20 triphenyl-porphyrin (TPP)	Click chemistry	White halogen lamp	nd nd B78-H1 nd
[82]	Gold nanostar (AuNS)	Photoporphyrin IX (PpIX)	SiO ₂ -PpIX coating	377	nd nd BT-549 nd
[84]	PCL ₄₅ -b-PAEP ₃₅ -Cya/DTPA and ^D TAT-PEG ₇₇ -b-PCL ₂₅ blocks copolymers	Chlorin e6 (Ce6)	Encapsulation	660	nd nd BxPC-3 BxPC-3 xenograft-bearing mice
[85]	Self-assembly of TAT-IR780 and Dox	IR780	Self assembly	785	nd nd 4T1 4T1 tumor bearing mice

*nd, not determined.

but it can also be detected on the cell surface, nucleus, and endoplasmic reticulum. p32 is overexpressed on the cell membrane of certain human cancers making it a useful target in tumor diagnosis and therapy.

α -Helix p32 is a stick-shaped peptide expressed in the main cancer types. The coupling of α -helix p32 with anti-cancer drugs plays a rigorous role in targeting more than 50% of human cancers [99, 100].

2.6.3 NPs@PS@ α -helix p32 membrane

In 2015, Zhang et al. described a new approach, called conformational epitope imprinting, to develop new targeted nanocarriers using the three-dimensional conformation of an epitope, rather than its linear structure, for the specific recognition of p32 membrane protein. To achieve this goal, the authors produced the HAPPE peptide (*i.e.* hybrid apamin-p32 polypeptide). It consisted of a disulfide-linked α -helix-containing peptide, *i.e.* apamin, which mimics the extracellular structured N-terminal region of the p32 membrane protein, where seven residues were replaced by topologically equivalent ones from p32. For epitope imprinting, they designed molecularly imprinted polymeric NPs (MIPNPs), possessing selective cavities for the specific recognition of p32 membrane protein, using the HAPPE peptide as template. MIPNPs had a particle size of 37 nm. Nonimprinted polymeric NPs (NIPNPs), using a linear analog of HAPPE peptide (*i.e.* four cysteines of apamin were replaced by alanines), were also synthesized to demonstrate the specific recognition. Compared to NIPNPs, a strong binding interaction of the MIPNPs with p32 was observed. A fluorescence probe, 6-aminofluorescein (FAM), was encapsulated into MIPNPs and NIPNPs. The uptake of both NPs by p32-positive cancer cells, namely 4T1 murine breast cancer and BxPC-3 human pancreatic cancer cells was assessed by flow cytometric measurement. MIPNPs displayed a greater cellular uptake as compared to NIPNPs. The *in vivo* biodistribution of MIPNPs and NIPNPs, both encapsulating a near-infrared fluorophore (IR-783 dye), was also studied using 4T1-tumor-bearing mice. A higher accumulation in tumors was presented by MIPNPs. The pre injection of Lyp-1 peptide, known to bind specifically to the N-terminal region of p32, significantly reduced this accumulation. This result confirmed that MIPNPs specifically bound to the targeted p32 protein. The *in vivo* antitumor effect of methylene blue (MB)-loaded NPs (MIPNPs and NIPNPs) was evaluated using laser light irradiation at 650 nm (800 mW cm⁻², 10 min). It was demonstrated that the MB-loaded MIPNPs exhibited an efficient targeted photodynamic therapy (Figure 37) [101].

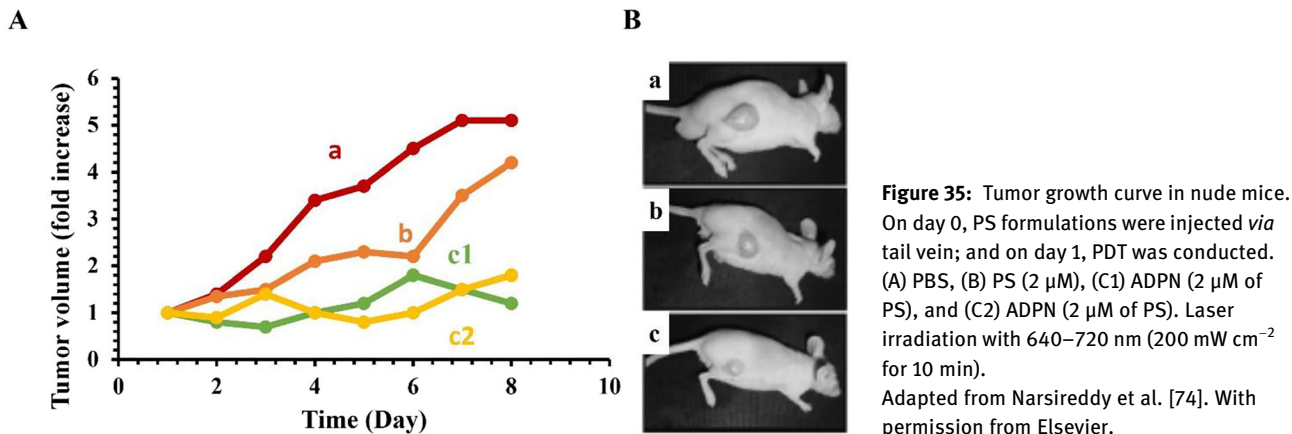


Table 5: The summary of NPs conjugated with PSs and human EGFR targeting peptides in terms of different parameters.

NPs@PS@Peptide targeting human EGFR										
Reference	NPs	PS	Coupling between NPs and PS	NPs size (nm)	$\lambda_{excitation}$ (nm)	ϕ_F	$\Delta_{O.S}$	<i>In vitro</i>	<i>In vivo</i>	
HER2 3–340 Peptide										
[89]	Dendrimer (G4)	5,10,15,20-Tetrakis (4-hydroxyphenyl)-21 <i>H</i> ,23 <i>H</i> -porphine (tHPP)	Amide bond	10 for DPN and ≈100–200 for ADPN	640	nd	nd	SKOV-3 MCF-7	FoxN1 Nude mice	
[88]	Fe ₃ O ₄ -Chitosan-Au	5,10,15,20-Tetrakis (4-hydroxyphenyl)-21 <i>H</i> ,23 <i>H</i> -porphine (tHPP)	Ester bond	35–40 for Fe ₃ O ₄ NPs and 35 for MGPS ^a	640	nd	nd	SKOV-3	FoxN1 Nude mice	
GE11 Peptide										
[93, 94]	Polyethylene glycol-co-polycaprolactone (PEG-PCL)	Phthalocyanine 4 (Pc4)	Encapsulated	<100 for Pc4 in PEG-PCL micelles	675	nd	nd	A431 MCF-7c3		nd

^a MGPS: Magnetic/gold particles with PS, *nd, not determined.

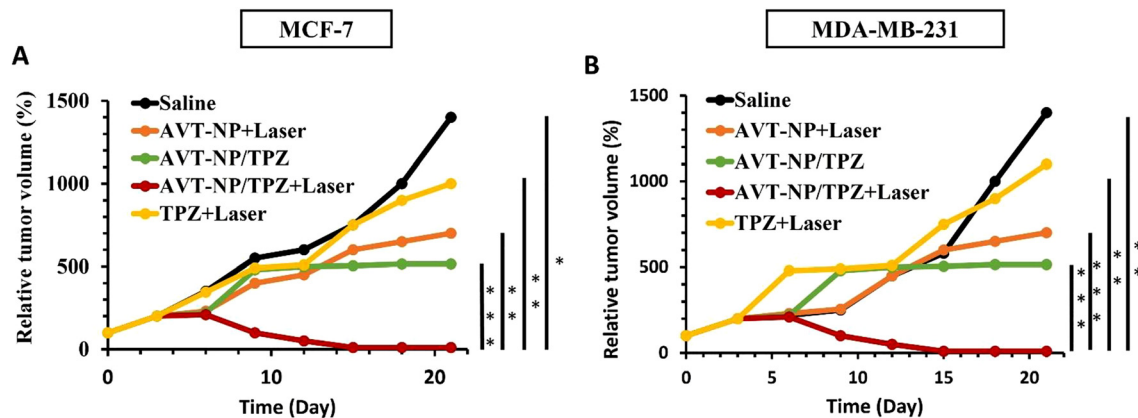


Figure 36: MCF-7 tumor (A) and MDA-MB-231 (B) growth curves after intravenous injection of different drug formulations (0.1 mg/kg; Ps/body weight).

Error bars indicate standard deviations ($n = 5$). * $P < 0.05$, ** $P < 0.01$, *** $P < 0.001$ (two-tailed Student's-test). He–Ne laser irradiation (650 nm, 1.2 W/cm² for 10 min). Adapted from Guo et al. [82].

Table 6: The summary of NPs conjugated with PSs peptides targeting tumor vasculature endothelium in terms of different parameters.

NPs@PS@Peptide targeting tumor vasculature endothelium									
Reference	NPs	PS	Coupling between NPs and PS	NPs size (nm)	$\lambda_{\text{excitation}}$ (nm)	ϕ_F	$\Delta_{O,S}$	<i>In vitro</i>	<i>In vivo</i>
GX1 cyclopeptide									
[97]	Self assembly of TPC/GX1-TPZ	5-(4-Carboxyphenyl)-10,15,20-tris(3-hydroxyphenyl) chlorin (TPC)	Self assembly	109 for AVT-NP/TPZ	650	nd	nd	MCF-7, 3T3, HUVEC	MCF-7 and MDA-MB-231 xenograft mice models

nd, not determined.

Table 7 describes the NPs@PS@peptide systems, targeting $\alpha_v\beta_3$ integrin, regarding the types of NPs, PSs, and the coupling between them, in addition to the NPs size, excitation wavelength ($\lambda_{\text{excitation}}$), fluorescence quantum yield (ϕ_F), singlet oxygen quantum yield ($\Delta_{O,S}$), and the results obtained *in vitro* and/or *in vivo*.

2.7 Peptide to target transferrin

Transferrin receptor (TfR) is also considered an attractive receptor for the targeted therapy since it is overexpressed on the surface of many cancer cells [102] and it is mostly expressed in epithelial cells. It is used to transfer iron from the liver to the bone marrow for incorporation into hemoglobin within red blood cells and distribution throughout

the body [103]. Subsequently, the survival of human cells compels the body to manufacture transferrin. This emphasizes the importance of coupling transferrin to the NPs to improve the selectivity of PDT [104].

In 2017, Zhang and coworkers designed enzyme- and pH-responsive nanocarriers (UCNP@mSiO₂-Ce6) with a size of 75 nm. These nanocarriers consisted of an UCNP (NaYF₄:Yb,Er@NaYF₄) core embedded in a mesoporous silica shell (mSiO₂) doped with Ce6 PS. They were then surface-functionalized with transferrin (Tf) for targeting TfR overexpressed in tumor cells. In addition, Dox chemodrug was further loaded on the NPs, with an efficiency of about 4%, through a succinic acid-peptide linker (succinic acid-Gly-Phe-Leu-Gly, SGFLG linker). This linker established the pH- and enzyme-triggered drug release of Dox. The resulted enzyme/pH-responsive multifunctional

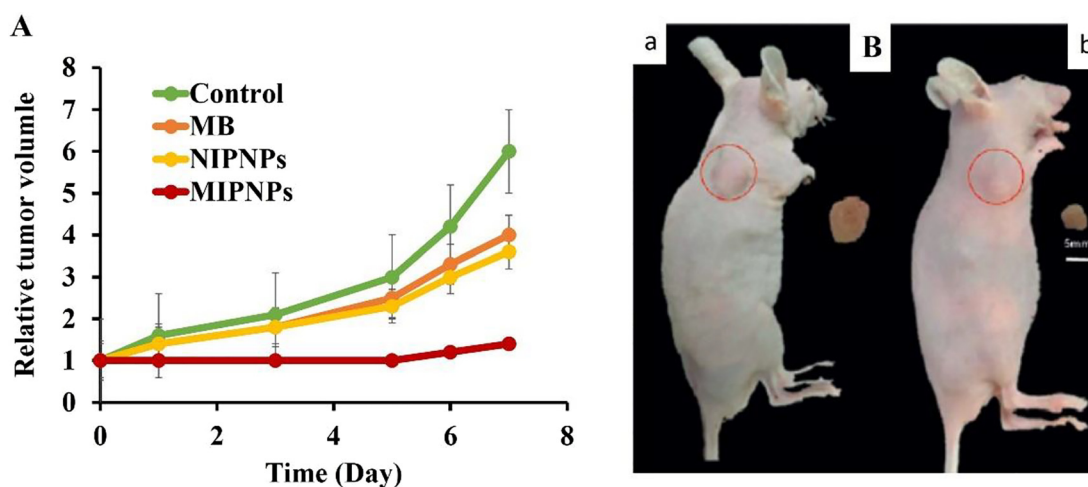


Figure 37: (A) *In vivo* antitumor effect of PDT on 4T1-tumor bearing mice performed using distinct NP formulations. All injections were performed once at $t = 0$, MIPNPs (1 mg/mL) loaded with the photosensitizer methylene blue (MB, 3 μm). Tumor volumes were measured every other day for one week. (B) Images of mice treated with (a) NIPNPs and (b) MIPNPs.

Scale bar = 5 mm 650 nm laser light irradiation, 800 mW cm^{-2} , 10 min. Adapted from Zhang et al. [86]. With permission from John Wiley and Sons.

Table 7: The summary of NPs conjugated with PSs and peptides targeting tumor suppressor protein p32 in terms of different parameters.

NPs@PS@Peptide targeting tumor suppressor protein p32									
Reference	NPs	PS	Coupling between NPs and PS	NPs size (nm)	$\lambda_{\text{excitation}}$ (nm)	ϕ_F	$\Delta_{0.5}$	<i>In vitro</i>	<i>In vivo</i>
α -helix containing peptide, apamin									
[101]	Molecularly imprinted polymeric (MIPNPs)	Methylene blue (MB)	Encapsulated	37 for MIPNPs	650	nd	nd	4T1 BxPC-3	4T1-Tumor-bearing mice

nd, not determined.

nanocomposite (UCNP@mSiO₂/Ce6-Dox-SGFLG-Tf) was developed for application in synergistic PDT and chemotherapy. After the endocytic uptake of the nanocomposite into the tumor cells by pinocytosis or phagocytosis, various steps took place. First of all, the pH- and enzyme-triggered Dox release occurred due to the high concentration of cathepsin B and the low pH condition, thus illustrating a chemotherapeutic effect. Secondly, a 5 min NIR irradiation of UCNPs (980 nm, 0.5 W cm⁻²) led to a visible-light emission, which enabled the efficient excitation of Ce6 and the further generation of ROS, illustrating a photodynamic effect. The enzyme- and pH-dependent Dox release from UCNPs@mSiO₂/Ce6-Dox-SGFLG-Tf was estimated in PBS using different parameters. With the pH fixed at 6.8, better values were obtained at high cathepsin concentration, for example 60.17% of Dox were released at 2 × 10⁻⁷ mol/L. By testing various pH conditions, from 1.2 to 6.8, better values were obtained at low pH, for instance 78.36% of Dox was released at pH 1.2. The *in vitro* cell viability assays were carried out on cancerous HeLa cells and L02 normal human liver cells. These tests demonstrated a synergistic PDT and chemotherapeutic effect under NIR irradiation. This effect was more drastic using UCNPs@mSiO₂/Ce6-Dox-SGFLG-Tf nanocomposite and NIR irradiation (980 nm, 0.5 W cm⁻², 15 min) leading to a HeLa cell viability of 33% (Figure 38) [105].

Table 8 describes the NPs@PS@peptide systems, targeting $\alpha_v\beta_3$ integrin, regarding the types of NPs, PSs, and the coupling between them, in addition to the NPs size, excitation wavelength ($\lambda_{\text{excitation}}$), fluorescence quantum yield (ϕ_F), singlet oxygen quantum yield ($\Delta_{0.5}$), and the results obtained *in vitro* and/or *in vivo*.

2.8 Peptide to target PD-1

Programed death-1 (PD-1) is a cell surface molecule that regulates the adaptive immune response [106]. The

engagement of PD-1 by its PD-L1 or PD-L2 ligands transduces a signal that inhibits *T* cell proliferation, cytokine production, and cytolytic function. *T* lymphocytes are white blood cells that are specialized in certain immune reactions. It helps fight infections and destroy abnormal cells, including cancer cells.

In 2020, B. Liu et al. described the development of multifunctional PEG-coated gold nanoprisms (GNPs) incorporating Ce6 PS and coupled to PD-L1 targeting peptide [96]. These NPs were designed for enhanced imaging and PTT/PDT applications. Using NIR and photoacoustic imaging, the authors proved that the NPs presented a high affinity for PD-L1 receptors both *in vivo* and *ex vivo* in the main organs and tissues. They also showed a synergistic PDT and PTT effect leading to the inhibition of the tumor growth *in vivo*.

Table 9 describes the NPs@PS@peptide systems, targeting PD-1, regarding the types of NPs, PSs, and the coupling between them, in addition to the NPs size, excitation wavelength ($\lambda_{\text{excitation}}$), fluorescence quantum yield (ϕ_F), singlet oxygen quantum yield ($\Delta_{0.5}$), and the results obtained *in vitro* and/or *in vivo*.

2.9 Bioactive peptide targeting many cancer types

Bioactive peptides are short protein fragments of 2–20 amino acids [108]. These peptides have revealed the ability to overcome cell membranes and cause cell death [109]. Since then, bioactive peptides have been used to target tumor cells in general [108]. Some researchers cited that coupling a bioactive targeting peptide can target plasma membrane and mitochondria.

In 2019, Cheng et al. described the synthesis of a chimeric peptide that consisted of a hydrophobic PpIX PS conjugated, *via* a lysine linker, to a bioactive peptide (rFxrFxrFxr; r and Fx stand for D-arginine and L-

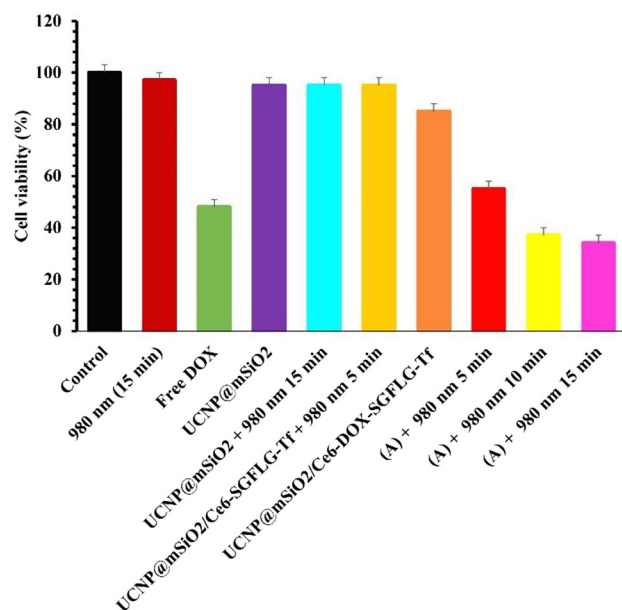


Figure 38: Cell viability of HeLa cells under pure NIR, or incubated with free Dox (equal Dox concentration with NPs), UCNP@mSiO₂, UCNP@mSiO₂/Ce6-SGFLG-Tf, and UCNP@mSiO₂/Ce6-DOX-SGFLG-Tf without and with 5, 10 or 15 min NIR irradiation (980 nm, 0.5 W cm⁻²).

Adapted from Zhang et al. [90]. With permission from Elsevier.

cyclohexylalanine, respectively). Hydrophilic PEG₈ chain was also attached at the C-terminal extremity of the peptide. This amphipathic chimeric peptide self-assembled

into spherical micelles in aqueous media, affording M-ChiP of a hydrodynamic size of about 167.9 nm. M-ChiP was used for mitochondria and plasma membrane dual-targeted PDT. The goal of this strategy was to have a M-ChiP insertion into the plasma membrane of tumor cells inducing its rupture *via* ¹O₂ generation upon laser irradiation. The membrane rupture resulted in an enhanced membrane permeability, leading to endocytosis and mitochondria targeted delivery of M-ChiP, then to mitochondria destruction by the ¹O₂ generated upon laser irradiation. The *in vitro* antitumor PDT efficacy of M-ChiP was carried out on murine mammary carcinoma 4T1 and African green monkey kidney COS7 cells using 630 nm LED light (29.8 mW cm⁻², 20 or 30 s). This study showed negligible cytotoxicity and obvious phototoxicity on 4T1 and COS7 cells in a concentration-dependent manner where less than 10–15% of the cells remained viable at 20 mg L⁻¹. The *in vivo* antitumor photodynamic efficiency was conducted in 4T1 tumor-bearing mouse using 630 nm He–Ne laser (250 mW cm⁻², 10 min). This study revealed that M-ChiP had a remarkable tumor suppression effect upon laser irradiation (Figure 39) [110].

Table 10 describes the NPs@PS@peptide systems, targeting α_vβ₃ integrin, regarding the types of NPs, PSs, and the coupling between them, in addition to the NPs size, excitation wavelength (λ_{excitation}), fluorescence quantum yield (φ_F), singlet oxygen quantum yield (Δ_{0,S}), and the results obtained *in vitro* and/or *in vivo*.

Table 8: The summary of NPs conjugated with PSs and peptides targeting BBB in terms of different parameters.

NPs@PS@Peptide targeting blood brain barrier									
Reference	NPs	PS	Coupling between NPs and PS	NPs size (nm)	λ _{excitation} (nm)	φ _F	Δ _{0,S}	<i>In vitro</i>	<i>In vivo</i>
Transferrin									
[105]	Upconversion (NaYF ₄ :Yb,Er@NaYF ₄)	Chlorin e6 (Ce6)	Mesoporous silica (mSiO ₂)-Ce6 coating	75 for UCNP@mSiO ₂ /Ce6 NPs	980	nd	nd	HeLa L02	nd

nd, not determined.

Table 9: The summary of NPs conjugated with PSs and peptides targeting PD-1 in terms of different parameters.

NPs@PS@Peptide targeting PD-1 expressed on T cells									
Reference	NPs	PS	Coupling between NPs and PS	NPs size (nm)	λ _{excitation} (nm)	φ _F	Δ _{0,S}	<i>In vitro</i>	<i>In vivo</i>
Peptide PD-1									
[107]	Gold NPs	Ce6	Ce6 adsorbed on the surface of NPs	nd	633 nm (0.8 W cm ⁻² , 3 min) <i>in vitro</i> at 633 nm (0.8 W cm ⁻² , 5 min) <i>in vivo</i>	nd	nd	Human lung cancer HCC827	nude mice

nd, not determined.

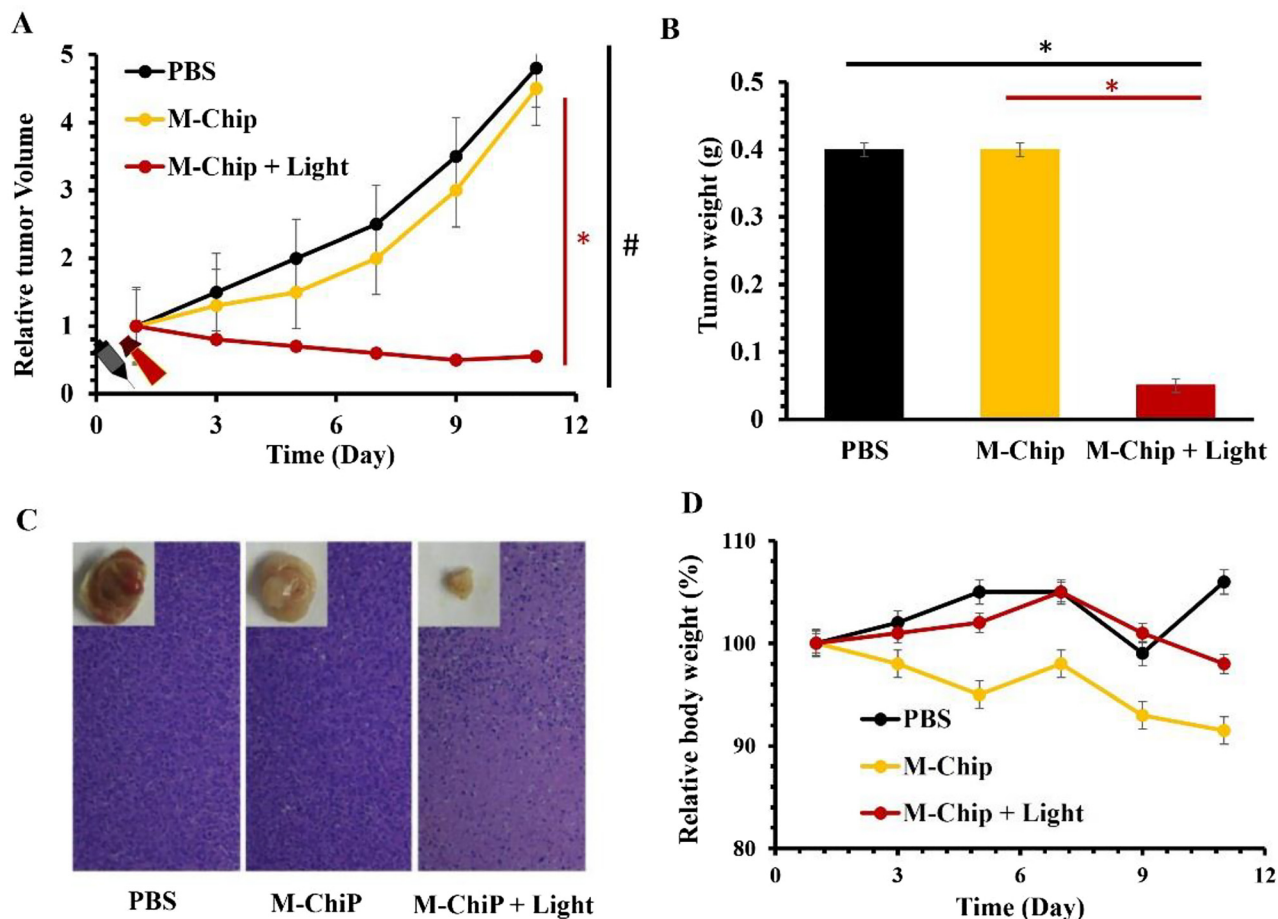


Figure 39: Antitumor study of M-Chip.

(A) The relative tumor volume changes after treatment with PBS, M-Chip ($200 \mu\text{L}$, 1.2 mg mL^{-1}), and laser irradiation (150 J cm^{-2} , 250 mW cm^{-2} for 10 min). (B) The corresponding average tumor weight and (C) the scarified tumor images and HE staining analysis of tumor tissues after various treatments at the 11th day. (D) The relative body of the mice after various treatments in 11 days. Adapted from Cheng et al. [93].

Table 10: The summary of NPs conjugated with PSs and peptides targeting human muscular nicotinic acetylcholine receptors in terms of different parameters.

NPs@PS@Peptide targeting human muscular nicotinic acetylcholine receptors									
Reference	NPs	PS	Coupling between NPs and PS	NPs size (nm)	$\lambda_{\text{excitation}}$ (nm)	ϕ_F	$\Delta_{0.5}$	<i>In vitro</i>	<i>In vivo</i>
Bioactive peptide									
[110]	Spherical micelles chimeric peptide (M-ChiP)	Photoporphyrin IX (PpIX)	Amide bond	167.9 for M-ChiP	630	nd	nd	4T1 COS7	4T1 Tumor-bearing mouse

nd, not determined.

3 Conclusion

The coupling of the peptides to the NPs enabled an important double targeting in PDT. The performed researches showed very encouraging results. The phototoxicity studies

of these NPs confirmed their efficiency. In addition, the *in vivo* results presented a remarkable tumor regression and growth inhibition. NPs@PS@Peptide was considered the best candidates for PDT, since each peptide vector targeted specific tumor cells allowing better accumulation and,

consequently, a superior photodynamic effect. Among these bioactive peptides, research results validated the effectiveness of the cell-penetrating peptides, such as TAT, that facilitated the penetration of the NPs into the cells. The *in vitro* and *in vivo* tests confirmed that the peptides DKPPR, ATWLPPR, CRGDK, and tLyp-1 targeted NRP-1 receptor, which has been evaluated in the whole sections of 65 primary breast carcinomas, 95 primary colorectal adenocarcinomas, 90 primary lung carcinomas, 59 additional human metastases, and 16 xenografts. NRP-1 immunoreactivity had been observed in normal tissue vessels adjacent to the cancer cells and in 98–100% of carcinomas. The expression of NRP-1 in tumor cells was also observed in 36% of primary lung carcinomas and 6% of primary mammary carcinomas, but not in the colorectal adenocarcinoma. NRP-1 was also evaluated in mouse embryos, where their expression was limited to the nervous system, endocardium, and vascular smooth muscle and in endothelium on subsets of vessels. Other peptides such as RGD, iRGD, cRGD, c(RGDyK), RGD-4R, RGDfK, and fibronectin (Fmp), validated, by *in vitro* and *in vivo* tests, their ability to target $\alpha_v\beta_3$ integrins that are strongly expressed in normal mammary epithelium and in other primary invasive breast carcinomas. This integrin heterodimer was also abundant in all the breast cancer and the metastatic bone cancer cells. The *in situ* hybridization revealed high levels of mRNA at steady state corresponding to the protein expression sites. In addition to NRP-1 and $\alpha_v\beta_3$ integrins, transferrin was also a receptor of interest in the targeted PDT. Transferrin (TfR) is a receptor found on the BBB. Regarding the high selective permeability imposed by BBB, the photodynamic therapy with NPs@PS@transferrin allowed the penetration of transferrin protein, thus overcoming the difficulty of treating central nervous system (CNS) diseases by standard drugs such as chemotherapy. Coupling transferrin to the nanoparticles (NPs@PS@transferrin) enabled a superior and selective accumulation. This accumulation was confirmed by the fluorescence of the PS. On this basis, the Transferrin peptide targeted successfully the brain and blood cancers. Moreover, the efficiency of targeting by α -helix p32 peptide was also assessed. This peptide targeted all the tumors overexpressing p32 protein. In addition, the efficacy of F3 Peptide to target tissue factor F3 was confirmed. This factor is responsible for activating blood clotting and is expressed in most solid tumors. Other research efforts had also verified that GX1 peptide targeted the human gastric cancer (GC) vasculature by generally binding to the endothelial cells. The overexpression of EGFR contributes to the malignant transformation of human epithelial cells indicating gene mutations. It is mostly expressed in breast cancer. Various studies validated that the peptides GX1, HER2 3–340, GE11 are important vectors

for targeting EGFR due to the overexpression of tissue transglutaminase (TGM2). TGM2 is a multifunctional protein located in the cytoplasm which has been shown to be a molecular marker of colorectal cancer.

Author contributions: All the authors have accepted responsibility for the entire content of this submitted manuscript and approved submission.

Research funding: None declared.

Conflict of interest statement: The authors declare no conflicts of interest regarding this article.

References

- [1] A. I. Doerflinger, *Design and Synthesis of Polymerized Micelles for the Diagnosis and Therapy of Tumours*, Paris, Université Paris-Saclay, 2017.
- [2] M. S. Rajagopalan, D. E. Heron, R. E. Wegner, et al., “Pathologic response with neoadjuvant chemotherapy and stereotactic body radiotherapy for borderline resectable and locally-advanced pancreatic cancer,” *Radiat. Oncol.*, vol. 8, p. 254, 2013.
- [3] M. A. Bellavance, M. Blanchette, and D. Fortin, “Recent advances in blood-brain barrier disruption as a CNS delivery strategy,” *AAPS J.*, vol. 10, pp. 166–177, 2008.
- [4] A. F. dos Santos, D. R. Q. de Almeida, L. F. Terra, M. S. Baptista, and L. Labriola, “Photodynamic therapy in cancer treatment - an update review,” *J. Canc. Metastasis Treat.*, vol. 5, p. 25, 2019.
- [5] R.-M. Szeimies, J. Dräger, C. Abels, and M. Landthaler, “Chapter 1 history of photodynamic therapy in dermatology,” in *Comprehensive Series in Photosciences*, vol. 2, P. Calzavara-Pinton, R.-M. Szeimies, and B. Ortel, Eds., Amsterdam, Elsevier, 2001, pp. 3–15.
- [6] C. Frochot, M. Barberi-Heyob, M. Blanchard-Desce, et al, “La thérapie photodynamique : état de l’art et perspectives,” *L’Actualité Chimique*, Société chimique de France, La chimie fête la lumière, 2015, pp. 46–50.
- [7] P. D. Silva, M. A. Saad, H. C. Thomsen, S. Bano, S. Ashraf, and T. Hasan, “Photodynamic therapy, priming and optical imaging: potential co-conspirators in treatment design and optimization — a Thomas Dougherty Award for Excellence in PDT paper,” *J. Porphyr. Phthalocyanines*, vol. 24, pp. 1320–1360, 2020.
- [8] D. Kessel and N. L. Oleinick, “Cell death pathways associated with photodynamic therapy: An update,” *Photochem. Photobiol.*, vol. 94, pp. 213–218, 2018.
- [9] T. J. Dougherty, J. E. Kaufman, A. Goldfarb, K. R. Weishaupt, D. Boyle, and A. Mittleman, “Photoradiation therapy for the treatment of malignant tumors,” *Canc. Res.*, vol. 38, pp. 2628–2635, 1978.
- [10] R. R. Allison and K. Moghissi, “Photodynamic therapy (PDT): PDT mechanisms,” *Clin. Endosc.*, vol. 46, pp. 24–29, 2013.
- [11] S. B. Brown, E. A. Brown, and I. Walker, “The present and future role of photodynamic therapy in cancer treatment,” *Lancet Oncol*, vol. 5, pp. 497–508, 2004.
- [12] M. Lan, S. Zhao, W. Liu, C.-S. Lee, W. Zhang, and P. Wang, “Photosensitizers for photodynamic therapy,” *Adv. Healthc. Mater.*, vol. 8, 2019, Art no. 1900132.

- [13] X. Dai, T. Du, and K. Han, "Engineering nanoparticles for optimized photodynamic therapy," *ACS Biomater. Sci. Eng.*, vol. 5, pp. 6342–6354, 2019.
- [14] L. Larue, A. Ben Mihoub, Z. Youssef, et al., "Using X-rays in photodynamic therapy: An overview," *Photochem. Photobiol. Sci.*, vol. 17, pp. 1612–1650, 2018.
- [15] B. Sun, R. Chang, S. Cao, et al., "Acid-Activatable transmorphic peptide-based nanomaterials for photodynamic therapy," *Angew. Chem. Int. Ed.*, vol. 59, pp. 20582–20588, 2020.
- [16] H. Azaïs, C. Schmitt, M. Tardivel, et al., "Assessment of the specificity of a new folate-targeted photosensitizer for peritoneal metastasis of epithelial ovarian cancer to enable intraperitoneal photodynamic therapy. A preclinical study," *Photodiagnosis Photodyn. Ther.*, vol. 13, pp. 130–138, 2016.
- [17] A. M. Gazzali, M. Lobry, L. Colombeau, et al., "Stability of folic acid under several parameters," *Eur. J. Pharmaceut. Sci.*, vol. 93, pp. 419–430, 2016.
- [18] W. M. Sharman, J. E. van Lier, and C. M. Allen, "Targeted photodynamic therapy via receptor mediated delivery systems," *Adv. Drug Deliv. Rev.*, vol. 56, pp. 53–76, 2004.
- [19] D. Zahavi and L. Weiner, "Monoclonal antibodies in cancer therapy," *Antibodies*, vol. 9, p. 34, 2020.
- [20] O. H. Aina, T. C. Sroka, M.-L. Chen, and K. S. Lam, "Therapeutic cancer targeting peptides," *Biopolymers*, vol. 66, pp. 184–199, 2002.
- [21] S. Li, Y. Jin, Y. Su, et al., "Anti-HER2 affibody-conjugated photosensitizer for tumor targeting photodynamic therapy," *Mol. Pharm.*, vol. 17, pp. 1546–1557, 2020.
- [22] J. Yan, T. Gao, Z. Lu, J. Yin, Y. Zhang, and R. Pei, "Aptamer-targeted photodynamic platforms for tumor therapy," *ACS Appl. Mater. Interfaces*, vol. 13, pp. 27749–27773, 2021.
- [23] R. Schneider, L. Tirand, C. Frochot, et al., "Recent improvements in the use of synthetic peptides for a selective photodynamic therapy," *Anticanc. Agents Med. Chem.*, vol. 6, pp. 469–488, 2006.
- [24] R. Mehdi, A. Mary, and A. M. Shaker, "Peptide-conjugated nanoparticles as targeted anti-angiogenesis therapeutic and diagnostic in cancer," *Curr. Med. Chem.*, vol. 26, pp. 5664–5683, 2019.
- [25] G. Graziani and P. M. Lecal, "Neuropilin-1 as therapeutic target for malignant melanoma," *Front. Oncol.*, vol. 5, p. 125, 2015.
- [26] S. Sun, Y. Lei, Q. Li, et al., "Neuropilin-1 is a glial cell line-derived neurotrophic factor receptor in glioblastoma," *Oncotarget*, vol. 8, pp. 74019–74035, 2017.
- [27] P. Hamerlik, J. D. Lathia, R. Rasmussen, et al., "Autocrine VEGF-VEGFR2-Neuropilin-1 signaling promotes glioma stem-like cell viability and tumor growth," *J. Exp. Med.*, vol. 209, pp. 507–520, 2012.
- [28] A. Starzec, P. Ladam, R. Vassy, et al., "Structure-function analysis of the antiangiogenic ATWLPFR peptide inhibiting VEGF(165) binding to neuropilin-1 and molecular dynamics simulations of the ATWLPFR/neuropilin-1 complex," *Peptides*, vol. 28, pp. 2397–2402, 2007.
- [29] E. Kamarulzaman, H. Benachour, M. Barberi-Heyob, et al., "Vascular-Targeted Photodynamic Therapy (VTP)," in *Advances in Cancer Therapy*, Hala Gali-Muhtasib, Ed., InTech, 2011, pp. 99–122, ISBN: 978-953-307-703-1.
- [30] C. L. Thomas, E. M. Bayer, C. Ritzenthaler, L. Fernandez-Calvino, and A. J. Maule, "Specific targeting of a plasmodesmal protein affecting cell-to-cell communication," *PLoS Biol.*, vol. 6, p. e7, 2008.
- [31] H. Benachour, A. Sève, T. Bastogne, et al., "Multifunctional peptide-conjugated hybrid silica nanoparticles for photodynamic therapy and MRI," *Theranostics*, vol. 2, pp. 889–904, 2012.
- [32] D. Bechet, F. Auger, P. Couleaud, et al., "Multifunctional ultrasmall nanoplateforms for vascular-targeted interstitial photodynamic therapy of brain tumors guided by real-time MRI," *Nanomedicine*, vol. 11, pp. 657–670, 2015.
- [33] P. Couleaud, D. Bechet, R. Vanderesse, et al., "Functionalized silica-based nanoparticles for photodynamic therapy," *Nanomedicine*, vol. 6, pp. 995–1009, 2011.
- [34] E. E. Kamarulzaman, R. Vanderesse, A. M. Gazzali, et al., "Molecular modelling, synthesis and biological evaluation of peptide inhibitors as anti-angiogenic agent targeting Neuropilin-1 for anticancer application," *J. Biomol. Struct. Dyn.*, vol. 35, pp. 26–45, 2017.
- [35] E. Kamarulzaman, R. Vanderesse, A. Gazzali, et al., "Molecular modelling, synthesis and biological evaluation of peptide inhibitors as anti-angiogenic agent targeting Neuropilin-1 for anticancer application," *J. Biomol. Struct. Dynam.*, vol. 35, pp. 1–49, 2016.
- [36] L. Tirand, C. Frochot, R. Vanderesse, et al., "A peptide competing with VEGF165 binding on neuropilin-1 mediates targeting of a chlorin-type photosensitizer and potentiates its photodynamic activity in human endothelial cells," *J. Contr. Release*, vol. 111, pp. 153–164, 2006.
- [37] Z. Youssef, N. Yesmurzayeva, L. Larue, et al., "New targeted gold nanorods for the treatment of glioblastoma by photodynamic therapy," *J. Clin. Med.*, vol. 8, p. 2205, 2019.
- [38] E. Thomas, L. Colombeau, M. Gries, et al., "Ultrasmall AGuIX theranostic nanoparticles for vascular-targeted interstitial photodynamic therapy of glioblastoma," *Int. J. Nanomed.*, vol. 12, pp. 7075–7088, 2017.
- [39] M. Gries, N. Thomas, J. Daouk, et al., "Multiscale selectivity and in vivo biodistribution of NRP-1-targeted theranostic AGuIX nanoparticles for PDT of glioblastoma," *Int. J. Nanomed.*, vol. 15, pp. 8739–8758, 2020.
- [40] L. Sancey, S. Kotb, C. Truillet, et al., "Long-term in vivo clearance of gadolinium-based AGuIX nanoparticles and their biocompatibility after systemic injection," *ACS Nano*, vol. 9, pp. 2477–2488, 2015.
- [41] O. Leduc, E. Fumière, S. Banse, et al., "Identification and description of the axillary web syndrome (AWS) by clinical signs, MRI and US imaging," *Lymphology*, vol. 47, pp. 164–176, 2014.
- [42] L. Sancey, F. Lux, S. Kotb, et al., "The use of theranostic gadolinium-based nanoprobe to improve radiotherapy efficacy," *Br. J. Radiol.*, vol. 87, p. 20140134, 2014.
- [43] C. C. Hsu, T. W. Watkins, G. N. Kwan, and E. M. Haacke, "Susceptibility-weighted imaging of glioma: update on current imaging status and future directions," *J. Neuroimaging*, vol. 26, pp. 383–390, 2016.
- [44] D. Schwarz, M. Bendszus, and M. O. Breckwoldt, "Clinical value of susceptibility weighted imaging of brain metastases," *Front. Neurol.*, vol. 11, 2020, <https://doi.org/10.3389/fneur.2020.00055>.
- [45] C. Zhao, Y. Tong, X. Li, et al., "Photosensitive nanoparticles combining vascular-independent intratumor distribution and on-demand oxygen-depot delivery for enhanced cancer photodynamic therapy," *Small*, vol. 14, 2018, Art no. e1703045.
- [46] D. Jiang, X. Gao, T. Kang, et al., "Actively targeting d- α -tocopheryl polyethylene glycol 1000 succinate-poly(lactic acid)

- nanoparticles as vesicles for chemo-photodynamic combination therapy of doxorubicin-resistant breast cancer,” *Nanoscale*, vol. 8, pp. 3100–3118, 2016.
- [47] H. Benachour, T. Bastogne, M. Toussaint, et al., “Real-time monitoring of photocytotoxicity in nanoparticles-based photodynamic therapy: a model-based approach,” *PLoS One*, vol. 7, p. e48617, 2012.
- [48] C. Frochet, B. Di Stasio, R. Vanderesse, et al., “Interest of RGD-containing linear or cyclic peptide targeted tetraphenylchlorin as novel photosensitizers for selective photodynamic activity,” *Bioorg. Chem.*, vol. 35, pp. 205–220, 2007.
- [49] H. Wang, C. Dong, P. Zhao, S. Wang, Z. Liu, and J. Chang, “Lipid coated upconverting nanoparticles as NIR remote controlled transducer for simultaneous photodynamic therapy and cell imaging,” *Int. J. Pharm.*, vol. 466, pp. 307–313, 2014.
- [50] F. Yuan, J.-L. Li, H. Cheng, X. Zeng, and X.-Z. Zhang, “A redox-responsive mesoporous silica based nanoplatfor in vitro tumor-specific fluorescence imaging and enhanced photodynamic therapy,” *Biomater. Sci.*, vol. 6, pp. 96–100, 2018.
- [51] B. Hou, B. Zheng, W. Yang, C. Dong, H. Wang, and J. Chang, “Construction of near infrared light triggered nanodumbbell for cancer photodynamic therapy,” *J. Colloid Interface Sci.*, vol. 494, pp. 363–372, 2017.
- [52] Y. Zhao, F. Li, C. Mao, and X. Ming, “Multiarm nanoconjugates for cancer cell-targeted delivery of photosensitizers,” *Mol. Pharm.*, vol. 15, pp. 2559–2569, 2018.
- [53] A. Yuan, B. Yang, J. Wu, Y. Hu, and X. Ming, “Dendritic nanoconjugates of photosensitizer for targeted photodynamic therapy,” *Acta Biomater.*, vol. 21, pp. 63–73, 2015.
- [54] S. K. Kim, J. M. Lee, K. T. Oh, and E. S. Lee, “Extremely small-sized globular poly(ethylene glycol)-cyclic RGD conjugates targeting integrin $\alpha(v)\beta(3)$ in tumor cells,” *Int. J. Pharm.*, vol. 528, pp. 1–7, 2017.
- [55] S. Shi, L. Zhang, M. Zhu, et al., “Reactive oxygen species-responsive nanoparticles based on PEGylated prodrug for targeted treatment of oral tongue squamous cell carcinoma by combining photodynamic therapy and chemotherapy,” *ACS Appl. Mater. Interfaces*, vol. 10, pp. 29260–29272, 2018.
- [56] K. N. Sugahara, T. Teesalu, P. P. Karmali, et al., “Tissue-penetrating delivery of compounds and nanoparticles into tumors,” *Canc. Cell*, vol. 16, pp. 510–520, 2009.
- [57] F. Yan, H. Wu, H. Liu, et al., “Molecular imaging-guided photothermal/photodynamic therapy against tumor by iRGD-modified indocyanine green nanoparticles,” *J. Contr. Release*, vol. 224, pp. 217–228, 2016.
- [58] Y. Sheng, Z. Wang, G. M. Ngandeu Neubi, et al., “Lipoprotein-inspired penetrating nanoparticles for deep tumor-targeted shuttling of indocyanine green and enhanced photo-theranostics,” *Biomater. Sci.*, vol. 7, pp. 3425–3437, 2019.
- [59] Y. Wang, Y. Xie, K. V. Kilchrist, J. Li, C. L. Duvall, and D. Oupický, “Endosomolytic and tumor-penetrating mesoporous silica nanoparticles for siRNA/miRNA combination cancer therapy,” *ACS Appl. Mater. Interfaces*, vol. 12, pp. 4308–4322, 2020.
- [60] A. Zhou, Y. Wei, B. Wu, Q. Chen, and D. Xing, “Pyropheophorbide A and c(RGDyK) comodified chitosan-wrapped upconversion nanoparticle for targeted near-infrared photodynamic therapy,” *Mol. Pharm.*, vol. 9, pp. 1580–1589, 2012.
- [61] A. Zhou, Y. Wei, Q. Chen, and D. Xing, “Vivo near-infrared photodynamic therapy based on targeted upconversion nanoparticles,” *J. Biomed. Nanotechnol.*, vol. 11, pp. 2003–2010, 2015.
- [62] Z. Yi, X. Li, Z. Xue, et al., “Tumor detection: remarkable NIR enhancement of multifunctional nanoprobe for in vivo trimodal bioimaging and upconversion optical/T2-weighted MRI-guided small tumor diagnosis,” *Adv. Funct. Mater.*, vol. 25, p. 7102, 2015.
- [63] X. L. Tang, J. Wu, B. L. Lin, et al., “Near-infrared light-activated red-emitting upconverting nanoplatfor for T(1)-weighted magnetic resonance imaging and photodynamic therapy,” *Acta Biomater.*, vol. 74, pp. 360–373, 2018.
- [64] F. F. E. Kohle, S. Li, M. Z. Turker, and U. B. Wiesner, “Ultrasml PEGylated and targeted core-shell silica nanoparticles carrying methylene blue photosensitizer,” *ACS Biomater. Sci. Eng.*, vol. 6, pp. 256–264, 2020.
- [65] R. Kopelman, Y.-E. Lee Koo, M. Philbert, et al., “Multifunctional nanoparticle platforms for in vivo MRI enhancement and photodynamic therapy of a rat brain cancer,” *J. Magn. Magn Mater.*, vol. 293, pp. 404–410, 2005.
- [66] L. V. Halig, D. Wang, A. Y. Wang, Z. G. Chen, and B. Fei, “Biodistribution study of nanoparticle encapsulated photodynamic therapy drugs using multispectral imaging,” *Proc. SPIE-Int. Soc. Opt. Eng.*, vol. 8672, 2013, <https://doi.org/10.1117/12.2006492>.
- [67] D. Wang, B. Fei, L. V. Halig, et al., “Targeted iron-oxide nanoparticle for photodynamic therapy and imaging of head and neck cancer,” *ACS Nano*, vol. 8, pp. 6620–6632, 2014.
- [68] J. Dai, Y. Li, Z. Long, et al., “Efficient near-infrared photosensitizer with aggregation-induced emission for imaging-guided photodynamic therapy in multiple xenograft tumor models,” *ACS Nano*, vol. 14, pp. 854–866, 2020.
- [69] K. Haedicke, D. Kozlova, S. Gräfe, U. Teichgräber, M. Epple, and I. Hilger, “Multifunctional calcium phosphate nanoparticles for combining near-infrared fluorescence imaging and photodynamic therapy,” *Acta Biomater.*, vol. 14, pp. 197–207, 2015.
- [70] H. Cao, Y. Qi, X. Gao, et al., “Two-photon excited peptide nanodrugs for precise photodynamic therapy,” *Chem. Commun.*, vol. 57, pp. 2245–2248, 2021.
- [71] Y. Wang, L. Jiang, Y. Zhang, et al., “Fibronectin-targeting and cathepsin B-activatable theranostic nanoprobe for MR/fluorescence imaging and enhanced photodynamic therapy for triple negative breast cancer,” *ACS Appl. Mater. Interfaces*, vol. 12, pp. 33564–33574, 2020.
- [72] L. S. Carvalho, N. Gonçalves, N. A. Fonseca, and J. N. Moreira, “Cancer stem cells and nucleolin as drivers of carcinogenesis,” *Pharmaceuticals*, vol. 14, p. 60, 2021.
- [73] N. A. Fonseca, A. S. Rodrigues, P. Rodrigues-Santos, et al., “Nucleolin overexpression in breast cancer cell sub-populations with different stem-like phenotype enables targeted intracellular delivery of synergistic drug combination,” *Biomaterials*, vol. 69, pp. 76–88, 2015.

- [74] K. Porkka, P. Laakkonen, J. A. Hoffman, M. Bernasconi, and E. Ruoslahti, "A fragment of the HMG2 protein homes to the nuclei of tumor cells and tumor endothelial cells in vivo," *Proc. Natl. Acad. Sci. U. S. A.*, vol. 99, pp. 7444–7449, 2002.
- [75] M. E. Akerman, W. C. Chan, P. Laakkonen, S. N. Bhatia, and E. Ruoslahti, "Nanocrystal targeting in vivo," *Proc. Natl. Acad. Sci. U. S. A.*, vol. 99, pp. 12617–12621, 2002.
- [76] G. R. Reddy, M. S. Bhojani, P. McConville, et al., "Vascular targeted nanoparticles for imaging and treatment of brain tumors," *Clin. Canc. Res.*, vol. 12, pp. 6677–6686, 2006.
- [77] H. J. Hah, G. Kim, Y. E. Lee, et al., "Methylene blue-conjugated hydrogel nanoparticles and tumor-cell targeted photodynamic therapy," *Macromol. Biosci.*, vol. 11, pp. 90–99, 2011.
- [78] D. A. Orringer, Y.-E. L. Koo, T. Chen, et al., "In vitro characterization of a targeted, dye-loaded nanodevice for intraoperative tumor delineation," *Neurosurgery*, vol. 64, pp. 965–972, 2009.
- [79] X. Feng, D. Jiang, T. Kang, et al., "Tumor-homing and penetrating peptide-functionalized photosensitizer-conjugated PEG-PLA nanoparticles for chemo-photodynamic combination therapy of drug-resistant cancer," *ACS Appl. Mater. Interfaces*, vol. 8, pp. 17817–17832, 2016.
- [80] A. Borrelli, A. L. Tornesello, M. L. Tornesello, and F. M. Buonaguro, "Cell penetrating peptides as molecular carriers for anti-cancer agents," *Molecules*, vol. 23, p. 295, 2018.
- [81] A. Subrizi, E. Tuominen, A. Bunker, T. Róg, M. Antopolsky, and A. Urtti, "Tat(48-60) peptide amino acid sequence is not unique in its cell penetrating properties and cell-surface glycosaminoglycans inhibit its cellular uptake," *J. Contr. Release*, vol. 158, pp. 277–285, 2012.
- [82] A. M. Fales, H. Yuan, and T. Vo-Dinh, "Cell-penetrating peptide enhanced intracellular Raman imaging and photodynamic therapy," *Mol. Pharm.*, vol. 10, pp. 2291–2298, 2013.
- [83] M. Thandu, V. Rapozzi, L. Xodo, F. Albericio, C. Comuzzi, and S. Cavalli, "Clicking" porphyrins to magnetic nanoparticles for photodynamic therapy," *ChemPlusChem*, vol. 79, pp. 90–98, 2014.
- [84] M. Gao, F. Fan, D. Li, et al., "Tumor acidity-activatable TAT targeted nanomedicine for enlarged fluorescence/magnetic resonance imaging-guided photodynamic therapy," *Biomaterials*, vol. 133, pp. 165–175, 2017.
- [85] G. Wan, Y. Cheng, J. Song, et al., "Nucleus-targeting near-infrared nanoparticles based on TAT peptide-conjugated IR780 for photo-chemotherapy of breast cancer," *Chem. Eng. J.*, vol. 380, p. 122458, 2020.
- [86] S. Gomez, A. Tsung, and Z. Hu, "Current targets and bioconjugation strategies in photodynamic diagnosis and therapy of cancer," *Molecules*, vol. 25, p. 4964, 2020.
- [87] T.-Y. Sun, Q. Wang, J. Zhang, T. Wu, and F. Zhang, "Trastuzumab-peptide interactions: mechanism and application in structure-based ligand design," *Int. J. Mol. Sci.*, vol. 14, pp. 16836–16850, 2013.
- [88] A. Narsireddy, K. Vijayashree, J. Irudayaraj, S. V. Manorama, and N. M. Rao, "Targeted in vivo photodynamic therapy with epidermal growth factor receptor-specific peptide linked nanoparticles," *Int. J. Pharm.*, vol. 471, pp. 421–429, 2014.
- [89] A. Narsireddy, K. Vijayashree, M. G. Adimoolam, S. V. Manorama, and N. M. Rao, "Photosensitizer and peptide-conjugated PAMAM dendrimer for targeted in vivo photodynamic therapy," *Int. J. Nanomed.*, vol. 10, pp. 6865–6878, 2015.
- [90] I. Genta, E. Chiesa, B. Colzani, T. Modena, B. Conti, and R. Dorati, "GE11 peptide as an active targeting agent in antitumor therapy: A minireview," *Pharmaceutics*, vol. 10, 2017, <https://doi.org/10.3390/pharmaceutics10010002>.
- [91] R. S. Agnes, A. M. Broome, J. Wang, A. Verma, K. Lavik, and J. P. Babilion, "An optical probe for noninvasive molecular imaging of orthotopic brain tumors overexpressing epidermal growth factor receptor," *Mol. Canc. Therapeut.*, vol. 11, pp. 2202–2211, 2012.
- [92] A. M. Master, M. Livingston, N. L. Oleinick, and A. Sen Gupta, "Optimization of a nanomedicine-based silicon phthalocyanine 4 photodynamic therapy (Pc 4-PDT) strategy for targeted treatment of EGFR-overexpressing cancers," *Mol. Pharm.*, vol. 9, pp. 2331–2338, 2012.
- [93] A. M. Master, Y. Qi, N. L. Oleinick, and A. S. Gupta, "EGFR-mediated intracellular delivery of Pc 4 nanoformulation for targeted photodynamic therapy of cancer: in vitro studies," *Nanomedicine*, vol. 8, pp. 655–664, 2012.
- [94] N. Miyoshi, H. Ishii, K. Mimori, et al., "TGM2 is a novel marker for prognosis and therapeutic target in colorectal cancer," *Ann. Surg. Oncol.*, vol. 17, pp. 967–972, 2010.
- [95] Z. J. Li, W. K. Wu, S. S. Ng, et al., "A novel peptide specifically targeting the vasculature of orthotopic colorectal cancer for imaging detection and drug delivery," *J. Contr. Release*, vol. 148, pp. 292–302, 2010.
- [96] A. de Oliveira É, B. L. Faintuch, D. Seo, et al., "Radiolabeled GX1 peptide for tumor angiogenesis imaging," *Appl. Biochem. Biotechnol.*, vol. 185, pp. 863–874, 2018.
- [97] D. Guo, S. Xu, N. Wang, et al., "Prodrug-embedded angiogenic vessel-targeting nanoparticle: A positive feedback amplifier in hypoxia-induced chemo-photo therapy," *Biomaterials*, vol. 144, pp. 188–198, 2017.
- [98] V. Fogal, L. Zhang, S. Krajewski, and E. Ruoslahti, "Mitochondrial/cell-surface protein p32/gC1qR as a molecular target in tumor cells and tumor stroma," *Canc. Res.*, vol. 68, pp. 7210–7218, 2008.
- [99] L. Chen, H. Yin, B. Farooqi, S. Sebti, A. D. Hamilton, and J. Chen, "p53 alpha-Helix mimetics antagonize p53/MDM2 interaction and activate p53," *Mol. Canc. Therapeut.*, vol. 4, pp. 1019–1025, 2005.
- [100] J. Banerjee, E. Radvar, and H. S. Azevedo, "10 - self-assembling peptides and their application in tissue engineering and regenerative medicine," in *Peptides and Proteins as Biomaterials for Tissue Regeneration and Repair*, M. A. Barbosa and M. C. L. Martins, Eds., Cambridge, Woodhead Publishing, 2018, pp. 245–281.
- [101] Y. Zhang, C. Deng, S. Liu, et al., "Active targeting of tumors through conformational epitope imprinting," *Angew. Chem. Int. Ed.*, vol. 54, pp. 5157–5160, 2015.
- [102] T. R. Daniels, E. Bernabeu, J. A. Rodríguez, et al., "The transferrin receptor and the targeted delivery of therapeutic agents against cancer," *Biochim. Biophys. Acta*, vol. 1820, pp. 291–317, 2012.

- [103] M. Ruivard, M. Boursiac, G. Mareynat, x et al., "Diagnostic de la carence en fer: évaluation du rapport « récepteur soluble de la transferrine/ferritine »,» *Rev. Med. Interne*, vol. 21, pp. 837–843, 2000.
- [104] S. Li, H. Zhao, X. Mao, et al., "Transferrin receptor targeted cellular delivery of doxorubicin via a reduction-responsive peptide-drug conjugate," *Pharmaceut. Res.*, vol. 36, p. 168, 2019.
- [105] T. Zhang, S. Huang, H. Lin, et al., "Enzyme and pH-responsive nanovehicles for intracellular drug release and photodynamic therapy," *New J. Chem.*, vol. 41, pp. 2468–2478, 2017.
- [106] N. Kamimura, A. M. Wolf, and Y. Iwai, "Development of cancer immunotherapy targeting the PD-1 pathway," *J. Nippon Med. Sch.*, vol. 86, pp. 10–14, 2019.
- [107] B. Liu, G. Qiao, Y. Han, et al., "Targeted theranostics of lung cancer: PD-L1-guided delivery of gold nanoprisms with chlorin e6 for enhanced imaging and photothermal/photodynamic therapy," *Acta Biomater*, vol. 117, pp. 361–373, 2020.
- [108] L. Wang, C. Dong, X. Li, W. Han, and X. Su, "Anticancer potential of bioactive peptides from animal sources (Review)," *Oncol. Rep.*, vol. 38, pp. 637–651, 2017.
- [109] S. Li, L. Liu, G. He, and J. Wu, "Molecular targets and mechanisms of bioactive peptides against metabolic syndromes," *Food Funct.*, vol. 9, pp. 42–52, 2018.
- [110] H. Cheng, R. R. Zheng, G. L. Fan, et al., "Mitochondria and plasma membrane dual-targeted chimeric peptide for single-agent synergistic photodynamic therapy," *Biomaterials*, vol. 188, pp. 1–11, 2019.